The advancement of the TU Delft vaporising liquid micro-resistojet design

AE5211: Thesis Flight Performance and Propulsion

L. J. M. Cramer

Delft University of Technology

TU Delft

The advancement of the TU Delft vaporising liquid micro-resistojet design

by

L. J. M. Cramer

Student Number 4552830

Instructor:	J. A. Melkert, B. T. C. Zandbergen
Project Duration:	January, 2023 - May, 2024
Faculty:	Faculty of Aerospace Engineering, Delft

Cover: M-Cubed/COVE-2 by Jet Propulsion Lab, NASA

TU Delft

Preface

Dear reader,

Thank you for picking up the work that accumulates eight years of hard work. Before we start going into the science, I would like to acknowledge everybody who has made this work possible.

I started my bachelor's degree in 2016 with plenty of hope and ambition. During this period, I have had the pleasure of meeting many wonderful people and I was taught about wonderous things. I believe the best lectures are those that inspire and our aerospace faculty is full of those. I have been fortunate to have Joris Melkert and Barry Zandbergen as mentors for my thesis. Their support and guidance have been invaluable, especially in allowing me to pursue my passion for rocket engines. I have had the opportunity to work on three different engines so far, and I cannot wait to see where this journey takes me next.

One of the best decisions I made during my student time was taking a gap year and joining DARE. I spent a year, and some more due to Corona, building and testing a 25 kN hybrid engine for a rocket destined for space. This position taught me what type of work I really enjoy doing and I would like to thank everybody from the Stratos IV team who has made this possible. Especially Roderick who was always there to keep things calm amidst the chaos.

I would like to thank all my friends back in Gouda, who have always shown interest when I talked about rockets. They supported me throughout my entire student time and were always there when I needed a break. They have been there for me through thick and thin, and I could not have done it without them. The same goes for all the friends I made during my time in Delft, the infinite coffee breaks and lectures we had together made better by each others company. A special thanks goes out to my best friend, Alex, and my partner, Kieran. Without their patience, encouragement, and endless brainstorming sessions, I would not be where I am today.

My family has also been a big support. My grandma who believed that with hard work you can achieve anything. Proven to be true as I will be obtaining my aerospace degree soon. My mom who has endlessly cared for me when I was too busy studying and my little brother who is my biggest cheer-leader.

As I look ahead to the future, I am grateful for the support of all these amazing people who have helped me along the way. Here's to the next chapter of this journey.

L. J. M. Cramer
Delft, April 2024

Summary

Small satellites, in particular nanosatellites, are an upcoming technology that offer flexible designs, faster manufacturing periods, and cost efficiency compared to their larger equivalents. Creating a variety of micro-propulsion systems is crucial to enable miniaturised spacecraft to realise their full potential. The TU Delft has its own program, Delfi, which develops small satellites and aims to lead the way in a somewhat uncharted category of satellites. During this research, efforts have been made to improve the current micro-resistojet design of the TU Delft and its test set-up. Two previous master students had developed a resistojet using readily available components and machining techniques to decrease cost and production times. Experiments were conducted with both nitrogen and water as propellant and it was found that the test set-up using water was not optimal. The primary goals of this project were to improve the heating capacity of the thruster and to explore whether a transition to a different thrust bench could enhance the precision of thrust measurements, thus potentially decreasing the associated uncertainty.

During the disassembly of the thruster significant degradation off the sealing edge was detected. In an effort to make the thruster leak tight regardless of the damage, additional torque was applied to the screws holding together the thruster construction. This did resolve the leak, but upon inspection this also resulted in a deformation of the nozzle geometry. The throat geometry cannot be measured and assumptions were made regarding the dimensions. As the thruster geometry is significantly altered, collected experiment data can no longer be used to verify the behaviour of predecessors.

Calibrations of the new test bench were performed with a variable-density turn coil. Data was collected while a range of loads were applied, this data had a recorded 3σ value of up to 40%. Whether this was an artefact of the calibration method used or caused by the way that the test bench is assembled is unknown at this point. Suggestions have been made to narrow down the cause for future research.

The thruster was mounted to the new test bench and tested with nitrogen. In the thrust results both long-term and short-term drift was identified. Possible explanations for this behaviour are discussed. The experimental results did not match the predicted performance as dictated by the previously developed analytical model. Given that the thrust bench was also replaced simultaneously, it became impossible to determine which portion in the measured results could be attributed to the incorrect thruster assembly or to the switching from the thrust bench.

A potential shortcoming of the analytical model was identified as relations for axisymmetrical nozzles were used whereas the real life thruster has a 2D geometry. In micro-nozzles, viscous boundary layers have a significant impact on the efficiency. This means that gas-surface interactions are an important factor in predicting the thruster efficiency. Viscous effects, wall roughness and corner effects are overlooked or underestimated in the current approach.

Contents

1 Introduction

Over the past few decades, there has been a significant rise in the deployment of miniaturised spacecraft, with an ever-growing demand for Earth observation. Small satellites, particularly nanosatellites, have emerged as a practical solution due to their inherent flexibility, quicker production times, and cost-effectiveness compared to larger counterparts [1]. Despite their constrained size, nanosatellites mark a new era in space exploration, offering opportunities such as formation flying, where multiple small satellites collaborate on various experiments, enhancing redundancy and lowering risks [2]. Additionally, nanosatellites can exploit piggybacking opportunities during larger mission launches, effectively reducing launch costs [3]. However, this novel approach presents its own set of challenges, notably the need for miniaturised propulsion systems. These systems must deliver precise attitude corrections and sufficient power for orbit adjustments [4]. They also need to endure numerous on/off cycles, exhibit high specific impulse, low thrust, and maintain compact dimensions to seamlessly integrate within the satellite. Among the potential solutions, the micro-resistojet stands out, utilising electrical power to heat the propellant and expel it through a converging-diverging nozzle [5]. The development of such micro-resistojet technology is essential for enhancing nanosatellite capabilities and facilitating broader access to space.

At the Technical University of Delft, there is a programme developing small satellites named Delfi [6]. The purpose of this programme is to showcase the usage of miniaturised spacecraft and provide pre-qualification for new technologies. There has been considerable effort put into developing a micro-resistojet for such a satellite. The particular design this thesis focuses on has been developed and tested by two previous master's students. The key aspect of this design is that it uses readily available components wherever possible, such as the heater. This strategy speeds up the thruster's development, leading to cost savings. The fabrication process focuses on simplicity and availability to ensure ease of implementation. The goal of the thesis will be the advancement of the Commercial off-the-Shelf (COTS) vaporising liquid resistojet developed by the Space department of the TU Delft. This is defined as improving the thruster and test bench functionality to lower the uncertainty. This includes validation of thruster performance through comparison with analytical results and previously obtained experimental results. Currently, the design is limited in its heating capacity, this is addressed. Furthermore, the test bench introduced a measurement inaccuracy exceeding 10%, a margin deemed too significant for design verification.

This main objective can be divided into four research questions which are listed below. With these questions, a new design will be developed and tested during the thesis.

- How can the thruster design be improved?
    - How will the heating be implemented to achieve a propellant temperature of 400°C?
- How does the experimental set-up need to be modified to decrease the measurement inaccuracy below 10%?
    - How does the experimental set-up need to be modified to fit on the TB-50m?

    - How should a proper calibration be executed?
- Can the thruster performance be estimated by the analytical model suggested by Makhan [7] and elaborated by Versteeg and Pappadimitriou [8, 9]?
    - What changes should be made to the analytical model?
- How well does the thruster performance compare to data obtained by Versteeg and Hutten?
    - What influence does the modified test bench have?

This thesis essentially has two parts, one part is scientific with the aim of answering the research questions. The other part is written with the repeatability of the project in mind and is therefore more descriptive. In chapter 2 the findings of the literature study [10] have been summarised. The literature study had the goal of identifying which changes could be implemented into the thruster and set-up. To predict the behaviour of the thruster in chapter 3 an analytical model has been set up, starting from ideal rocket theory and expanding with correcting factors. Changes to the thruster have been made in chapter 4 and the test set-up is discussed in chapter 5. In these chapters, the methodology has been described in detail to assist future experiments. An electrical diagram of the system has also been developed to clarify the system. In chapter 6 preliminary tests have been conducted to characterise the thruster; the nozzle geometry, surface roughness, and leak rate. Furthermore, the test bench has been characterised through calibration. chapter 7 explains the experiments that are conducted and their results. In chapter 8 the obtained data is compared to predecessor results to verify that the thruster behaves as expected after modifications have been made. The results of the analytical model are compared to that of the experiment to see whether the thruster behaves as predicted by theory. Finally, conclusions are drawn to answer the research questions and recommendations are made for future research in chapter 9 and chapter 10 respectively.

2

Background information

During the literature study [10] the author looked into the history of vaporising liquid micro-resistojet (VLM) especially at the TU Delft. It was decided to continue the projects of H. Versteeg [8] and R. Hutten [11], who looked into a motor that could be made with readily available machines and materials. Several improvements were identified which will be elaborated upon in this chapter. But first, an explanation of the type of thruster used in this project is given and the history of the project is explained.

2.1. Thruster

Before diving into the work performed at the TU Delft, first a bit of background will be given on the type of thruster being discussed. A resistojet is a type of electrothermal propulsion where electrical energy is converted into thermal energy which results in kinetic energy. With a resistojet the propellant is electrically heated, before exiting the thruster via a supersonic nozzle as is shown in Figure 2.1. It is a simple system with a propellant tank, valve and thruster body with heater. It is an interesting system for satellite propulsion as it often has lower thrust but higher specific impulse compared to conventional chemical propulsion method. Specific impulse (I_{sp}) is a measure of how efficiently propellant is converted to thrust, $I_{sp} = F_{thrust}/(\dot{m} \cdot g_0)$, where $\dot{m}$ is the mass flow rate in kg/s and g_0 is the gravitational constant. This system has a low complexity compared to other electrical systems [12].

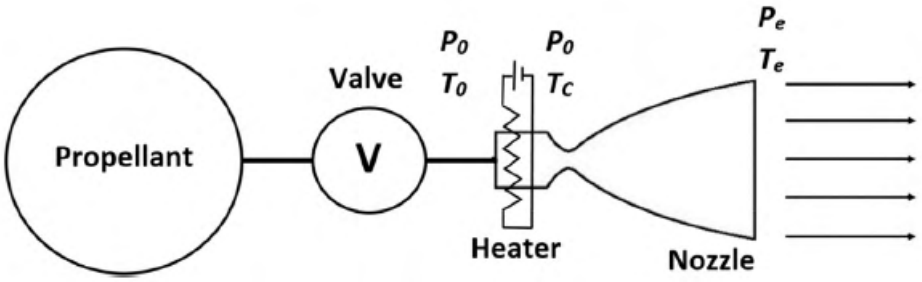

Figure 2.1: PI&D of an electrothermal system ([12], chapter 5)

Water was picked as a propellant based on a paper written by David Guerriri [5]. This paper looks at a wide variety of propellants and compares them using several criteria: Performance, Safety, System density and velocity increments (ΔV) achieved. Water comes out on top due to its high liquid density and safety of handling, the one downside being the high power consumption due to the relatively high energy of vaporisation. A serious contender is ammonia, however this poses a serious safety risk and is deemed unsuitable for a master thesis project.

2.2. History

This project started as the master thesis project of Versteeg [8] to see if a viable alternative could be made to the Micro-Electro-Mechanical System (MEMS) VLM that was under development at the TU. This technique had the drawback that iterations were time-consuming and expensive. Moreover the strength of a VLM is the increase in performance with temperature. This Micro-Electro-Mechanical System (MEMS) design was limited to 150°C due to sealing issues. Versteeg developed a thruster consisting of two copper blocks that act both as seal and heat conductors with a thruster profile clamped in between. Figure 2.2 shows both the copper block with thruster profile and foam as well as the complete thruster. An exploded view is shown in Figure 2.4. The copper blocks have a ridge on them that presses into the steel thruster profile, images of this sealing edge can be found in subsection 4.3.3. The profile is cut with wire-Electrical discharge machining (EDM) to achieve the microscopic nozzle. A foam insert was placed within the thruster body to promote heat conduction towards the propellant. Disk springs are added to the bolts holding the construction in place to release the thermal stress the body will experience. A heat shield was made out of bent aluminium to increase the heating efficiency. This construction was tested in the clean room at the Aerospace Faculty's 8th floor with nitrogen up to 400°C. A pendulum test bench was used, the TB-5m, the complete set-up including thruster is displayed in Figure 2.3. A bracket consisting of two parts was used to clamp the thruster to the pendulum. Two tubes connect the bracket to the thruster, one as propellant feed line, the other as pressure sensor. Sensors could not be mounted directly to the thruster body due to the high temperatures.

(a) Inside of the thruster with metal foam and nozzle profile

(b) Assembled thruster

Figure 2.2: Thruster by Versteeg [8]

Hutten [11] continued this thesis intending to introduce water as propellant as this has a higher specific impulse. He ran into an issue during leak testing where the nozzle seemed to be blocked, based on the pressure, temperature, and mass flow relation. He then had to take the thruster apart and re-assemble it to get rid of the obstruction. He advised putting a mesh before the nozzle to prevent any debris from blocking the nozzle in the future. The feed system had to be adjusted to use water as a propellant, for this a syringe pump was found. The thruster was mounted upside down to prevent water drops from creating thrust bursts.

The cartridge heaters used in this project are not perfectly round, when placing them inside the copper blocks there is empty space between the surfaces. This empty space in vacuum prevents heat transfer to the surrounding of the cartridge heater causing it to overheat and break. Compared to the nitrogen tests performed by Versteeg, the amount of heat required to heat up water is larger. The water tests are also planned to be longer to record steady-state performance of the thruster. Previously the heaters were used to heat up the thruster, and then turned off prior to the test, this is no longer an option. Hutten has solved this issue by using copper grease to fill the cavity to promote heat conduction and prevent overheating.

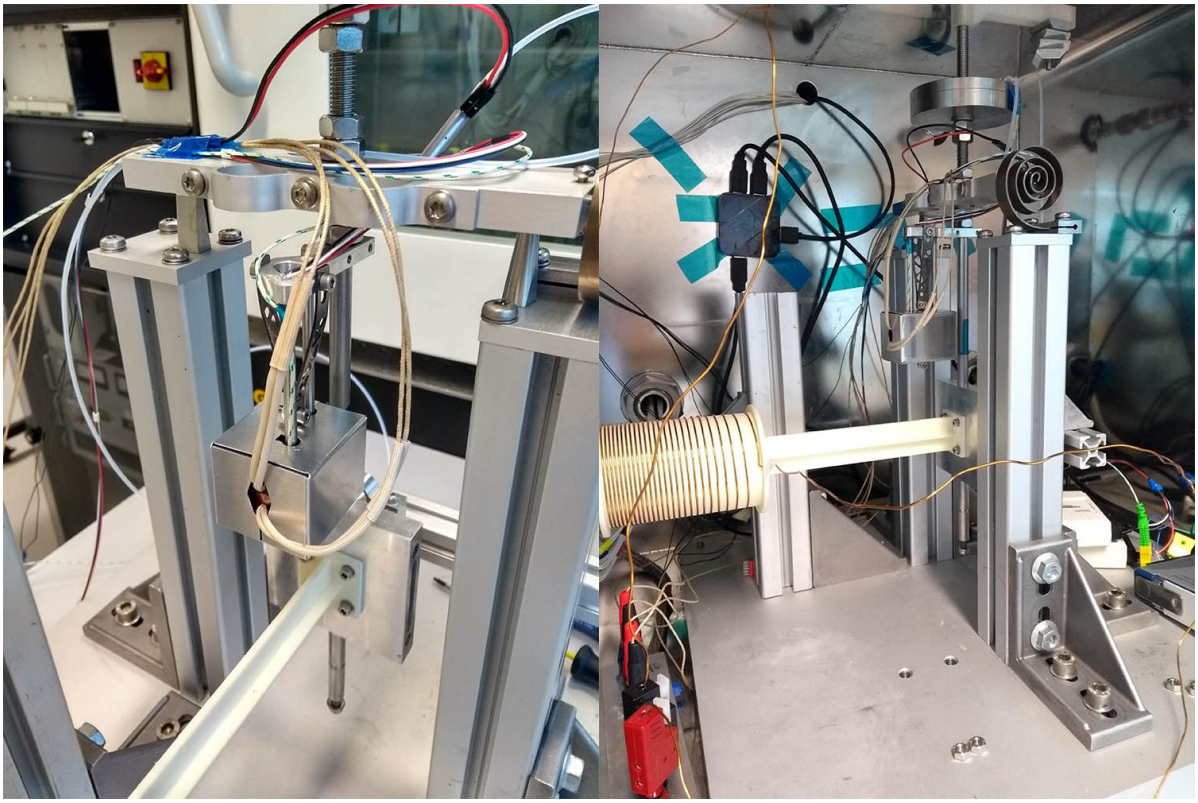

Figure 2.3: Test set-up as used by Versteeg and Hutten with the thruster attached to the TB-5m [8]

The results Hutten [11] obtained from experimental tests with water as propellant had a measurement inaccuracy of $\sim$14% on the specific impulse. This is too much to be used as validation data for the analytical model. This inaccuracy can be attributed to multiple factors. The test bench is dependent on the Centre of Gravity of the thruster, which is subjected to changes by thermal expansion and liquid propellant mass. The mass flow was not constant and led to a chamber pressure increase over the firing duration. After the test is done, water remains in the system which is slowly evaporating, this makes calibration afterwards very difficult. These uncertainties became apparent with water testing, the measurement inaccuracy for nitrogen was an acceptable 1.5%. The inaccuracy of the analytical model is estimated to be 10% due to the vacuum pressure sensor and nozzle geometry determination, the results for the experimental tests should be within this margin.

Another part of the thesis is setting up an analytic model that is able to predict the thruster performance. The thrusters are built to compare the analytical results with experimental data. This analytical model is elaborated upon in chapter 3.

2.3. Improvements

During the literature study [10] several improvements that could be made to the thruster and the experimental set-up were identified to improve the thruster performance and decrease the measurement inaccuracy. In this section, the selection of design alterations that will be investigated in this thesis are presented. Their implementation is worked out in chapter 4.

2.3.1. Heater

To promote heat transfer several changes will be made to the system. Next to increasing the cartridge heater efficiency, it will be looked into whether a mica sheet heater has potential for enhanced performance. This type of patch heater could be placed on the top and bottom of the heater and can go up to 500°C.

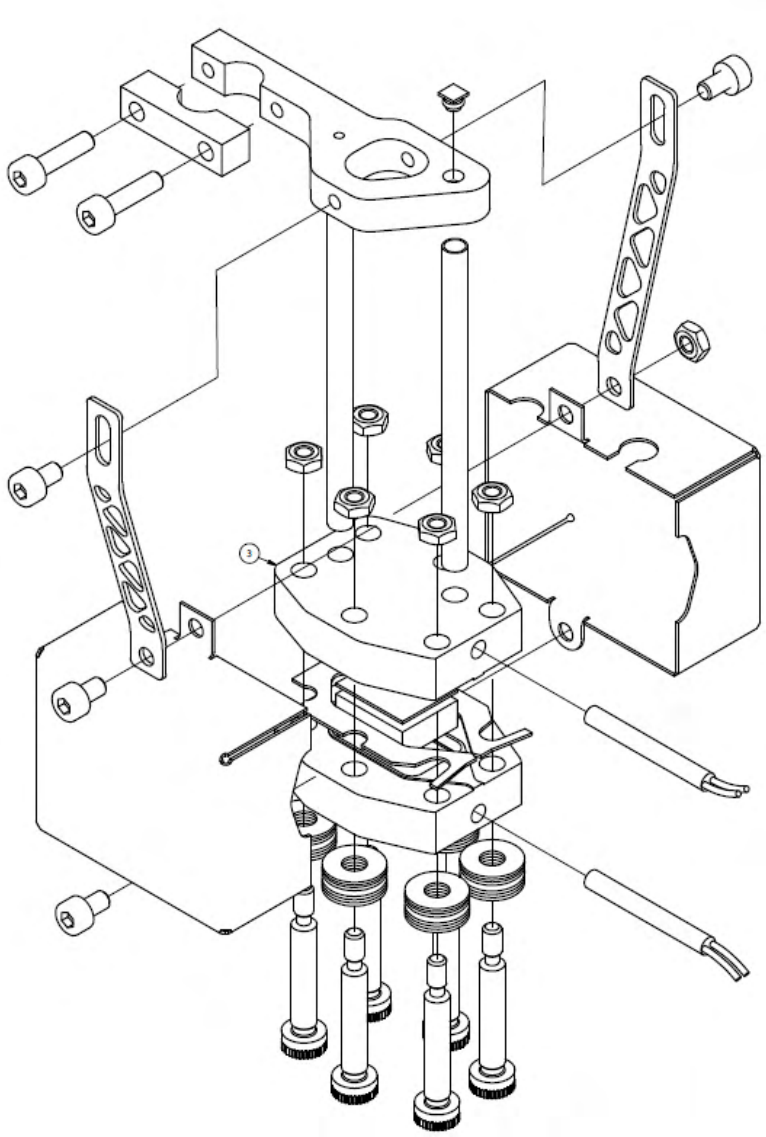

Figure 2.4: Exploded view [8]

Securement

The boiling point of grease now limits the temperature to which the thruster can be heated to 300°C due to the possibility of the boiling fluid pushing the cartridge heater out. A method has been devised to secure the cartridge heater to the copper blocks, such that risk of the heater moving does not limit the thrusters performance. A male thread will be attached to the cartridge heater and a female thread will be added to the copper block to prevent the cartridge heater from moving. This should also promote the heater efficiency as the materials are now in direct contact with each other.

Thermal adhesive

Next to securing the heater to the structure, it should have a snug fit inside the hole to promote conduction. This can be accomplished by adding liquid metals into the hole as metal is an excellent conductor. Currently copper grease is used, but as mentioned previously this limits the heating capacity. It was decided to opt for a liquid metal-based thermal paste. These are most commonly used to cool the Central Processing Unit (CPU) of computers, however they possess qualities that make them suitable for this purpose. Liquid metal pastes have a high thermal conductivity and are often gallium-based. Gallium-based liquid metal pastes have the highest surface tension of any liquid metal at room temperature. They spread isotopically on a surface. This is likely to be resistant against leakage through

the thread. Gallium has a very high vapour pressure and should not pose an issue inside the vacuum chamber. Gallium does react with aluminium and should be handled with care when inserted into the copper cavity.

2.3.2. Feedsystem

Liquid water entering the thruster will cause explosive boiling and erratic thrust profiles, this is made worse by air bubbles being present in the lines as this creates a non-constant supply of propellant. Using silicone patches can aid in vaporising the water inside of the propellant line, ensuring it gets heated to above 100°C and preventing liquid water from getting into the chamber.

In case heating the propellant line is unfeasible it would be interesting to add foam inserts to the propellant line. This will create more heating surface and the foam will retain the liquid propellant through surface tension while the vaporised water goes into the thruster chamber.

Air bubbles can be prevented by deaerating the propellant by boiling it before inserting it into the syringe. Deaerating can also be achieved by putting the water in the vacuum chamber before use. This should remove any air dissolved in the water. Shortening the distance between the valve and thruster will shorten the settling time of the thruster.

2.3.3. Test Bench

Hutten experienced issues with the TB-5m test bench being dependent on the Centre of Gravity, this was one of the causes of increased measurement inaccuracy during experiments with water compared to the nitrogen testing. To prevent this in the future the TB-50m is selected to be used during this project. This is a horizontal torsional test bench and therefore independent of gravity. It is shown in Figure 2.5, with the LRF 400 load cell in the bottom corner and the Variable-Turn Density Coil (VTDC) at the top. It is located in the clean room. The thrust range of the thruster is expected to be between 5 and 15 mN based on previous work [8, 11]. The TB-50m has a range of 0.5-50 mN $\pm$ 1% [13] and was redesigned and calibrated by Takken [14] in 2021 for a range of 0-12.3 mN $\pm$ 1.43%. The calibration is performed with the VTDC but is limited by the available current of 20 A. The magnet overheats and gives distorted results when more than 16.5 A is drawn for extended periods of time. This issue could be elevated by employing a larger magnet or by elongating the arm to the pivot point. The load cell present in the system can measure up to 100mN. Once the test bench is fully assembled with the thruster it is advised to re-calibrate. To place the thruster on this test bench a new bracket will have to be designed and manufactured, the old one will have to be removed from the thrust structure and the new one glued on.

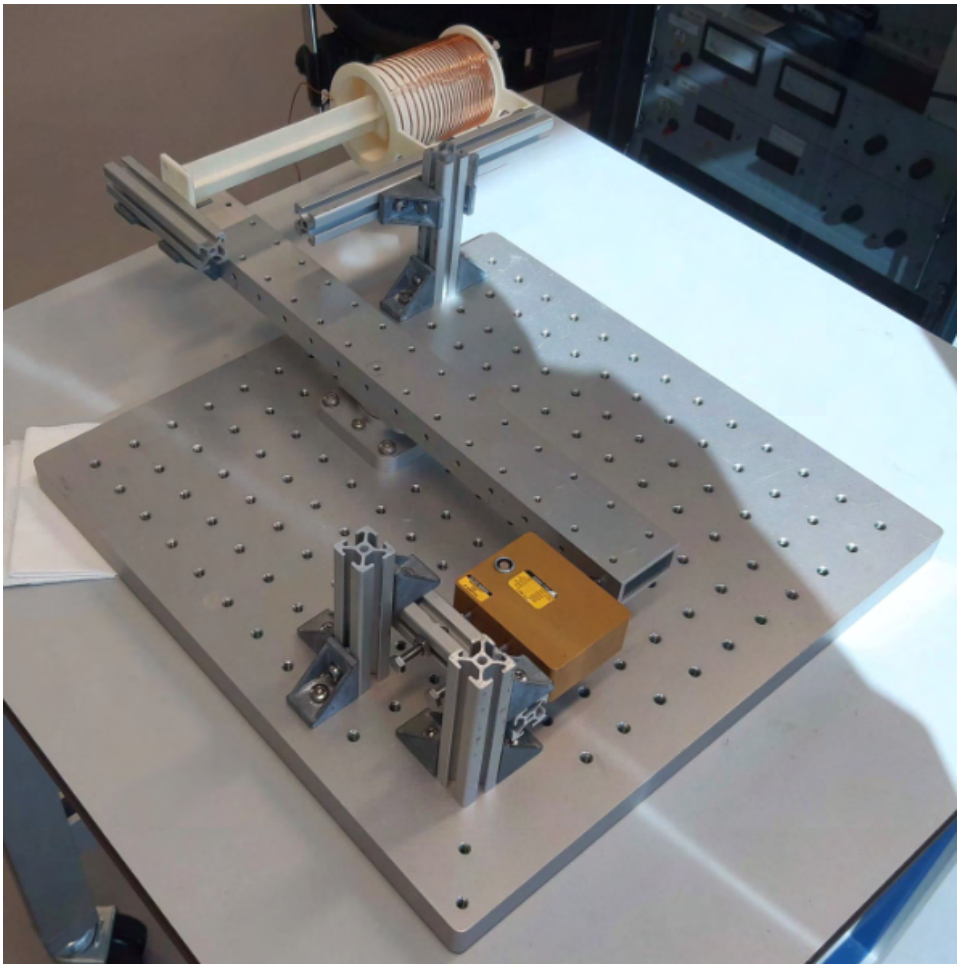

Figure 2.5: TB-50m constructed by Takken [14]

3

Analytical model

To design a thruster an analytical model is set up, experiments serve the purpose of validating this model. The goal would be to have an analytical model that computes the performance of a thruster, such that a design that complies with performance criteria of a spacecraft can easily be computed. The analytical model presented in this chapter is based on the equations taught by Zandbergen [15], Makhan [7] implemented the model and modifications were made by Versteeg [8], Hutten [11], and Pappadimitrou [9] in further thesis research. First, the analytical model itself will be explained, the way error propagation is employed will be described and finally the results will be verified by those obtained by Hutten.

3.1. Model set-up

The analytical model used here will be heavily based on the work from Hutten, a more elaborate description of the model can be found in [11], Chapter 2. The model starts with Ideal Rocket Theory (IRT), which is a simplification of reality based on several assumptions. This theory provides an adequate estimation of the motor performance and will be paired with correction factors which account for real-world deviations from ideal behaviour. These correction factors include the discharge coefficient and nozzle quality. Special attention is given to the selection of throat Reynolds number and picking the correct dimension to describe the planar nozzle profile. Given the thruster's 2D nozzle profile, particularly on this microscopic scale, significant viscous losses occur in the boundary layer.

3.1.1. Ideal Rocket Theory

Ideal Rocket Theory is based on the following assumptions. These assumptions will be revisited later on, and their effect on the model will be explained [15]:

- The propellant is a calorically ideal gas
- The nozzle flow is isentropic
- The nozzle flow is 1-dimensional
- Flow velocity is purely axial
- Propellant in the chamber has a negligible velocity

The equations described below are used to understand the fundamental behaviour of rocket propulsion. They describe the relation between propellant composition (γ, M, R_A), nozzle expansion ratio (A_e/A_t), and chamber conditions determined by temperature (T_c) and pressure (P_c). With the continuity equation and Poisson's equations, it can be derived that the mass flow ($\dot{m}_{ideal}$) can be described by Equation 3.1. The ideal exhaust velocity (U_e) is based on the energy equation and can be computed with Equation 3.2. The heat capacity ratio is described by γ, for nitrogen this equals 1.4. The molecular weight for nitrogen is M = 28.0134 kg/mol, and the universal gas constant is R_A = 8.314 J/Kmol. Γ describes the Vandenkerckhove function given by Equation 3.3.

$$\dot{m}_{ideal} = p_c \cdot A_t \sqrt{\frac{\gamma \cdot M}{R_A \cdot T_c} \left(\frac{2}{\gamma+1}\right)^{\frac{\gamma+1}{\gamma-1}}} = \frac{\Gamma p_c A_t \sqrt{M}}{\sqrt{R_A T_c}} \tag{3.1}$$

$$U_e = \sqrt{\frac{2\gamma}{\gamma-1}\frac{R_A T_c}{M}\left[1-\left(\frac{p_e}{p_c}\right)^{\frac{\gamma-1}{\gamma}}\right]} \tag{3.2}$$

$$\Gamma = \sqrt{\gamma\left(\frac{2}{\gamma+1}\right)^{\frac{\gamma+1}{\gamma-1}}} \tag{3.3}$$

Taking into account non-optimal expansion the equation for thrust is given by Equation 3.4. Combining this with the previous equations provides the variables necessary to determine the thruster's performance.

$$F_{ideal} = \dot{m}_{ideal} U_e + (p_e - p_a)\cdot A_e \tag{3.4}$$

$$= p_c A_t \sqrt{\frac{2\gamma^2}{\gamma-1}\left(\frac{2}{\gamma+1}\right)^{\frac{\gamma+1}{\gamma-1}}\left[1-\left(\frac{p_e}{p_c}\right)^{\frac{\gamma-1}{\gamma}}\right]} + (p_e - p_a)\cdot A_e \tag{3.5}$$

This means that the thrust depends on the propellant composition, nozzle expansion ratio and chamber conditions. The nozzle expansion ratio is given by Equation 3.6 and describes the relation between the area expansion ratio and pressure ratio between the exit and the chamber.

$$\frac{A_e}{A_t} = \frac{\sqrt{\gamma\left(\frac{2}{\gamma+1}\right)^{\frac{\gamma+1}{\gamma-1}}}}{\sqrt{\frac{2\gamma}{\gamma-1}\left(\frac{p_e}{p_c}\right)^{\frac{2}{\gamma}}\left[1-\left(\frac{p_e}{p_c}\right)^{\frac{\gamma-1}{\gamma}}\right]}} \tag{3.6}$$

A parameter often used to describe engine behaviour is the specific impulse (I_{sp}), this describes the total impulse per unit propellant. It is a measure of how efficiently the engine converts propellant into energy. g_0 is the gravitational constant on Earth, with a value of 9.80665 m/s^2

$$I_{sp} = \frac{F}{\dot{m}\cdot g_0} \tag{3.7}$$

An important quality of rocket engines is that they reach sonic conditions in the throat. This condition where Mach equals one creates a choked flow and prevents the downstream conditions from influencing upstream. In other words, a change in ambient pressure will not influence the mass flow for a fixed chamber pressure, therefore creating stable engine operation conditions. It also ensures that the maximum achievable mass flow is obtained in the throat, adding more energy to the flow will not result in an increase in mass flow at this point. This allows the thruster to operate at high efficiency. The pressure in the throat can be computed with Equation 3.8, and the condition for choked flow is shown in Equation 3.9.

$$\frac{p_t}{p_c} = \left(\frac{2}{\gamma+1}\right)^{\frac{\gamma}{\gamma-1}} \tag{3.8}$$

$$\frac{p_c}{p_e} > \left(\frac{\gamma+1}{2}\right)^{\frac{\gamma}{\gamma-1}} \tag{3.9}$$

For the critical pressure ratio, the flow through the nozzle is supersonic and the relation between throat area and chamber pressure can be written as Equation 3.10. With the help of the Poisson's relation Equation 3.11, the exhaust velocity at any point in the nozzle can be computed. This rewrites Equation 3.2 with the maximum obtainable exhaust velocity in vacuum Equation 3.13.

$$A_t = \frac{1}{\Gamma}\cdot\frac{\dot{m}\sqrt{\frac{R_A}{M}\cdot T_c}}{p_c} \tag{3.10}$$

$$\frac{T}{T_c} = \left(\frac{p}{p_c}\right)^{\frac{\gamma-1}{\gamma}} \tag{3.11}$$

$$U = U_{max}\cdot\sqrt{1-\left(\frac{p}{p_c}\right)^{\frac{\gamma-1}{\gamma}}} \tag{3.12}$$

$$U_{max} = \sqrt{\frac{2\gamma}{\gamma-1}\frac{R_A T_c}{M}} \tag{3.13}$$

3.1.2. Correction factors

During experiments the thruster performance will be different from that predicted by ideal rocket theory. Flow through the nozzle is not isentropic in practice, and flow will not be perfectly expanded in the nozzle. Furthermore there are boundary layers, heat transfer losses, and friction effects. The exact effect of each of these physical processes on the previously made assumptions is hard to quantify, this is why their effect is quantified by comparing the ideal and experimental results. Several characteristic parameters are set up for this purpose.

The characteristic velocity c^* represents the effective exhaust velocity of the thruster, it is a measure of the energy level of the propellant independent of nozzle performance, given in Equation 3.14. The thruster coefficient C_F is a measure of the efficiency of the propulsion system in transforming the mass flow rate of propellant into thrust, shown in Equation 3.15.

$$c^* = \frac{1}{\Gamma}\sqrt{\frac{R_A T_c}{M}} \tag{3.14}$$

$$C_F = \frac{F}{\dot{m} \cdot c^*} \tag{3.15}$$

With these characteristic parameters, correction factors can be defined. These correction factors determine the ratio between ideal ($_{ideal}$) and experimental ($_{exp}$) results and can be used to predict the experimental outcome. The combustion quality and nozzle quality are shown in Equation 3.16 and Equation 3.17 respectively. As no chemical combustion takes place inside the resistojet hence ξ_{c^*} is set to 1. The chamber temperature is purely controlled through the power input by the heaters.

$$\xi_{c^*} = \frac{(c^*)_{exp}}{(c^*)_{ideal}} \tag{3.16}$$

$$\xi_{C_F} = \frac{(C_F)_{exp}}{(C_F)_{ideal}} \tag{3.17}$$

$$\xi_{I_{sp}} = \frac{(I_{sp})_{exp}}{(I_{sp})_{ideal}} \tag{3.18}$$

The discharge coefficient, Equation 3.19, is a measure of how the throat area is affected by physical processes. At low Reynolds number the boundary layer can significantly reduce the effective throat area. This reduction decreased the amount of mass flow necessary to obtain a certain chamber pressure.

$$C_d = \xi_{c^*} \frac{\dot{m}_{exp}}{\dot{m}_{ideal}} \tag{3.19}$$

For resistojets, it is relevant to know the efficiency with which heat is transferred to the propellant. One method to calculate this is shown is Equation 3.20. The energy the heaters put into the system is represented by P_{heat}, h_c is the specific enthalpy of the heated propellant in the chamber and h_0 is the specific enthalpy of the stored propellant.

$$\eta_{Heat} = \frac{\dot{m}(h_c - h_0)}{P_{heat}} \tag{3.20}$$

3.1.3. Boundary layer losses

The Reynolds number is a parameter which characterises the flow of the fluid. Flows with equal Reynolds numbers are comparable in terms of flow behaviour. It defines the ratio of inert versus viscous forces within the fluid. Viscous forces are dominant in the boundary layer, this is the layer of flow that is influenced by the presence of the surface. The flow velocity approaches zero at the surface and increases with distance to the wall till the 'freestream' velocity is reached. At the wall this creates shear stresses. The thickness of the boundary layer (δ) is dependent on the viscosity of the fluid. This slow-moving layer of fluid decreases the overall momentum of the thruster compared to the ideal case, in essence, it decreases the effective throat area. The Reynolds number is given by the following formula Equation 3.21 where ρ is the density of the propellant, U the flow velocity in m/s, L is the characteristic length of the cross-section and μ_c the dynamic viscosity of the fluid in the chamber. This can be rewritten to include the mass flow and the area at the location of interest, in this case the throat. The difficulty comes from determining the characteristic length of the throat. The hydraulic diameter is used to describe the geometry of non-circular cross-sections. It ensures that the force balance of pressure and friction forces corresponds to the equivalent circular pipe.

$$Re = \frac{\rho U L}{\mu_c} = \frac{\dot{m} L_t}{\mu_c A_t} \tag{3.21}$$

$$D_{h,t} = \frac{2 W_t H_t}{W_t + H_t} \tag{3.22}$$

To determine the discharge coefficient multiple analytical [16] and (semi-)empirical [17, 18] relations will be compared. Equation 3.23 by Kuluva and Hosack is the simplest in usage, it is valid for $0 \leq r_c/r_t \leq 20$ and $50 \leq \text{Re} \leq 10^4$. It was derived from experiments utilising an axisymmetrical conical nozzle with an inlet and outlet angle of 20°. r_c is the geometrical radius of the throat curvature and r_t is the geometrical throat cross-sectional radius. The relation developed by Tang and Fenn [16] is based solely on an analysis assuming an infinitely long conical nozzle. The equation is experimentally validated and includes the Prandtl number as correction factor. Equation 3.25 has a dependency on the real Reynolds number, Equation 3.27 which requires the iteration of the Reynolds number and discharge coefficient till they converge. This is because the boundary layer thickness decreases the effective throat diameter. The effect this has on the hydraulic diameter is shown in Equation 3.28. The boundary layer thickness is represented by the discharge coefficient as shown in Equation 3.19. Master thesis students previously used both, the results were similar in the past but Equation 3.23 is preferred in usage as it does not require iterations.

$$C_{d,KH} = \left(\frac{r_c + 0.05 r_t}{r_c + 0.75 r_t} \right)^{0.019} \times \left(1 - \left(\frac{r_c + 0.1 r_t}{r_t} \right)^{0.21} \left(\frac{1}{Re_{t,ideal}} \right)^{\frac{1}{2}} (0.97 + 0.86\gamma) \right)$$

(3.23, Kuluva and Hosack)

with

$$Re_{t,ideal} = \frac{\dot{m}_{ideal} \cdot (D_{h,t})_{geo}}{\mu_c \cdot (A_t)_{geo}} \tag{3.24}$$

$$C_{d,TF} = 1 - \left(\frac{\gamma + 1}{2} \right)^{\frac{8}{4}} \left(\frac{4\sqrt{6}}{3} + \frac{8(9 - 4\sqrt{6})}{3(\gamma + 1)} \right) \frac{1}{\sqrt{Re_D^*}} + \frac{2\sqrt{2}}{3} \frac{(\gamma - 1)(\gamma + 2)}{\sqrt{\gamma + 1}} \frac{1}{Re_D^*}$$

(3.25, Tang and Fenn)

with

$$Re_D^* = Re_{t,real} \sqrt{\frac{r_t \mu_c^2}{(Pr) r_c \mu_t^2}} \tag{3.26}$$

$$Re_{t,real} = \frac{\dot{m}_{ideal} \cdot (D_{h,t})_{eff}}{\mu_c \cdot (A_t)_{geo}} \tag{3.27}$$

$$(D_{h,t})_{eff} = \frac{2 W_t H_t C_d}{\sqrt{4 W_t H_t C_d + (W_t - H_t)^2}} \tag{3.28}$$

Boundary layer losses do not only occur in the throat but they are present over the entire divergent part of the nozzle. The nozzle quality is related to divergence losses occurring due to non-ideal expansion and anisotropic flow in the nozzle. This effect is described by an empirical relation developed for 2D, thin micro-thrusters by Spisz, Brinich and Jack [19]. Equation 3.29 is developed for conical nozzles with an area ratio between $25 \leq A_e/A_t \leq 150$ with a half angle of 20°, hydrogen was used as propellant and results were accurate within 5%. This equation accounts for the viscous drag and heat transfer losses to the nozzle wall.

$$C_{F,loss} = 17.6 \exp\left(0.0032 \frac{A_e}{A_t} \right) (Re_{t,wall})^{-0.5} \tag{3.29}$$

with

$$Re_{t,wall} = \frac{C_d \mu_c}{\mu_t} Re_{t,ideal} \left(\frac{T_t}{T_{t,wall}} \right)^{5/3} \tag{3.30}$$

Here T_t is the temperature of the propellant gas and $T_{t,wall}$ the temperature of the nozzle wall. As the thruster is heated in its entirety this can be approximated to be equal to the chamber temperature. A_e/A_t is the geometric expansion ratio of the nozzle. The $C_d \mu_c/\mu_t$ stems from the definition of the Reynolds number used in Spizs et al [19]. It uses the real mass flow but geometric throat dimensions and throat viscosity. Combining Equation 3.8 and Equation 3.9 which govern throat conditions the temperature

fraction can be rewritten, shown in Equation 3.31. This allows Equation 3.29 to be rewritten in known parameters in Equation 3.32.

$$\frac{T_t}{T_{t,wall}} \approx \frac{T_t}{T_c} = \frac{2}{\gamma + 1} \tag{3.31}$$

$$C_{F,loss} = 17.6 \exp\left(0.0032 \frac{A_e}{A_t}\right) \left(\frac{C_d \mu_c}{\mu_t} Re_{t,ideal}\right)^{-0.5} \left(\frac{2}{\gamma + 1}\right)^{-5/6} \tag{3.32}$$

Gases exiting the nozzle divert from the nozzle throat to the nozzle exit. This means that there is an axial and radial velocity component to the gas particles. This opposes the purely axial flow assumption that is made in ideal rocket theory. The amount of diverting losses depends on the nozzle shape and the angle of the nozzle wall. For a conical nozzle this can be computed with Equation 3.33 as analytically derived by Berton [20]. Where θ is the nozzle divergence angle of 20°. Resulting in a C_θ of 0.98, or a 2% loss from the ideal case. This factor and the losses due to heat transfer and friction are incorporated into the estimated ($_{est}$) thrust coefficient with Equation 3.34. The nozzle quality factor becomes Equation 3.35, which is the estimated real case divided by the ideal case.

$$C_\theta = \frac{\sin\theta}{\theta} \tag{3.33}$$

$$C_{F,est} = C_\theta C_{F,ideal} - C_{F,loss} \tag{3.34}$$

$$\xi_{C_{F,est}} = \frac{C_{F,est}}{C_{F,ideal}} \tag{3.35}$$

3.2. Error propagation

As presented in section 5.2, real-world measurements have an uncertainty induced by the sensors and actuators used to obtain data. To be able to tell whether the theoretical model predicted the experimental results correctly this uncertainty will also be introduced into the theoretical values. The confidence interval used in this research is a range where 99.7% of the measurements will fall within if they are normally distributed around the mean value, $\bar{x} \pm 3\sigma$. The standard deviation (σ) can be computed with Equation 3.36 [21]. Here $\bar{x}$ is the mean value, x_i is the value of the i-th measurement and N is the total amount of measurements [21]. Uncertainties provided on data sheets are generally given in terms of 3 σ. The normal distribution can be displayed as Figure 3.1[1].

$$\sigma = \sqrt{\frac{\sum_i^N (x_i - \bar{x})^2}{N - 1}} \tag{3.36}$$

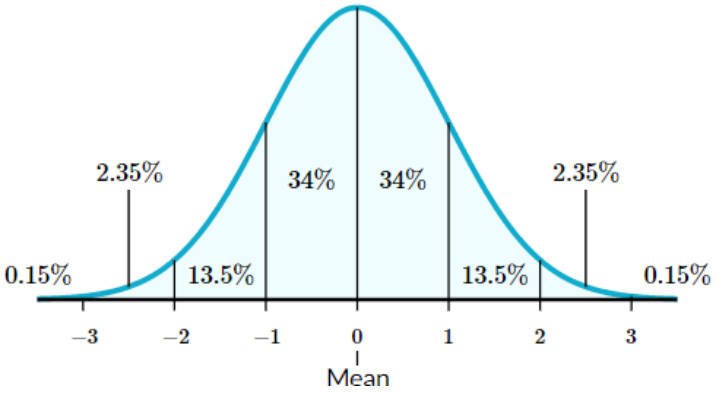

Figure 3.1: Normal Distribution

In the theoretical model uncertainties have to be passed on through mathematical operations. If A and B are variables with errors σ_A and σ_B, and σ_f is the error of resulting variable f, Equation 3.37 can be used to describe how errors are propagated throughout the model.

[1] https://www.khanacademy.org/math/statistics-probability/modeling-distributions-of-data/normal-distributions-library/a/normal-distributions-review

$$\left.\begin{array}{l} f = A + B \\ f = A - B \end{array}\right\} \Rightarrow \sigma_f = \sqrt{\sigma_A^2 + \sigma_B^2}$$
$$\left.\begin{array}{l} f = A \cdot B \\ f = A/B \end{array}\right\} \Rightarrow \sigma_f = |f|\sqrt{\left(\frac{\sigma_A}{A}\right)^2 + \left(\frac{\sigma_B}{B}\right)^2} \tag{3.37}$$

These equations are only valid for independent errors, which is not always the case in the model. For example, the temperature is used to determine γ and both γ and the temperature are used to compute the characteristic velocity c^* in Equation 3.14. Using Equation 3.37 would overestimate the error. That is why in the model by Hutten a Gaussian distribution of randomised input parameters is used. The calculations are run many times to generate a distribution from which the standard deviation can be computed. While determining the error of the output parameters with this method may not yield exact results, repeated iterations of this process will gradually converge towards the accurate value.

3.3. Model Verification

Code from Hutten [11] was used to replicate the analytical model. This code was retrieved from the GitHub repository RickHutten/ResistojetPerformanceTool. The code had to be slightly modified to replicate the analytical model results as it is configured to analyse TDMS files from the experiment. The input geometry is that of the thruster Versteeg produced for heated experiments. The table found on page 12 of Hutten was used as a verification tool that the output of the code was as expected. Both the values of the parameters and the uncertainties could be exactly replicated as shown in Table D.1 in the appendix. One should keep in mind that the uncertainties are determined via a Gaussian distribution of inputs, this creates a variability of $\pm$ 0.01 between code runs. The uncertainty is also dependent on the number of iterations, at least 100,000 are recommended.

Some constant values that are used throughout the rapport and that can be used to replicate these values are shown in Table 3.1. It should be evident that the specific heat ratio and chamber viscosity depend on temperature. These values are determined via Coolprop based on thrust chamber conditions.

Variable	Symbol	Value	Unit
Constants			
Molar mass	M	28.013	g/mol
Universal gas constant	R	8.31446	J/(K·mol)
Dynamic chamber viscosity	$\mu_{c,305.5°K}$	18.147	mg/(m·s)
Dynamic chamber viscosity	$\mu_{c,670.7°K}$	31.905	mg/(m·s)
Specific heat ratio	$\gamma_{305.5°K}$	1.402	-
Specific heat ratio	$\gamma_{670.7°K}$	1.374	-
Standard gravity	g_0	9.80665	m/s^2
Relevant geometry			
Throat radius of curvature	r_c	260	μm
Throat cross-sectional radius	r_t	$D_{h,t}/2$ = 144	μm

Table 3.1: Inputs analytical model

4

Detailed Design

In the literature study, several areas of improvement were defined, and concepts were selected to be implemented. In this chapter, the applicability and feasibility of those concepts are looked into and the thruster is modified accordingly. The execution and implementation of these changes are discussed afterwards. Tools are obtained from either the clean room and connecting workshop or the Aircraft Hall (ACH). Tools were also occasionally used from Delft Aerospace Rocket Engineering (DARE), as the author is a member of this society.

4.1. Heater selection & implementation

The intention was to implement both heater solutions identified during the literature study [10], meaning both the cartridge heater and mica paper would be used to heat the propellant. The results of these methods could be compared in terms of efficiency and achievable temperature. In previous work cartridge heaters were always available and thus used to heat the thruster. To evaluate the usage of other heaters, the required heating power is computed. This is done with Equation 4.1 [15], the energy required (Q_{req}) to heat up the propellant to the desired 400°C is equal to the energy necessary to raise the temperature (H_t°) plus energy of vaporisation (H_{vap}). The mass flow rate ($\dot{m}$) taken for water is 9 mg/s as computed by Hutten [11]. The enthalpy is given in kJ/mol and obtained from NIST data and the mass flow is converted to mol/s with the molecular weight of 18.0153 g/mol [22]. The amount of energy per second that needs to be put into the water than becomes 27.1 J/s, with an efficiency of 70% as determined by Hutten this means that the heater should supply 38.7 W. These calculations are in the same range as the required heating power found by Hutten for 300°C. The required energy can be divided between two heaters, as each block is heated individually.

$$Q_{req} = n \cdot (H_t^\circ - H_{298}^\circ) = \dot{m} \cdot (H_4^\circ 00 + H_{vap}) = 27.1 J/s \tag{4.1}$$

The data sheet of the mica ceramic paper patch heaters[1] reports a maximum Watt density of 17 W/cm^2, with a minimum size of 10 x 20 mm. This poses a problem due to the irregular surface of the thruster. The biggest square patch that would fit is 12x14 mm which is not sufficient, besides this is not enough surface area to deliver the required power. To be on the safe side, in case the efficiency computation was off from Hutten, a safety factor of 1.2 was taken and heaters with a combined power of 50 W were investigated. As the top surface has insufficient surface area that idea was discarded, and a heater that would wrap around the circumference of the thruster was considered.

Mica paper heaters differ from regular flexible heaters in the fact that they do not have an adhesive side. This type of heater will have to be clamped with a plate to the surface to ensure equal heat distribution, this so-called backing plate should be either stainless steel or aluminium, aluminium comes with the risk of distortion when being used at high temperatures. After initial start-up, the inorganic binder of the mica paper will burn up and some smoke will be visible. Once the heater has been turned on, disassembly may result in layer separation and breakage of the heater. The potentially foreseen

[1] https://www.kawaidenki.co.jp/english/products/et_600.html

issue here is the 0.5mm gap between the copper blocks and the need to clamp the design. This would have to be a custom-made part, and threaded holes would have to be added to the copper block. The heater would have to be pre-formed to the copper block's circumference. As the aim of this project is to use readily available components, that require little effort to implement in order to save time, this was not deemed a feasible solution and the idea was disregarded.

Cartridge heater

In order to secure the heater to the structure a thread should be added to the cartridge heater. To prevent modification of the copper blocks, it is chosen to attach an external thread and make a threaded sleeve for the cartridge heater. The simplest method would be to take a bolt, cut off a threaded piece and drill a hole. A threaded rod would also be a suitable solution. The final selection will be dependent on the availability of components. The external thread can be taken from a nut which is secured to the copper blocks. It is important that the nut does not block the nozzle exit otherwise one will have to file or lathe down the nut.

The official cartridge heater diameter is 3.1mm, in practice it is found to be slightly oval, the company provides a tolerance of $\pm$ 0.05 mm. The hole in the copper block is designed to be 3.1mm, but this was found quite a loose fit by Hutten [11]. Dimensions of the cartridge heater can be found in section B.1 and the copper block in section E.2. No real force will be applied to the thread, its purpose is merely to hold the cartridge heater in place. Thus the strength of the bolt is not relevant. The material is required to be a good conductor as the heater will break when it can not dissipate the generated heat. Bras, copper, steel or aluminium would be good choices.

Rob van der List from Dienst Elektronische en Mechanische Ontwikkeling (DEMO) recommended using either brass or copper material for the nut to be attached to the copper block. The attachment method that they can provide is gas torch brazing. This is also how the steel tubes are attached to the copper sealing blocks. It requires the entire copper block to be heated up above the melting temperature of the copper. Oxidation is expected. Hence this process should take place before polishing. DEMO has brass round and hex stock available as well as brass M6 bolts.

Thermal Adhesive

Next to securing the heater to the structure, it should have a snug fit inside the hole to promote conduction. It was found that normal thermal pastes, used to cool CPU's of computers, have a temperature limitation of around 150°C. A suitable product was found from Thermal Management and inquiries were made. They recommended a product with, in their words, a viscosity similar to toothpaste or jam, of 30 mPa·s. In combination with the high surface tension that Gallium possesses it seems unlikely that it will leak through the thread. The composition of this product is a Gallium-Indium-tin alloy. Under the conditions of 400°C and 10 Pascal pressure, none of these components reach their respective vapour pressure [2]. The purchase price was €300, excluding VAT and customs.

Heating the propellant line

The idea was presented to heat the water in the propellant line, such that vapour enters the thruster. This would give a steadier thrust curve as water droplets lead to a sudden pressure increase and corresponding thrust rise. There are two perceived issues. One is that attached to the 'cold' side is a pressure sensor with a maximum rating of 85°C. Thus if the steel tube leading to this 'cold' connection is heated up, this will most likely lead to overheating of the pressure sensor. A heating test has been performed by Hutten [11] in which the temperature of the top interface is recorded. There is delayed heating, but after the thruster block reaches (454 $\pm$ 6)°C, the top interface reaches temperatures of (72 $\pm$ 4)°C. Putting heat into the propellant line, closer to the top interface, is therefore not an option in the current configuration.

If this connection is modified the second problem is that the propellant valve has a temperature rating of 49°C. The PTFE/Teflon tubing has a low thermal conductivity and an estimated melting tem-

[2] https://www.mbe-komponenten.de/selection-guide/vapor-pressure.php

perature of 260°C [3]. The original supplier is unknown, therefore data was taken from a comparable product.

Due to time constraints and the amount of redesign it would take to implement, propellant heating inside the feed line was disregarded. Instead it was decided to add foam to the propellant line, this will promote the conduction to the water in the propellant line as there is more surface available. Versteeg [8] has previously made foam inserts for the pressure sensor line, to prevent the pressure sensor from overheating. The foam is available in the dedicated box to this project in the clean room workshop. This contains instructions for the cutting speed. Instructions are provided by Versteeg on laser cutting speed and manufacturing of the foam inserts.

Mesh

Hutten recommended putting mesh in the thruster to prevent future nozzle blockage. The mesh was acquired from van Rooy & Co in Schiedam, they were consulted over the phone and it is advised to come by. As the nozzle's smallest dimension is 130 μm it was decided to go for the 110 μm mesh width with a wire thickness of 60 μm of RVS 304. This should stop any impurities from blocking the nozzle. As it was only a minuscule piece that was required (12 x 5.5 mm), the author was allowed to cut a strip of mesh from the roll free of charge. Normally this type of mesh is sold by the roll for air filtration systems.

4.2. Test bench

The TB-50m was selected for testing as this would mitigate the dependency on the Centre of Gravity for measurements. The current structure is not suitable to be attached to the test bench as it was constructed for pendulum attachment to the TB-5m. When designing a new construction, one should pay attention to the way load is introduced onto the torsion pendulum. If moments or bending is present, not all produced thrust will be registered by the load cell. The steel tubes are designed to be rigid and prevent bending. From any potential structural connection to the thermal shield the same cannot be said.

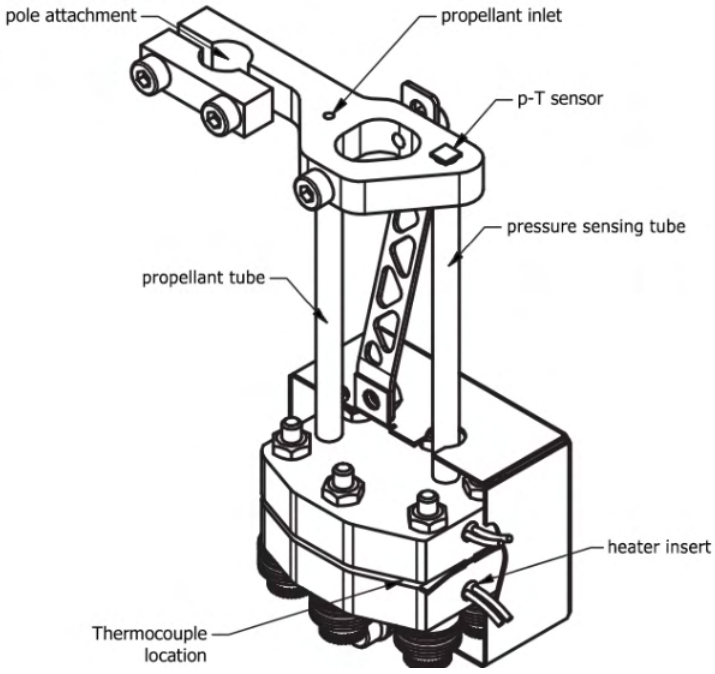

Figure 4.1: Thruster construction as devised by Versteeg [8]

[3] https://www.curbellplastics.com/materials/specialty-products/tubing-hose/ptfe-tubing/

It was decided to place the thruster upside down on the structure. The torsional pendulum has two rows of regularly spaced threaded holes on top, threaded holes are also present on the side. A square aluminium structure was designed, using the old drawing as indication of hole dimensions and position. A groove was made for the propellant feed line and pressure sensor electronic wires. Four holes are present to attach it to the pendulum for even weight distribution and a secure connection. The technical drawing can be found in section E.2.

4.3. Execution

With all elements thought out and designed it was time to start the practical work. In this section, the execution of adjusting the thruster and test bench will be presented and any issues that were run into will be discussed.

4.3.1. Disassembly

The first difficulty that was encountered was the disassembly of the cold part of the thruster. The cold part of the construction consists out of glued connections with the plastic feed line, pressure sensor and two steel connections. The metal glue used for these connections is rated up to 125°C, however the pressure sensor is only rated up to 85°C. The connection of the steel tubes to the thruster is brazed. This means that on neither side the connection can be undone without cutting into the metal tube or breaking the pressure sensor. The thesis of Versteeg [8] was consulted on the temperature profile along the tube. As can be seen in Figure 4.2, with the selected tube length of 55 mm there is a little leeway. Half a centimetre could be cut without risking the function of the pressure sensor.

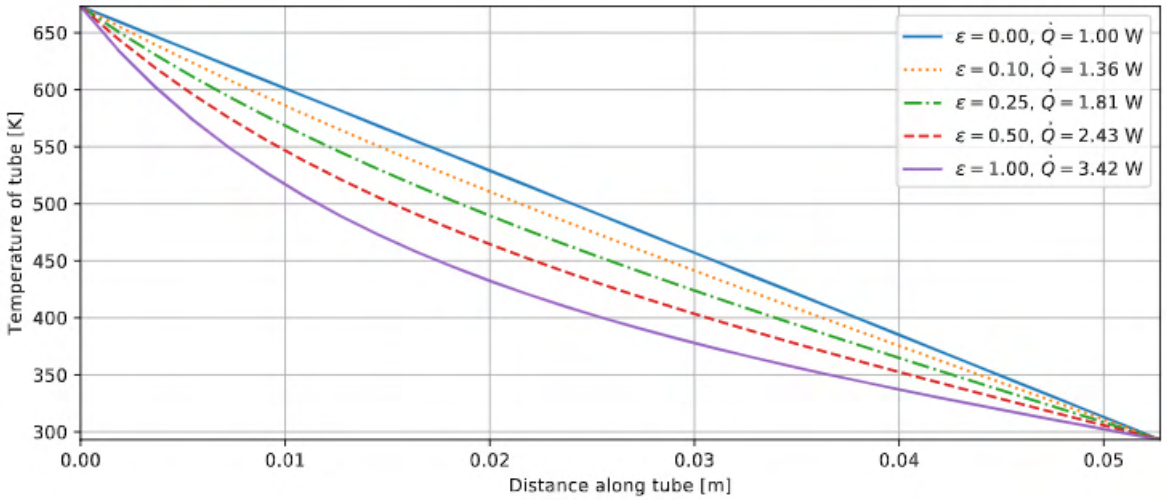

Figure 4.2: Temperature profile along connecting tubing from thruster body (left) to interface (right) with corresponding heat loss values. Conditions shown vary from pure conduction (η =0) to the outside of the tube acting as an ideal black body (η = 1) [8]

With this in mind another obstacle was discovered. The cut tubes had to be even and level for re-assembly or the thruster would be unevenly mounted. Due to the size of the thruster a hand saw was thought to be the best way to cut them, however the chance of obtaining a clean cut are slim with this method. The pressure sensor data sheet was consulted and it was found that for a maximum of 40 seconds a higher temperature could be sustained by the sensor. A maximum soldering temperature of 250°C was listed. Thus for a short period of time a higher temperature could be sustained.

It was decided to try and take off the cold bracket with a heat gun. In the best case the sensor could be reused, and in the worst case it breaks. With cutting the tubes, the sensor stays attached to an unused aluminium piece and will not be used again anyway. From Versteeg's cost breakdown it was known that the pressure sensor was 19 euro thus this was found to be a very reasonable risk. The thruster was lightly clamped in a vice, in hindsight some dampening material could have been in between the copper and the vice to protect it from damage. The heat gun was pointed upwards toward

the bottom of the block and a pair of tweezers was used to take off the pressure sensor and Teflon tube. A wrench was used to wiggle the aluminium bracket off. The open tubes were covered with painters tape to prevent dirt from entering and to restrain the foam inserts in the propellant tube line. During inspection of the aluminium bracket it was found that the pressure sensor had broken in two parts. This was regrettable, but a back-up pressure sensor was luckily already present.

To braze on the threaded components it was required to take apart the entire thruster. Gas torch brazing creates oxidation thus polishing of the copper seal would be necessary afterwards. This was also done to prevent clogging the nozzle throat. As the thruster was taken apart, the opportunity was taken to inspect the sealing surface of the copper block. This provides information on the degradation of the material since the construction in 2020 and indicates the state to which it should return too after polishing. Roughness on the surface enhances the boundary layer and thereby lowers the thrust. The copper blocks were studied underneath microscopes available in the physics lab in the Aircraft Hall (ACH). The Keyence Laser Scanning Confocal Microscope combines optical and laser equipment to provide the best image. It was decided to try this newer microscope instead of the Keyence VR-5000 in the hope to raise the resolution with respect to the previous theses, and thereby the accuracy of the image. The results can be found in section 6.1, where all microscope usage is explained.

After disassembly, it became clear that the sealing surface had aged differently than the throat area. There was a clear distinction visible on the thruster as can be seen in Figure 4.3. The throat area no longer had a shiny mirror-like appearance, which it had during assembly recorded by Versteeg [8]. As re-polishing was planned, this was not seen as an issue at the moment.

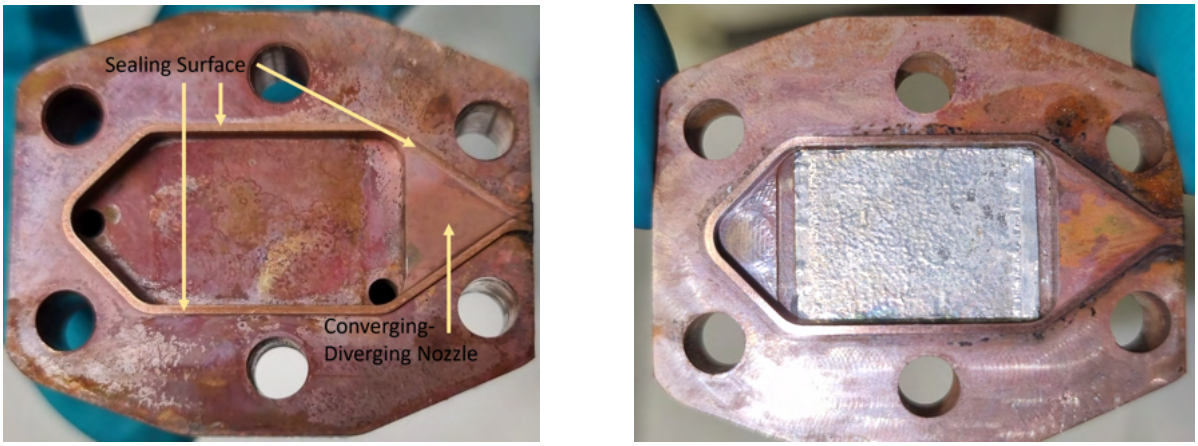

(a) Top **(b)** Bottom

Figure 4.3: Appearance of copper blocks after disassembly

Gaining access to the ACH goes via Gemma van der Windt and an online general safety training had to be followed. To subsequently gain access to specific facilities, the responsible person was approached for instruction. For the polishing equipment this is Roy Awater [4], for the microscopes this is Pietro Marchese[5].

4.3.2. Brazing

A small threaded block was designed to keep the cartridge heater in place. It is important that the block does not obstruct the nozzle exit and does not interfere with the flow. The design was based on a piece of round stock and was designed to be flush with the outside of the copper block.

This piece was made by DEMO and brazed to the copper block. The price estimation of DEMO is 40 euro per hour of work, this was expected to take 2-3 hours. The work proved to be difficult as the hole in the threaded block and previously existing heater hole had to be aligned. The capillary effect

[4] Contact: R.H.P.Awater@tudelft.nl
[5] Contact: P.G.Marchese@tudelft.nl

makes it such that the threaded block floats on the solder. This made it difficult to anchor and resulted in a slight misalignment. As a solution the holes in the conductor blocks were slightly enlarged on a mill. This led to an oval-shaped hole. It was deemed acceptable as it was already decided that thermal paste would be used to fill up the space between the heater and the surrounding copper.

Threaded sleeves

The threaded sleeves were made on the lathe in the ACH by a friend, Andrew Spekreijse. Copper M6 bolts were taken from the wall of bolts, and cut to pieces of 5mm. A 3.1mm hole was drilled for the cartridge heater to fit through. The threaded pieces had to be filed manually as after cutting the thread was slightly deformed. Three parts were made, so there was a spare.

The threaded sleeves are attached to the cartridge heater with high temperature sealant, normally used for fireplaces and resistant up to 1200°C. It was taken into consideration that the paste has a base of sodium silicate with a low thermal expansion coefficient. But since it will be a very thin layer inside the threaded sleeve, this should not prove a hindrance to the heat conduction.

Foam inserts

The original file from Versteeg was used, the idea is that there are small bridges between the inserts so they stay together as one piece and are not blown away by the blowing air of the laser cutter machine. Afterwards, they can be broken apart with little force and rolling them over a table will return them to the round shape necessary to insert them into the tube.

At the Faculty of Mechanical, Maritime and Materials Engineering (3ME) there is an Inloop Werkplaats Studenten (IWS) where students are free to work on projects and personnel is available to assist. For most tools, a course will have to be taken before one is able to work there. However for the laser cutter you can provide the staff with a DXF file and they will assist you with production. A new laser cutter had been acquired since Versteeg's project, thus the provided settings no longer applied. An experienced staff member assisted and several test pieces were made. Unfortunately, the bridges between foam inserts did next to nothing to keep them together and the inserts were blown through the machine. After the first test piece was cut, the machine was thoroughly emptied of scrap metal pieces as it was impossible to find the blown away singular foam inserts. Afterwards, most inserts could be recovered from each test piece made. Between each test piece the cutting speed was doubled, starting at 25 mm/s and ending at 200 mm/s. The speed determines how much of the material is actually cut, thus increasing the speed should mean there is more material intact to keep the foam inserts in place. Varying degrees of scorching and deformation of the inserts was noted. The cut did improve at increased velocity. In the end, 4 cuts were made and 25 foam inserts were recovered. The final settings are displayed in Table 4.1.

Cut Height (mm)	Cut Speed (mm/s)	Cut Duty Cycle (%)	Cut Freq (Hz)	Cut Power (%)
1.000	200.000	70	500	80

Table 4.1: Settings of the laser cutter for the final test piece of foam inserts

Pressurised air is directed at the workpiece to blow away any molten material. The standard setting is 5 bar, the final suggestion of the staff was to lower this pressure. Unfortunately the machine had a safeguard, and could not be operated at a pressure of 2-3 bar.

4.3.3. Polishing

Polishing is conducted in the Aircraft Hall (ACH) room 0.29, Surface treatment. The Dap-7 Polishing machine can be reserved via Labservant after receiving instructions. A similar method was employed as Versteeg [8] with diamond polish. This went in steps of 6, 3 and 1 μm. On the corresponding sanding disk a little bit of diamond polish was put with plenty of ethanol as lubricant. Ethanol and not water was selected as lubricant to prevent corrosion. A warning was also given by the instructor that too much diamond polish will cause scratches.

The goal of polishing was twofold, to smooth out both the throat area and the sealing surface. Due to the size of the throat, nozzle viscous effect are dominant. By having a smooth throat surface the boundary layer can be kept minimal. The sealing surface working principle is squeezing the steel thruster plate between two layers of copper. The copper will deform to fill in any holes as it is the softer metal. For this purpose, it is important that the sealing surface is level and even. As mentioned earlier, discolouration was already visible after disassembly, but now it became apparent how severe these issues were.

After the first round of sanding with 6 μm, it was found that the sealing surface was damaged more than expected. This became apparent when the surface did not polish evenly. For the top block, the sealing surface was found to be slanted as the effects of polishing were visible on the throat area and on the back end of the block as is shown in Figure 4.4. On the bottom block, dents in the sealing surface became apparent. This is visible in Figure 4.5. In both blocks, it was visible that the sealing surface was lowered with respect to the throat area. Something that could be caused by over-tightening the screws during assembly. The amount in which the surface was slanted is quantified on the microscope in section 6.1.

Figure 4.4: Top block after polishing with 6 μm

Figure 4.5: Bottom block after polishing with 6 μm

The damaged sealing surface, especially the slanted surface is expected to impact the leakage rate of the thruster. Several options to proceed were identified, the cautionary approach would be to remake the sealing surface side of the blocks by placing them in a CNC and taking off 0.25mm. This is the height of the sealing edge and could be done without impairing the thruster function. This is a costly affair as it would necessitate more involvement of DEMO and take some time to get machined. Another option would be to continue the process and wait to see the leak test results. The bolts could be tightened more, one would have to keep in mind the maximum bolt strength when deciding on the applied torque. Finally, as the copper conducting blocks have proved not to be reliable, reusable prototype, it could be decided to secure the blocks together by another method such as brazing or adding glue or kit. This option will be revisited after leak testing.

For now the polishing process was continued, with the 6 μm and 3 μm polish. The 1 μm polishing disk was damaged, which had a negative effect on the surface finish. After this was found, the polishing was restarted and measurements were performed after each disk. The 1μm step was omitted. The final results can be found in Figure 4.6. After polishing it is important that the copper blocks are kept in an airtight ziplock bag to prevent corrosion and other damage to the surface.

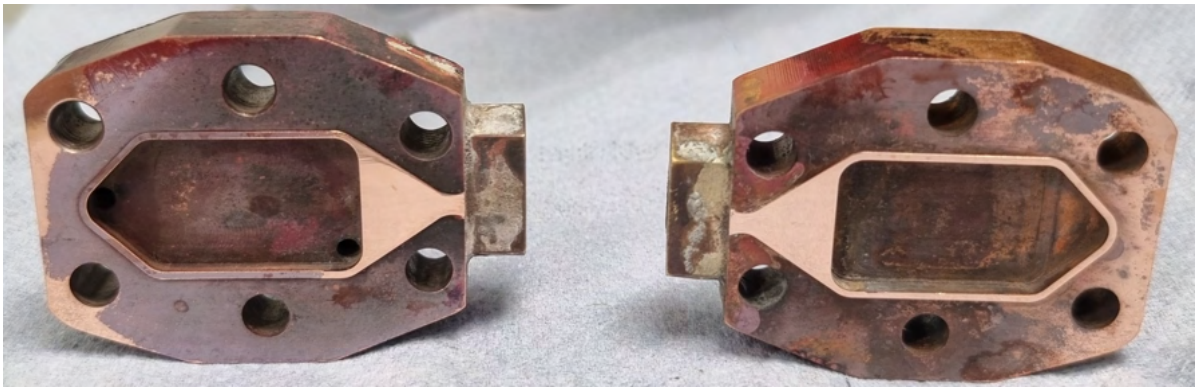

Figure 4.6: Final results of polishing

4.3.4. Assembly

After polishing the sealing blocks are very sensitive to scratching, so the thruster is assembled first and afterwards all other components are added. To facilitate an easily reproducible prototype, assembly procedures are included and a parts list is present in Appendix A. Any discrepancies that occurred during assembly are discussed.

There are two things noteworthy about this assembly procedure. First off Hutten was unable to remove the shoulder bolts in step 6, thus he only used the M4 bolts during assembly. The thruster will be clamped during assembly such that everything stays in place, later during leak testing the tightening of the bolts will be increased. It is important that this is done in a crosswise fashion to prevent uneven load distribution. Versteeg tightened to 1.4 Nm after leak testing, Hutten went to 1.6 Nm. Hence it was decided to start slightly below these values at 1.2 Nm, later during leak testing it was found necessary to increase this to 3.0 Nm with a torque wrench borrowed from Joris Melkert.

The assembly procedures of the thruster are as follows:

1) Put two shoulder bolts in the back most holes of the bottom copper block (furthest from the nozzle)
2) Place foam and mesh inside the bottom block cavity
3) Place thruster profile and top block
4) Insert the shoulder bolts a few mm in top block to assure alignment
5) Insert M4 bolts with springs and washers in the remaining four holes
6) Tighten until layers can no longer move (hand tight)
7) Exchange shoulder bolts for M4 bolts
8) Tighten with an initial value of 1.2 Nm with a torque wrench (FACOM A.402 0.5-2.5 Nm, present in the clean room).

By only hand tightening the bolts, it was possible to remove the shoulder bolts and insert the remaining normal bolts. The layers seemed to be secure in this way. The slanted sealing surface can also be observed in the assembled thruster. The previously present aluminium foil layer, as can be seen in Figure 4.3b and mentioned by Versteeg, is not returned to the thruster. As water is the main propellant of interest, galvanic corrosion might occur and this is an unwanted process. The aluminium foil was used as a spacer to firmly press the foam against the surrounding copper and thereby promote heat conduction. The author found that the foam was quite firmly wedged between the sides of the copper block and hence no other spacer was looked into. The thermocouple was supposed to be squeezed in between the two copper blocks where it is held in place through light compression. However due to leak testing difficulties, this was forgotten and could no longer be achieved after tightening, to prevent undoing the connection completely, only 1 bolt was loosened and the thermocouple was squeezed between a nut and the copper block.

The sensors are attached after it has been confirmed with the LabView software that they are functioning. The test bench bracket is first assembled with the valve and pressure sensor, as final step

the bracket is attached to the thruster. Due to this order, it can be visually verified that glue does not obscure the sensor and propellant line. Glue for the Teflon line has to be used generously or it will not hold. The following procedures are performed to attach all remaining items:

1) Glue Minstac tubing into respective hole with Teflon primer and glue
2) Glue the metal o-ring groove of the pressure sensor into the corresponding hole with metal glue
3) Wait 24 hours for glue to dry
4) Lightly sand the to-be-joined surfaces on the bracket and tubes
5) Apply metal glue: Bison Kombi Metaal
6) Put tubes and bracket together
7) Wait 24 hours for glue to dry

The completed thruster is shown in Figure 4.7.

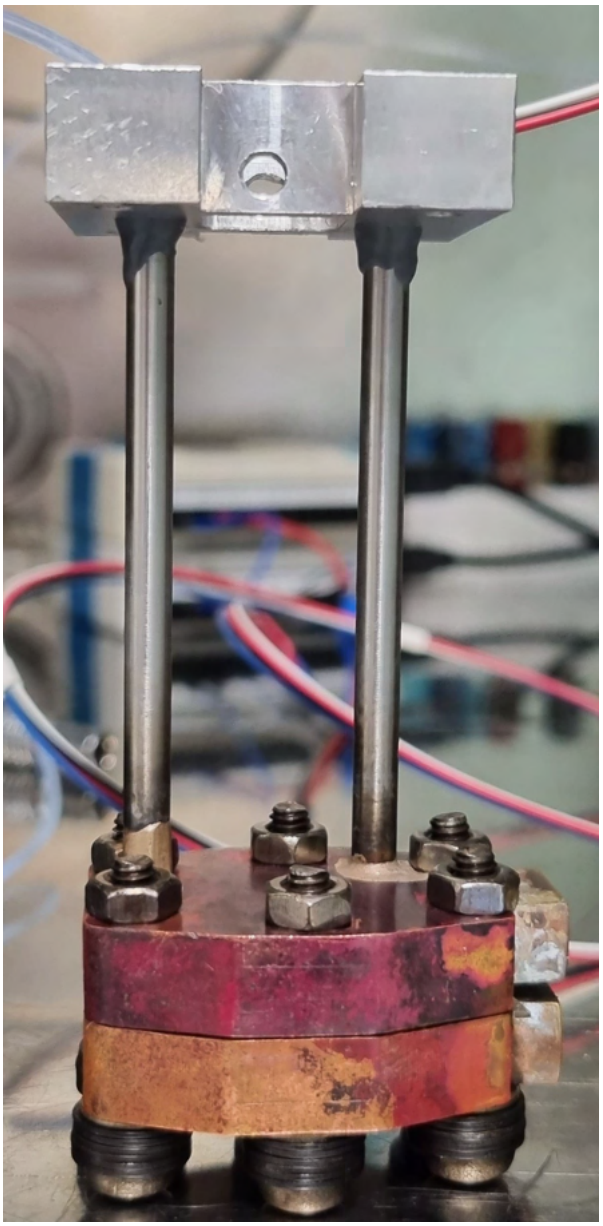

Figure 4.7: Completely assembled thruster with pressure sensor and propellant valve attached

5

Test set-up

A significant aspect of conducting experiments is the test set-up. Hardware has to be collected and code has to be written to control it. A different test bench was employed in this thesis than that the two predecessors had used, in an effort to decrease the measurement inaccuracy. In this chapter, first the hardware used in the set-up is discussed, followed by the confidence bounds of the hardware. Finally the test bench and its calibration are discussed.

5.1. Hardware

During this thesis quite some effort was put into making the test set-up as easy to use as possible. As the thesis experiment had already been conducted twice in a similar manner, the author expected the set-up of the electronics and LabVIEW to be a minimal effort. Unfortunately, documentation was found insufficient for this to be the case. Upon inspection most elements described by Hutten [11] and Versteeg [8] were still present in the clean room. Still, with little previous experience of connecting or operating these sensors, actuators and power supplies this took more time than expected.

First, all instruction manuals of the required items were collected, the most relevant can be found in section B.1. All information with regard to the electronic hardware and software was collected from previous theses. In this section, each piece of hardware and the process of getting it test-ready is discussed.

Sevket Uludag[1], the clean room manager and electrical engineer, assisted in the process of getting the electronics test ready. He advised to make an Electrical Diagram (E.D.) to aid in connecting the system and to have an overview of important information. The hardware connections are the first step to debugging the system. As this will be an electrical diagram used by aerospace engineers pictures were added for clarity, colours were added to the diagram to signal the different functions of elements. The electrical diagram displays the function of each element and their connections. Where necessary, settings or relevant specifications are mentioned. This chapter shows pieces of the electrical diagram, and a picture of the full electrical diagram is placed in section B.2. The electrical diagram turned out to be several pages large and is only readable in PDF. The original file can be requested from the author. The legend is shown in Table 5.1.

[1] M.S.Uludag@tudelft.nl

Legend	
Blue	Sensor or actuator
Red	Power supply
Green	Connector
White with dashed line	Data acquisition
White	In-between device e.g. Break out board, PC, Arduino
Coloured lines represent their physical counter part	

Table 5.1: Legend of the electrical diagram

5.1.1. PC

For this project, the system is controlled with LabVIEW on the offline computer inside the clean room. The desktop has several USB ports which are used for control and data collection of sensors and actuators as well as a NI-PCI-6229 DAQ which is integrated with a PCIe card. The NI PCI 6229 has two connectors and two CB-68LP breakout boards, these connect the mass flow meter and three power supplies to the computer. The boards are shown in Figure 5.1, together with an explanation of the wire connections. The boards have analogue input (AI) and output (AO) channels as well as ground (GND). A specific USB port on the desktop corresponds to a specific import channel on LabVIEW, therefore the USB cables must be placed in the correct ports, otherwise the LabVIEW will malfunction. The two NI plugs also correspond to a specific set of channels 0-15 and 16-31 and can therefore not be switched without consequences. From left to right the USB ports should be connected to:

1. Desktop to screen
2. Experiment feedthrough (Data from the hub inside the vacuum chamber)
3. Arduino that controls the valve
4. Connects to the DAQ 6008 of the load cell

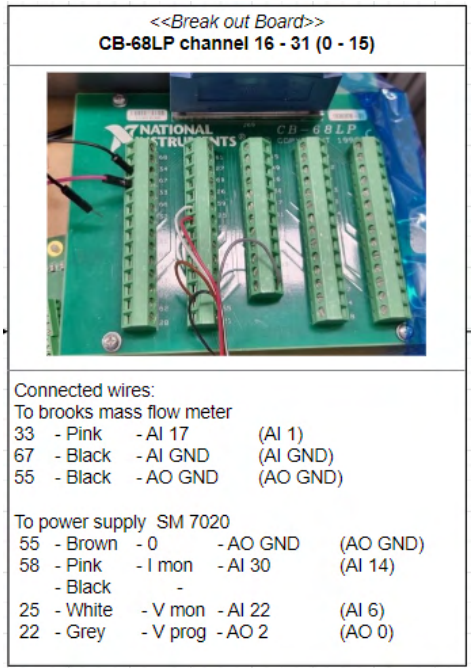

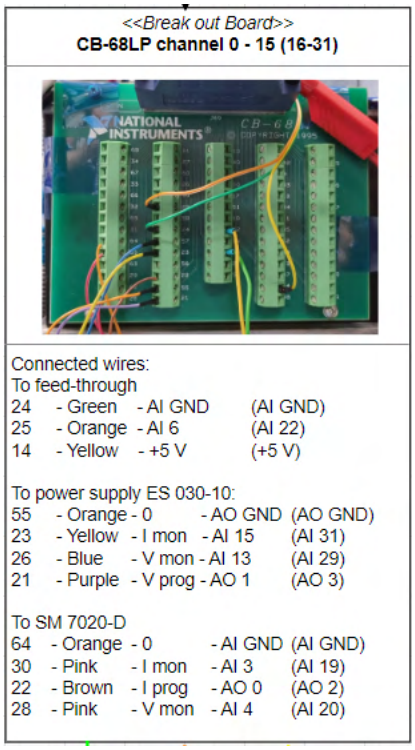

Figure 5.1: Both CB-68LP including the explained connections corresponding to LabView and the power supplies

For any devices going into the computer it should always be checked whether the channels in LabVIEW are correct. Multiple people work in the lab so there is no guarantee that things will stay the same. It is suspected that the two NI 6229 plugs were switched from position, as the old input channel in LabVIEW corresponds to the other connector. If the input channel in LabVIEW is an unconnected port on the breakout board a random irregular value can appear. For future purposes both the corresponding channels have been mentioned in the E.D. such that quick modifications of the LabVIEW can be made.

5.1.2. Thermocouple and Pressure sensor

Documentation on the pressure sensor I^2C bus connection can be found in the thesis by Versteeg [8], section 5.7. The pressure sensor requires pull-up resistors, this circuit was already integrated and is present underneath blue tape. The DAQ devices are connected with a USB B - USB A cable to a hub inside the vacuum oven, information exits the oven via the experiment feedthrough with an USB A - USB A cable that can be connected to a computer USB port. The pressure sensor and thermocouple connection inside the vacuum chamber are shown in Figure 5.2.

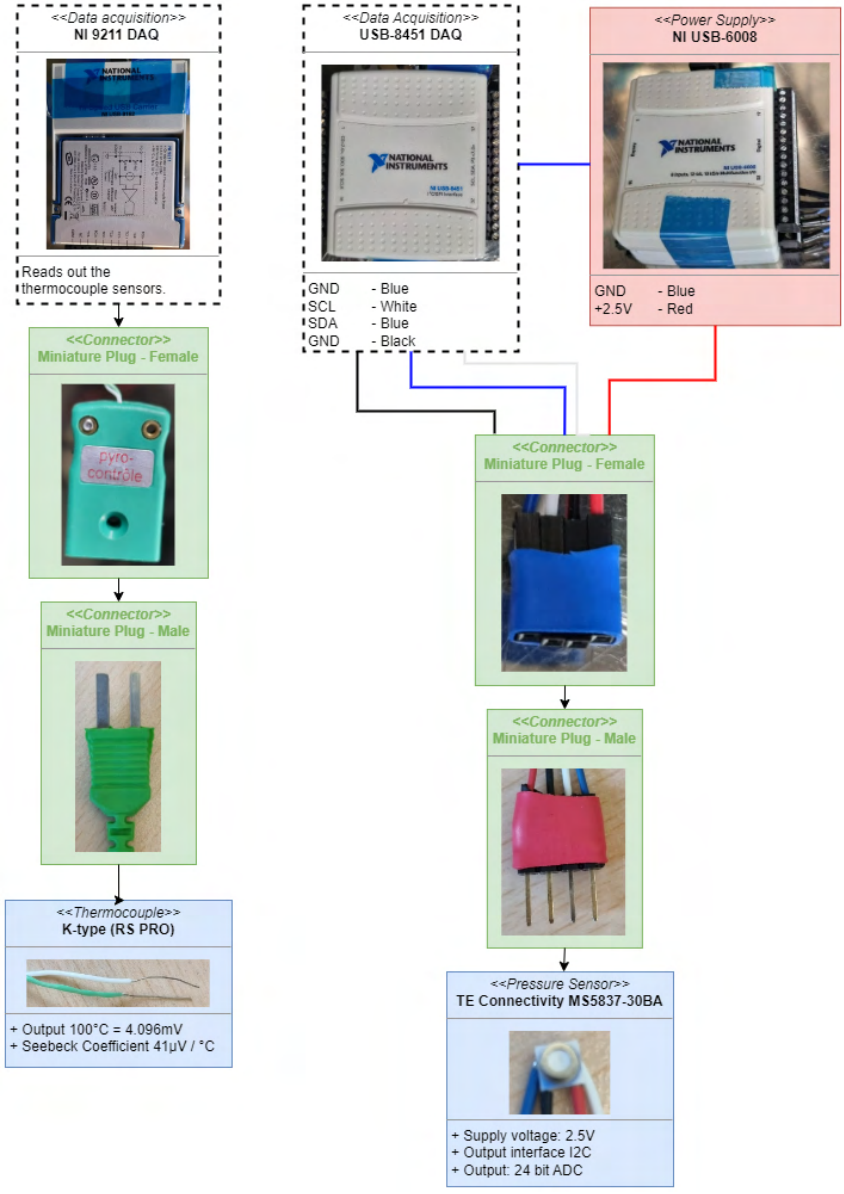

Figure 5.2: Electrical connections to the pressure sensor and thermocouples.

Once the hardware was complete and connected, unit tests could be conducted. LabVIEW code was retrieved from the clean room PC and split up into unit tests to check the sensors one by one. The pressure sensor and thermocouple are connected directly via USB and do not have a separate power supply, this was the easiest point to get started as there are less steps to debug. To get LabVIEW to recognise the USB port in LabVIEW it was found to be necessary to repress the input button and occasionally pull out the USB and plug it back in. This was a good first debugging step. Once the DAQ device is recognised by the computer, it will show a pop-up with information on which device tag the PC has given the DAQ. For the thermocouples, one should realise that the input signal comes from two ports on the DAQ, thus TC0+ and TC0- etc correspond to one channel.

Furthermore, it was discovered that the sensor experienced intermittent signal loss. Typically, the signal could be restored by adjusting the position of the sensor and its wiring, followed by a restart of the software. This solution was deemed insufficient, as reliable data acquisition has to be present in testing situations. Assistance was requested from a fellow master's thesis student with expertise in electronics, Maurits van Heijningen. He brought an oscilloscope to inspect the pressure sensor signal in real time. It became apparent that the signal did not look healthy. Instead of the expected square wave, it resembled a triangular waveform. This posed a risk, as a single missed bit of data could break the connection, rendering LabVIEW unable to retrieve information. The cause of this issue was suspected to be the 1 kΩ resistors. While generally suitable for I^2C connections, the lengthy cables used in this set-up make it an issue. I^2C should be used over as short a distance as possible up to maximum one meter. To ensure sufficient signal transmission, the decision was made to either reduce the resistor size or decrease the data rate. As the aim is a steady-state measurement, it was decided to decrease the clock rate in LabVIEW from 250 Hz to 100Hz. This means the sensor is asked less frequently to send data, and therefore the threshold is reached more frequently and the signal looks healthier. This was an easy software solution as opposed to having to change the hardware. Furthermore one should be aware that the wires are soldered directly on top of the sensor and they can short when they come into contact with metal.

5.1.3. Brooks Mass flow meter

The Brooks 5850S mass flow meter in use is rated for a mass flow of 0 - 2 ln/min of nitrogen, or 0 - 41.69 mg/s. It is connected with a D sub-15 cable via a breakout board, to a CB-68LP board. By changing it to ai17, the voltage output is around zero and so is the mass flow, this is as expected.

5.1.4. Heaters

Two cartridge heaters are placed inside the vacuum oven, they come connected to two banana clips. From old pictures it is derived that they connect to connection 1-2 and 3-4 on the power supply splitter. The heater type is 1/8-Inch FIREROD® from Watlow, with a capacity of 760°C. For testing purposes, the temperatures won't exceed 400°C due to the concern about the heat conduction discussed in chapter 4. This precaution is taken to prevent overheating and consequent heater damage. The datasheet can be found in section B.1.

Five heaters were present in the project box, and it was unclear whether they all worked as during previous theses it was reported that heaters had broken. The author was taught a way to test this by a fellow student. With a multimeter the resistance over a wire can be measured, this is done by sending a small current through the wire and the drop in voltage is measured. If no, or no consistent, signal is measured it means that the connection is broken. In this way one can also discover which pins in a connector on both sides of a wire are connected if the schematics are unavailable.

The power supply splitter inside the chamber is directly connected to the one outside, here connections to the different power supplies are made, the ES 030-10 and SM 7020 are responsible for the heaters. Via a D-sub 15 port on the back of these devices a connection is made to the CB-68LP boards and the PC. The LabVIEW controls these supplies based on the feedback it receives from the thermocouples. It is important to turn the power supplies to maximum voltage and ampere so they are not limited by these settings, while respecting the maximum power outage of these supplies. Based on the old LabVIEW, it was deduced which analogue input corresponded to which power supply and the

heaters were gotten to work.

A Proportional-Integral-Derivative (PID) controller has been designed by Hutten ([11], section 3.5.2) and was recovered from the clean room computer. This controller should be activated after manually bringing the temperature close to the setpoint by either voltage or power control. A mistake was made during programming which gave the PID the wrong thermocouple data, and the PID started to heat the thruster uncontrollably. Even after quitting the program, the thruster continued to heat. This was remedied by turning off the heater power supplies. This issue is likely created through a fault somewhere in the stop button logic incorporated in the while loop of each element. One should be very careful while working with heaters and monitor the temperature while debugging to prevent this from happening.

5.1.5. Variable-Turn Density Coil

The Variable-Turn Density Coil will be used to calibrate the thruster before and after use. It has been designed by Bijster [23] and has been used by Versteeg, Hutten, Pappadimitriou and Takken in the past. This means that plenty of data and LabVIEW code exist for it. The coil is connected via ports 6 and 7 on the power splitter, and connects to the computer in the same way that the heaters do, via a D-sub 15 connection to the CB-68LP. With relative ease the LabVIEW was recovered from the clean room computer.

5.1.6. Load cell

Takken described in his thesis how the Futek LRF400 with a range of 10 grams or 100 mN was used. From the collection of load cells available this was the most suitable choice to measure a thrust of up to 15 mN. An amplifier is added such that a DAQ 6008 can read out the signal, the signal from the load cell is 1 mV/V the amplifier increases this to 10 V. The supplies for this circuit are borrowed from the meetshop[2]. This is a facility in 3ME, it is located in a side room of the IWS and an appointment has to be made beforehand. In addition to picking up the Scaime CJP amplifier and the DAQ 6008 device, a D-sub 9 adapter had to be soldered with four wires to connect to the amplifier, and a few D-sub 9 connectors were used to make the circuit complete.

Jacques Brenkman from the Meetshop explained that the best results could be obtained by calibrating the amplifier to the range that the load cell will be used, in this case a range of 0 to 20 mN was picked, corresponding to 0 - 10 V. In practise the smallest load for which the amplifier could be calibrated was 50 mN. Software to read out the load cell was provided by the Meetshop as well, no software was found from Takken on the load cell hence the provided software was adapted to fit the program. The Scaime CJP has an internal low-pass filter with a 10Hz cutting frequency. A filter of this type allows signals with frequencies below 10 Hz to pass through the filter unaffected, signals with a frequency below 0.1 s get blocked. As steady-state thrust is desired, signals with a high-frequency are not of interest. Therefore the filter is turned on to eliminate problems caused by vibrations and electrical noise. With a filter, the sampling frequency must be at least double the filtering frequency according to the Nyquist-Shannon sampling theorem. The load cell is sampled at 30Hz, well above this threshold.

The Meetshop software provided a simple voltage-to-thrust relation, the offset and slope are filled in manually after calibration. The offset of the load cell is recorded before each experiment, and it can be easily corrected for afterwards. The author adapted the code to show the force exerted on the load cell by the Variable-Turn Density Coil (VTDC), this was done with the respective arm length from the centre to the coil and load cell.

5.1.7. Feedsystem

The valve that is used in this system is a VHS Series solenoid valve from the Lee company of type INKX0514300A. This is a high-speed, normally closed 2-way valve. It is operated with a spike (24 V) and hold (3.2 V) voltage administrated through the control valve module was purchased together with the valve. The valve is controlled with LabVIEW via an Arduino and USB connection to the PC [24]. The Arduino board is necessary to generate the Pulse-width modulation voltage signal and has been purchased from RedBear, specifically it is a Blend Micro board ([24], sec 3.2). Furthermore the control

[2]Meetshop-3ME@tudelft.nl

drive module is connected to power supplies D-030-10 for hold voltage and E-030-10 for spike voltage. The electric connection to the valve is made via two pins protruding from the valve onto which two female Dupont connectors slide. It is noteworthy that four dupont connectors come from the D-sub 9 inside the vacuum chamber, pin 6 and 7 correspond to the valve. The red wire should be positioned on the right pin, when the pins point towards the observer and the flow direction is directed upwards. These items have been set up by previous students.

With feedsystem components found within the boxes of the clean room workshop a small feedsystem was assembled. Inside of the vacuum oven are the connections for a quick disconnect, this two component fitting can simply be assembled by pressing one onto the other till a click is heard. The male part of the quick disconnect is on the left of Figure 5.3, followed by a 1/4” swagelock tube, and a male swagelock to NPT fitting. The NPT fitting is made leak tight by applying plenty of Teflon tape. The tape has to be applied in the same direction as the thread, to avoid unravelling when screwing into the female connection. This is followed by a brass fitting, also covered in Teflon tape and finished with a Lee company connection. From here a long Teflon tube with an outer diameter of 0.062 inch (1.57 mm) with a male 0.138-40 UNF threaded fitting on both ends [25] connects to the valve. Another 0.138-40 UNF threaded fitting exits the valve and connects to the Teflon tube that is glued into the test bench stand.

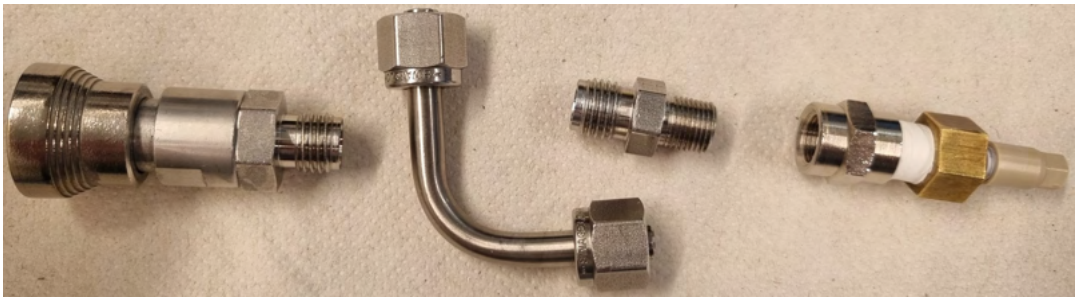

Figure 5.3: Components of the feedsystem inside the vacuum oven

The feedsystem outside of the vacuum chamber consists of a quick disconnect as exit of the vacuum oven that is connected via a tube to the mass flow meter on the top right of the feedsystem board shown in Figure 5.4. This board is designed, such that three different mass flow meters can be mounted at the same time. Currently only one branch is in use. It is placed on top of a four-wheeled plank with the nitrogen bottle strapped to the back of the board. There is a compressed gas regulator at the bottom of the board that reduces the gas pressure from the bottle (0-200 bar) to 0-15 bar. This creates a relatively safe system to work with as no high pressures can come out of lines. One should be mindful that during experiments the black line between the bottle and regulator contains high pressure and is therefore dangerous. Valves with a handle are turned perpendicular to the flow direction to close them. Valves with a nob are turned clockwise to close them.

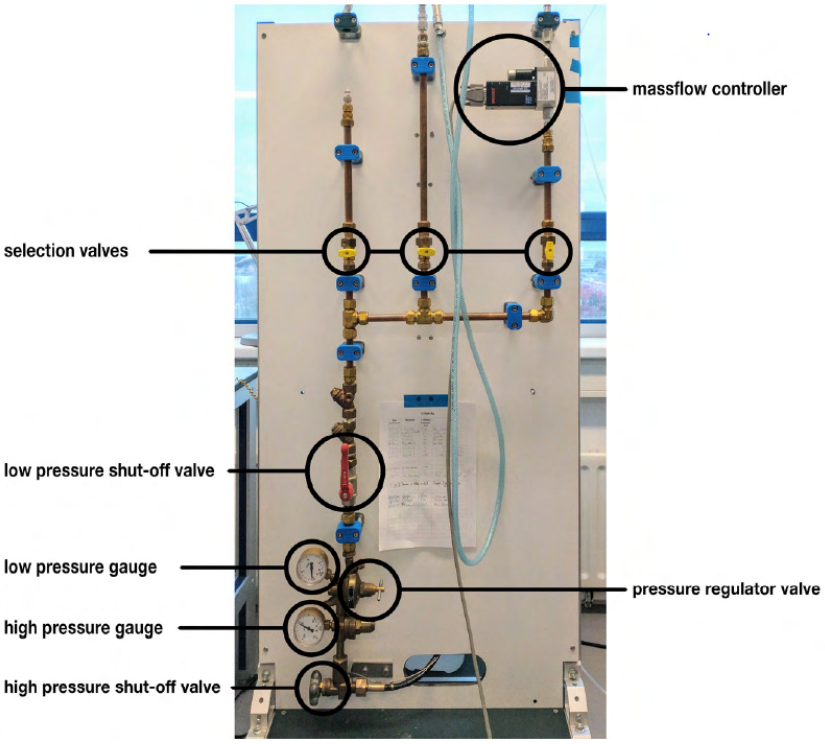

Figure 5.4: Feedsystem board including description ([11], sec 3.3)

5.1.8. Test bench

The test bench used during this experiment is the TB-50m. It was found mostly assembled in the clean room, one additional element was required to make it work. A connection had to be made between the load cell and test bench. The holes on the side of the torsion beam are M3, the load cell connection was a 10 - 32 UNF 2B. This type of bolt was not present at the faculty. A M5 fits a thread length inside the load cell connection and as a temporary solution, the head of an M5 bolt was drilled out and an M3 nut was glued in with metal glue. This brings an uncertainty of misalignment of load introduction into the load cell as the longitudinal axis of the M5 bolt and the M3 nut do not necessarily coincide.

The assembled test bench including thrusters and sensors is displayed in Figure 5.5. This image is annotated with the items present inside the vacuum chamber.

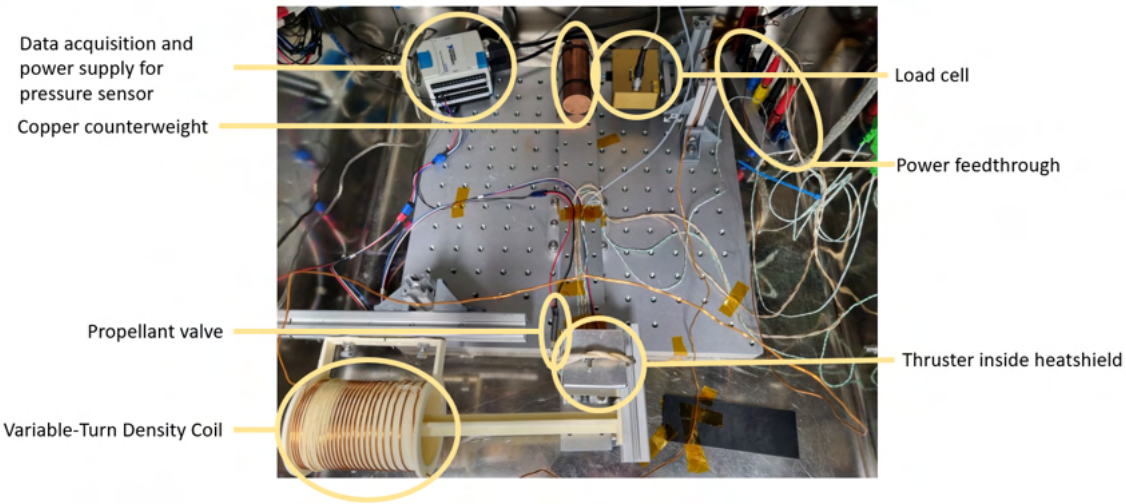

Figure 5.5: Assembled test bench with annotations

5.2. Confidence bounds

In this section, the focus is on the individual accuracy of equipment and the combined effect it has on the setup. The confidence bounds determined here dictate that 99.7% of the values measured will fall within the provided range. This range, $\bar{x} \pm 3\sigma$, is determined by the computed mean value ($\bar{x}$) and the standard deviation (σ). The values have previously been recorded by Hutten and Versteeg for the mass flow meter and pressure sensor, the thrust measurement equipment has been discussed by Takken. In this thesis those two elements are combined.

The following sensor and actuator standard deviations are discussed in detail by Versteeg [8] in sections 6.2.2 - 6.2.3 and 8.2.1 and by Hutten [11] in section 3.6: Parameter confidence bounds. Therefore only a summary of their effects is given in Table 5.2 here. The effect of both the sensor itself and the data transfer to the PC is taken into account. These connections have not been altered since the previous two theses so their assessment of the inaccuracy measurements is taken as correct.

- K type thermocouple measured with the NI 9211 DAQ (T_c)
- TE Connectivity MS5837-30BA thrust chamber pressure sensor (p_c & T_{ps})
- VACUUBRAND vsp 3000 Vacuum oven pressure sensor (p_a)
- Brooks 5850S nitrogen mass flow meter ($\dot{m}$)
- ES 030-10 & SM-7020, power supply of the heaters
- Delta Elektronika SM 7020-D, power supply of the actuator coil

Parameter	3 standard deviations (3σ)
T_c	6 - 7.5 °K
p_c	$\pm$ 50 mbar between 0 to 45°C $\pm$ 100 mbar between -20 to 85°C
p_a	N_2: 15% H_2O: 50%
$\dot{m}$	N_2: max(0.7%, 0.08 mg/s)
P_{heat}	0.2%

Table 5.2: Summary of standard deviations

Noteworthy is that the accuracy of the thrust chamber pressure sensor is dependent on the internal temperature, this should be recorded each test. For the Brooks mass flow meter, the device requires 45 minutes to completely warm up and stabilise. Hutten has recorded the effects of water on the vacuum oven pressure sensor and the syringe pump. The programming accuracy of the heater power supplies at constant voltage is equal to the uncertainty of the heating power.

The measurement inaccuracy found for the thermocouple is elaborated upon as this includes several factors. The determination of the temperature uncertainty consists of three elements. The uncertainty of the sensor itself is equal to 2.2K or 0.75%, whichever is greater. From 20°C onwards the 0.75% is leading. In addition to that the DAQ device adds an uncertainty of 2.5°C and temperature variations along the thruster body are accounted for by 5°C. As these errors are independent, the total temperature uncertainty can be computed with Equation 5.1 [21]. This leads to an uncertainty of 6-7.5°K in chamber temperature over a range of 293-673°K. The maximum error at room temperature is 2%.

$$3\sigma_{T_c} = \sqrt{(0.75\% \cdot T_c)^2 + 2.5^2 + 5^2} \tag{5.1}$$

There are also a couple of altered or new elements in the system. The load cell is newly introduced. In the datasheet of the Futek LSP400 in section B.1 several potential errors are found. The combined error is the root mean square value of nonlinearity, hysteresis, non-repeatability and temperature effect according to the FUTEK Glossary. The occurrence of these errors is unrelated. The conditions are full applied load, assuming a temperature range of $\pm$ 2°C and proper set-up and calibration. Creep

and potential read-out errors are not included. Creep will have to be detected by calibrating before and after testing to detect the drift. The Rated Output (R.O.) of the sensor is 0.1 N or 100 mN. Using Equation 5.2 all relevant uncertainties from Table 5.3 are added, resulting in a load cell of 0.17 mN.

Non Linearity [% of R.O.]	0.1
Hysteresis [% of R.O.]	0.1
Nonrepeatability [% of R.O.]	0.1
Creep [% of R.O.]	0.2
Temp Shift Zero. [% of R.O./°C]	0.01
Temp Shift Span. [% of Load/°F]	0.01

Table 5.3: Uncertainties relevant for the LRF 400 load cell

$$3\sigma_{F_t} = \sqrt{x_1^2 + x_2^2 + ... + x_n^2} = 0.17\% \text{ of R.O i.e. } 0.17 \text{ mN.} \tag{5.2}$$

The accuracy of the calibration spool was determined in subsection 6.3.2.

6

Preliminary tests

A set of preliminary tests are executed to ensure that the data collected during the nitrogen testing has meaning. If tests are performed without properly knowing the geometry of the thruster or the leak rate, no meaningful conclusions can be drawn as the parameters are unknown.
The following preliminary tests will be executed:

- Optical characterisation.
- Leak testing with nitrogen.
- Calibration of the test bench

6.1. Optical characterisation

Optical characterisation of the components is performed before disassembly and after re-assembly. The data from before can be used to get a feeling of the degradation of the nozzle over time. It is also a point of reference for what the nozzle exit is expected to return to, and the upper limit of the surface roughness that should be achieved. Two types of measurements are performed: Surface roughness analysis of the copper sealing surface and measurements of the nozzle exit.

The surface roughness is relevant as in micro-nozzles viscous boundary layer effects and wall losses are no longer negligible, each can account for up to 10% efficiency loss [26]. This means that the surface roughness should be considerably less than the throat dimensions, i.e. a wave amplitude below 4%, to prevent the performance from being negatively affected. This would lead to a surface roughness of a maximum of 5 μm with a throat width of 130 μm. If less is obtainable with the equipment available, this is desirable. The nozzle geometry should be known to compute the expected thruster behaviour as explained in chapter 3.

6.1.1. Surface roughness

This task proved more difficult than expected. It was found that the numerical aperture and optical resolution change with the magnification lens, and therefore the surface features that can be distinguished are altered. This means that per magnification a different surface roughness is detected. This was discussed with Pietro Marchese, who is in charge of the microscopes. He confirmed that there was not one 'best' setting to measure surface roughness. Instead he suggested the usage of a reference material with known roughness for comparison. The other option would be to use the specific settings indicated in guidelines for my research. As this is a continuation of master theses projects, these guidelines sadly do not exist. No explanation could be found in the thesis by Versteeg [8] to defend his choice for 40x on the Keyence VR-5000. Keyence has been contacted for reference material samples, but no reply has been received.

To proceed without this information all types of data has been collected with different light settings and magnitudes. A poster by Keyence was consulted to obtain the correct sampling length for the specimen. The sampling length is estimated based on the expected Ra value, the sampling length

is chosen and then cross-checked with the resulting Ra for correctness. Where Ra is a measure of surface roughness defined as the average difference between maxima and minima. The sampling length is the longest spatial wavelength that will be measured, this is determined by the particular roughness requirement. In the end the blocks were deemed acceptable when the Ra value was below 10 μm at 5x magnification as this was the maximal achievable value with the tools available.

6.1.2. Nozzle geometry

The nozzle exit was measured before disassembly and after assembly. The before measurement provides an indication of the degradation of the thruster production in 2019. A new thrust profile was used by Hutten in 2020, but no work was done on the copper blocks. The Keyence VK-X1000 Confocal laser microscope was used to perform the measurements. This microscope combines laser and optical techniques to reconstruct one image with the best quality images. The set-up under the microscope is shown in Figure 6.1, the vantage point is from the top looking into the nozzle exit.

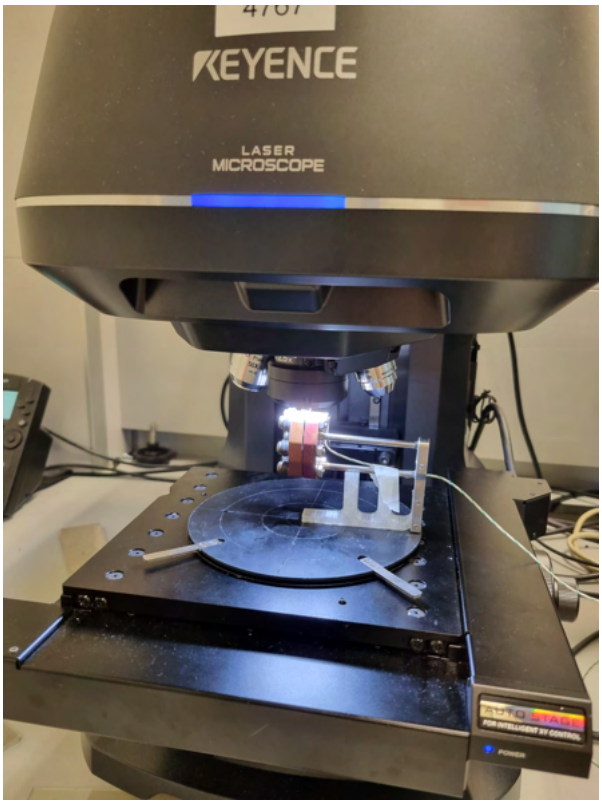

Figure 6.1: Thruster underneath microscope with 3D printed stand

A significant difference can be seen between the nozzle exit after assembly by Hutten [11] shown in Figure 6.2 and its present state, Figure 6.3. A different microscope and magnification lens was used to record both images, hence the scale is not equal. Whereas after assembly by Hutten the nozzle appears to consist of sharp straight lines, the left copper block shows degradation of the surface quality. This could be attributed to copper oxidation over time. Discrepancies in the exit area were also found when measurement data was examined from Versteeg after assembly and Hutten before he disassembled the thruster. This indicates that changes in area occur either during the experiments or subsequently over time.

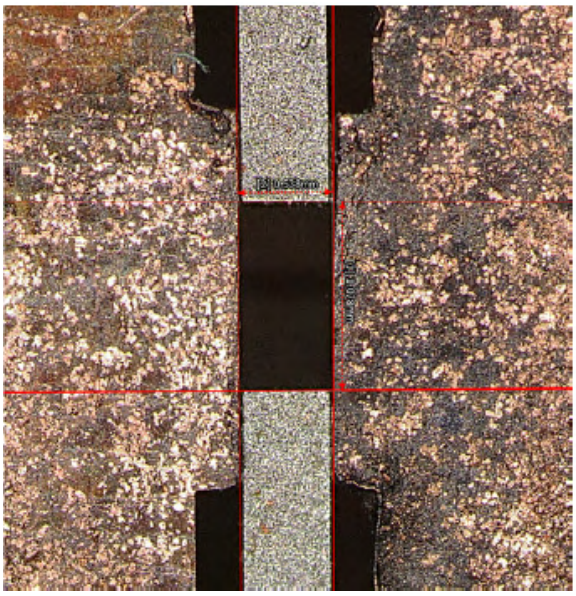

Figure 6.2: Nozzle exit after assembly by Hutten [11]

Figure 6.3: Nozzle exit before disassembly under the VK-X1000 microscope

Due to the way that the thruster is constructed, the throat area can not be measured. There is no light source that can penetrate into the nozzle to visualise the throat area. The nozzle height (H), is equal to the thickness of the profile and is originally assumed to be constant in the throat and exit. By measuring the unconstrained thrust profile the throat area can be derived. As the thruster profile is squeezed between the sealing surfaces, it cannot be assumed that the dimensions are equal to the unconstrained profile. However, it can be assumed that no rotation takes place, thus the difference between the constraint and unconstrained profile is equal in the throat and the exit. This allows the computation of the throat width (W_t) and the throat area (A_t). In Table 6.1 the nozzle geometry of Figure 6.4 is presented. The way these values were determined will be explained in the following paragraphs.

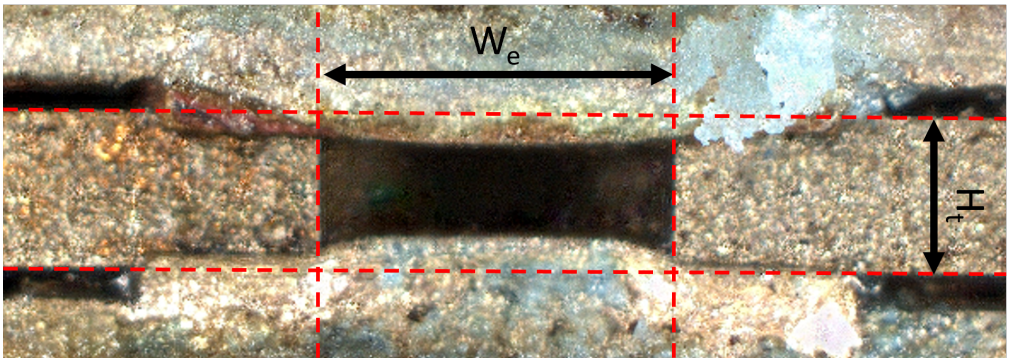

Figure 6.4: Nozzle exit after assembly and tightening

After assembly the threaded blocks obscured the exit, there is only a 2 mm gap between them. This made focusing more difficult as the edge of the picture quickly fell out of focus, as can be seen in Figure 6.4. Ring light at 50% and 5x magnification was found to achieve reasonable results. For the width 1138 $\mu m \pm 5$ μm was found. The accuracy with which this edge could be determined was set to be two pixels. For the width determination, the unconstrained thruster profile values were taken from Hutten [11] as the same thruster cut out was used, W_e = 1073 $\mu m \pm 5$, W_t = 135 $\mu m \pm 5$. The difference between throat and exit width remains constant as no rotation takes place, therefore the throat width becomes 200.1 $\mu m \pm 16.2$. The force necessary to make the thruster leak tight has forced material into the nozzle. This creates a curved edge, hence it was not possible to simply determine the width of the exit area. Instead of taking the product of width and height, the exit area was determined by tracing

the circumference. Due to the uncertainty that came with manually selecting the edges, the uncertainty was increased to 4 pixels or 10.8 μm. The average exit height (H_e) is based on the exit area and (W_e), but it should be clear that the exit is no longer rectangular. Looking at the edges of the copper block (top and bottom) and the steel profile (left and right) the copper appears to not only protrude into the nozzle but also in front of it to create a reduction in exit height. It is assumed that the copper moved in front of the steel, as this is more likely than copper deforming the steel. Images taken with the microscope with indicated dimensions are shown in section D.2.

Parameter	This Work	Hutten	Versteeg	Design
H_t [μm]	522 $\pm$ 34.3	538 $\pm$ 8	496 $\pm$ 4	500
W_t [μm]	200.1 $\pm$ 16.2	140 $\pm$ 11	142.3 $\pm$ 9.6	130
A_t [10^3 μm^2]	104.5 $\pm$ 15.3	75.3 $\pm$ 7	70.6 $\pm$ 5.3	65
H_e [μm]	315.6 $\pm$ 10.8	538 $\pm$ 8	496 $\pm$ 4	500
W_e [μm]	1138.1 $\pm$ 5.4	1078 $\pm$ 8	1071.9 $\pm$ 5.6	1072.5
A_e [10^3 μm^2]	359 $\pm$ 14.0	580 $\pm$ 12.9	531 $\pm$ 7.1	536
A_e/A_t (ϵ) [-]	3.44 $\pm$ 0.64	7.70 $\pm$ 0.89	7.53 $\pm$ 0.67	8.25

Table 6.1: Computed nozzle geometry based on microscope measurements including uncertainty in μm

As deflection is present in the exit, Equation 6.1[1] is consulted to relate the amount of deflection in the exit to deflection in the throat in order to compute the throat height. This situation is assessed as a fixed-fixed beam with a distributed load. The distributed load estimation comes from the load being applied through the six bolts present along the thruster. L is taken as the width, w is the applied load, E is the Young modulus of the material and I is the moment of Inertia. It is assumed that the load and moment of Inertia are constant throughout the exit and throat, the Young's modulus is a material property and therefore also constant. This makes the deflection difference between the throat and exit solely dependent on the width, which scales with a factor of 4. As a result, the deflection in the throat is only 0.09% of that in the exit, rendering it negligible. The thickness of the steel profile measured is taken as height in the throat, as indicated in Figure 6.4, uncertainty during this measurement was 5.7μm/pixel and 3 pixels margin was taken on each line placement.

$$\delta_{max} = \frac{wL^4}{384EI} \tag{6.1}$$

Uncertainties were computed using simple averaging errors [27]. For addition and subtraction of uncertainties $\Delta z = \Delta x + \Delta y$ is used, for multiplication or division $\Delta z = (\frac{\Delta x}{x} + \frac{\Delta y}{y}) \cdot z$. Here Δz is the new uncertainty and x, y, and z represent the values of the respective parameters. As it was unclear what method the predecessors selected to arrive at the uncertainty margins presented in their reports, it was decided to redo their uncertainty computations to allow for comparison.

This new nozzle geometry described in Table 6.1 is based on the assumption that the difference between constrained and unconstrained throat and exit width remains constant. The hypothesis is that material protuding into the nozzle exit has spread the thruster profile with 65.6 μm with respect to the design value. As can be seen in Figure 6.5 the thruster profile is open-ended and kept in place through the bolts surrounding it. A small spread of the nozzle is imaginable in such a set-up as regular tolerance bolts were used instead of shoulder bolts. These were originally included in the design and give a tighter tolerance but did not fit into the final construction. This assumption combined with the way that the deflection is predicted to behave in the throat leads to a decrease in exit area and an increase in throat area, thereby lowering the expansion ratio significantly to 41.2% of the design value.

It should be mentioned that the thruster profile might have been deformed differently. This option is not considered in this research but it is a possibility that a different pivot point was present on the thruster profile that left the throat area intact and only widened the nozzle exit.

[1] https://mechanicalc.com/reference/beam-analysis

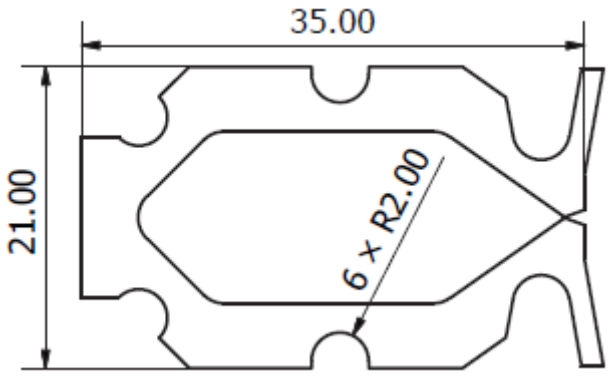

Figure 6.5: Drawing of the thruster profile

6.1.3. Thruster profile cut-out

During leak testing severe leakage was found. To rule out that this was caused by the deformation of the thruster profile which has been used previously by Hutten, it was put under the microscope to find any marks left by clamping. The profile is made from stainless steel, a relatively ductile metal. If it is deformed, this could cause leakage. Each time the thruster is taken apart the sealing surface degrades as it plastically deforms to fill gaps in material, therefore it was undesirable to take it apart. Versteeg and Hutten have used different profiles, hence there was one profile not inside of the thruster that could be used to test this hypothesis. This profile is shown in Figure 6.6, it is evident where the clamping took place due to discolouration.

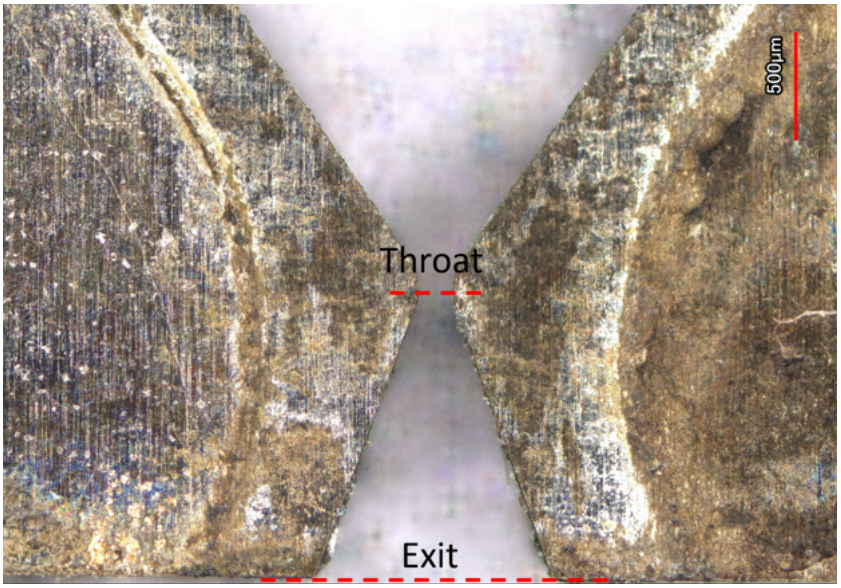

Figure 6.6: Old unconstrained thruster profile

Both with the roughness and plane measurement tool no major steps were found in the profile. One would expect small dents or extrusions in the material where it would have shaped around the copper. As these were not detected, it was ruled out that the thruster profile caused the leakage increase.

6.2. Leak testing

Leak testing is performed before experimental testing to find out how much of the mass flow going into the thruster is actually being converted into measurable thrust and how much is leaking away. During the assembly of the thruster, connections have also been undone, and it has to be verified whether

these connections have been properly reassembled. In this section the leak rate will be quantified, e.g. it will be quantified how much propellant actually exits the nozzle in normal conditions. This mass flow is used in the analytical model to verify the thrust measurements and is therefore important to be correct.

Methodology and Set-up

The same method is employed as Versteeg [8] and Hutten [11] have used. With a glue clamp a piece of rubber is secured over the nozzle and the back of the thruster as shown in Figure 6.8. It is important that not too much force is used to secure the glue clamp as otherwise the copper blocks will be forced away from the thrust profile and this will reduce the sealing capacity. Procedures were taken from appendix C.1 from Versteeg and can be found back in section C.1, they were adjusted where necessary.

The rubber required for the experiment was found in the project box and the glue clamps were located in one of the tool cabinets in the clean room. Due to the addition of the threaded blocks, the rubber has to be cut such that it fits in between, this is a space of around two millimetres. The rubber had to be cut such that it protruded a couple of millimetres to be able to push it in with the glue clamp. To make sure that the clamp is not over-tightened, the clamp is tightened with the valve open. The escaping nitrogen can be heard and therefore it can be determined when the clamp is tightened sufficiently.

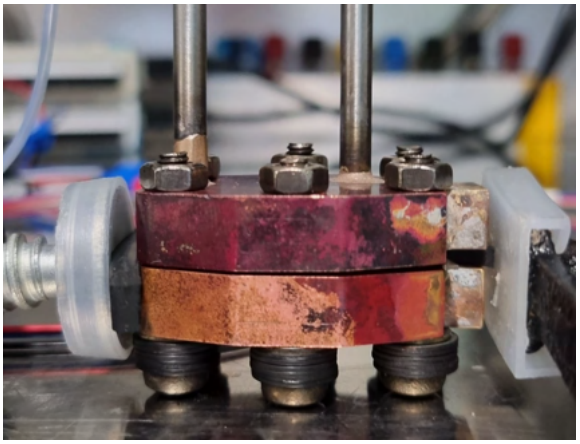

(a) Pieces of rubber clamped on the thruster

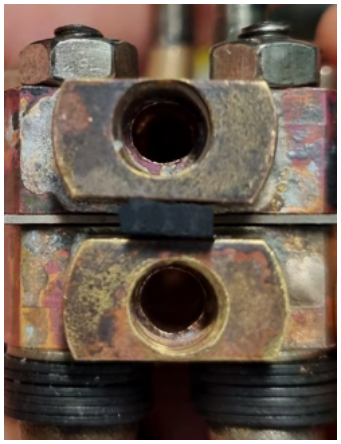

Figure 6.7: Blocked nozzle view

Figure 6.8: Leak testing set-up

The leak rate is determined by measuring the pressure drop within the closed system. The thruster is filled with nitrogen gas under ambient conditions until the pressure sensor reaches a steady state, once a constant pressure reading is obtained the propellant valve is closed. The leak test will be conducted at a pressure above 2 bar, this is slightly above the chamber pressure expected during the experiments where the highest planned value is 1.5 bar. The pressure drop within this closed system is indicative of nitrogen leaking out, this will be recorded over time. This pressure drop can be related to the mass leaking from the thruster via Equation 6.2. This equation is derived from the ideal gas law, under the assumption that there is a constant gas temperature (T_c) and internal volume (V_c). As the thruster is rigid and is held within the stable conditions of the clean room, this is justifiable. In Equation 6.2 the following standards are maintained. M stands for the molar mass of nitrogen of 28.014 g/mol and R for the universal gas constant of 8.314 J/(mol K). The volume within the thruster has been computed by Versteeg, this includes the top and bottom block, nozzle profile layer, one tube filled with 95% porous foam and one without and finally the MINSTAC tube to the solenoid valve. These two latter items have been modified by the author during the reassemble. The distance to the valve has been shortened to 4.45 cm, with an inner diameter of 0.04 inch this leads to a volume of 14.20 cm^3. This does include the parts within the aluminium and going into the valve. With these changes, the total internal volume of the thruster becomes 2.422 cm^3.

$$\dot{m}_{leak} = \dot{p}_c \frac{V_c M}{R T_c} \tag{6.2}$$

Due to the degraded sealing edge found during polishing subsection 4.3.3, the leakage is expected to be significant during initial leak tests. First, a short test will be conducted to see how the thruster performs and whether additional tightening of the bolts is required. A check was conducted to establish the maximum torque allowance of the bolts. It was unknown what type of strength the used bolts have, they are the standard stainless steel torx-head M4 bolts available in the workshop. Using the minimum tensile strength found on the engineering toolbox[2] and $T = F \cdot r$ it was computed that each bolt can take at least 7 Nm. After tightening, three longer tests will be performed until the pressure sensor reaches ambient, or till one hour has passed. Three tests should be sufficient data to filter out any faulty data. Gas leak detection spray will be used to detect any leaks along the circumference, and after testing special care is taken to dry off the thruster to avoid corrosion and soap residue.

Results and Discussion

During the first leak test, the thruster emptied rapidly after closing the supply valve. With gas leak detection spray it was found that leaks occurred around the exit of the thruster. To ensure that this was a leak, and not merely due to the way that the nozzle is blocked, the clamp was tightened slightly in between tests until the leak rate no longer decreased. In theory, this should mean that the nozzle is blocked and the leak is elsewhere. The set-up is shown in Figure 6.8. The bolts were tightened to 2.5 Nm with the torque wrench (FACOM A.402 0.5-2.5 Nm) in an attempt to lessen the leakage rate. The leakage rate was determined at 1 bar above the ambient conditions. This corresponds to a leaked mass flow rate of 0.96-1.23 mg/s or 5.5-7.02% of the full mass flow rate. The full mass flow rate is based on nitrogen testing at 20°C in ambient conditions to obtain 1 bar chamber pressure by Hutten ([11], sec.4.1). It was decided to continue the approach of tightening further with a torque wrench provided by Joris Melkert. Other options would have been to find a different sealing method, or let the sealing edge be re-machined by DEMO. This would have been a time consuming endeavour, and continuing to tighten as much as possible till the bolt threads would shear off was worth pursuing. After tightening to 2.8 Nm the leak rate dropped to almost 1%, further tightening to 3.0 Nm did not improve this rate by much.

The final achieved pressure leak rate is shown in Figure 6.9. Three different leakage percentages are shown in the legend, the lines are overlapping. Tests were also performed at 2.6 and 3.0 bar to check how the thruster would respond to pressure variations, the leakage rate remains between 1.2% and 1.3% at 1 bar throughout these tests.

[2] https://www.engineeringtoolbox.com/metric-bolts-minimum-ultimate-tensile-proof-loads-d_2026.html

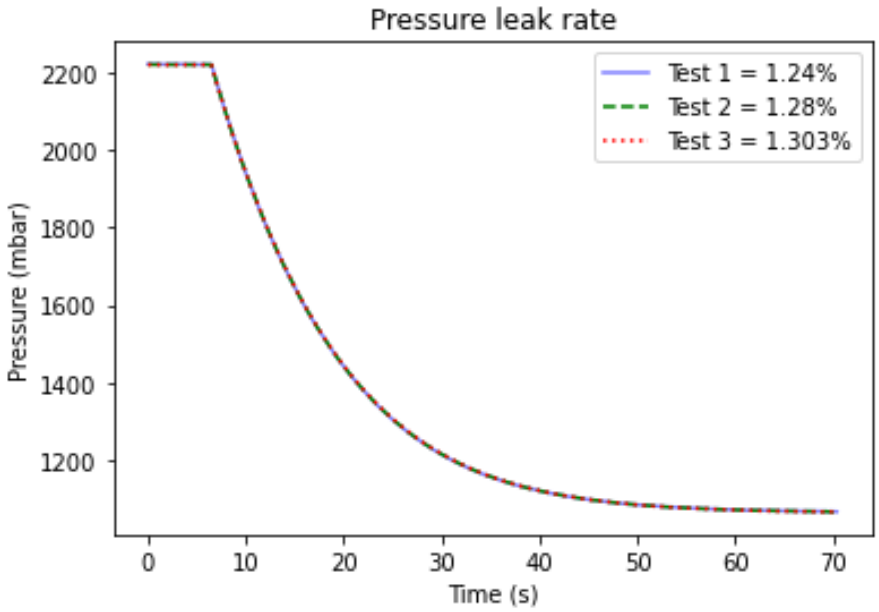

Figure 6.9: Pressure drop due to propellant leakage at 2.2 bar maximum

A leakage rate of 5% was set to be the maximum allowable leak rate by Hutten, as errors higher than that will significantly impact the performance as this exceeds the inaccuracy of the analytical model. Versteeg set the threshold for acceptable leakage rate at 1%, as this is equal in magnitude to the thrust sensor and mass flow accuracy. The obtained leakage rate is below the sensor uncertainty and satisfies the requirements.

Recommendations

For future testing with this thruster, it is advised to not take it apart as currently a seal is achieved by crushing the copper into the steel profile, and not with a proper sealing edge. This is clearly visible at the back of the thruster where the copper blocks are touching in the corners. Thus once the thruster is taken apart it loses its sealing capability.

To remedy this situation, the sealing edge can be restored by re-machining the sealing edge. This can be accomplished by taking off 0.2mm from the top surface. The process of polishing and microscopic analysis will have to be repeated. However, it has been shown that this sealing edge is not reusable, as after two re-assemblies it has lost its integrity. This means that a different approach to thruster design might be necessary, such as a redesign of the sealing method.

It would have been advisable to check the nozzle exit with a microscope between rounds of tightening, as due to this severe tightening copper now protrudes into the nozzle exit as is discussed in section 6.1.

6.3. Calibration

Calibration is a very secure process to minimise any measurement accuracy present, with it done correctly anomalies recorded during the experiments are more easily to define [21].

6.3.1. Load cell

The calibration process will begin with the re-calibration the LRF400 load cell using known weights. The load cell has last been used by Takken [14] in 2021 when he rebuild the TB-50m, and no record has been found of anybody using the test bench in the meantime. Any significant impact on the load cell might have shifted the linear relationship between load and output voltage. Therefore it is wise to establish a new weight-voltage output relation.

As a first step of the calibration the Scaime CJP is connected to the load cell and voltage is recorded via a voltage meter. This set-up is displayed in Figure 6.10. In this way the expected behaviour of the load cell is known, which makes setting up the LabView possible as a next step. First the amplifier is set up to equate 50 g to 10 V and measure 0 V when no load is applied, this is an iterative process of adjusting screws and pins on the amplifier. As the load cell is of the type tension-compression load cell, it was found hard to keep 0 V equal to zero load as the load cell drifted slightly. However, the 50 g to 10 V was a steady measurement. This adjustment was done to increase the resolution of the load cell. Its range is 0 - 100 mN, but if you modify the amplifier such that it only records the used range, the signal is refined.

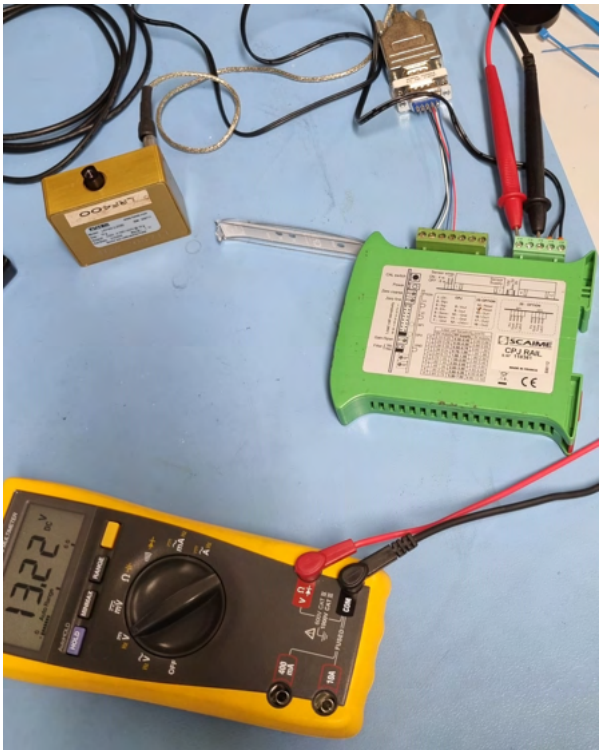

Figure 6.10: Load cell calibration set-up

There is a box of weights present inside the cleanroom, their real weight is recorded with the Mettler Coledo AG electronic scale. A collection of bolts and nuts were also found in the box, these were used to increase the number of data points. This scale has a reported inaccuracy of 0.1 mg, the datasheet is shown in section B.1. It was found unnecessary to calibrate the load cell to below 1% of its capacity as it was recorded to become less accurate in this range and the thruster does not produce thrust in this spectrum. The load cell was taken off the test bench and placed vertically, in the upright position, for this test. Each measurement was recorded upon settling, and then again 30 seconds later to detect drift in the signal. As reported, this was found to be quite minimal. The gravitational constant of 9.80665 m/s^2 was used to move from weight to load. The results of this test can be found in Table 6.2 and the recorded relationship between weight and output voltage is shown in Figure 6.11. It can be seen that this relationship is very linear as the R^2 value is close to 1, this means that the trend line fits the data almost perfectly. The linear regression to relate measured load to voltage is reported in Equation 6.3. One should keep in mind that the orientation of the load cell is different in the test bench than during these measurements, this will change the intercept value. During experiments, this value should be recorded and adjusted in the code.

$$F_{LRF400} = 4.901677 \cdot V_{LRF400} + F_{intercept} \tag{6.3}$$

#	Indicated Mass [g]	Measured mass [g]	Voltage [V]	Voltage [V] (30s)
1	5	5.0018	10.00	10.00
2	2	2.004	3.995	3.998
3	1	1.006	1.997	1.997
4	0.629	0.6293	1.249	1.250
5	0.3872	0.3878	0.77	0.768
6	0.2872	0.2873	0.566	0.565
7	0.2142	0.2158	0.426	0.422
8	0.5	0.5001	0.990	0.989
9	0.2	0.1999	0.392	0.391
10	0.1	0.0997	0.189	0.188

Table 6.2: Load cell input and outputs for the calibration

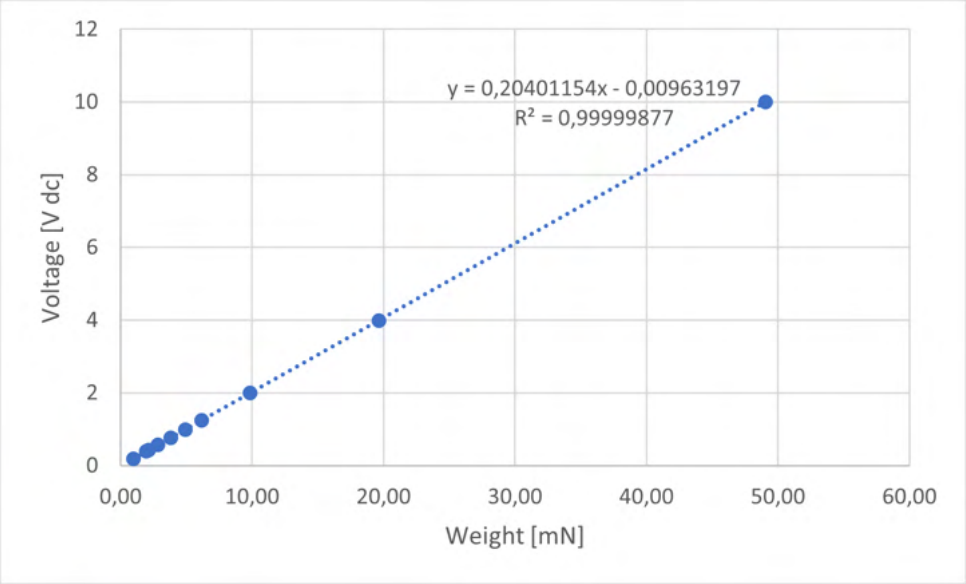

Figure 6.11: Relationship between weight in mN and voltage

6.3.2. Test Bench

Since the test bench has been partially disassembled since its construction by A. Takken [14] in 2020 and new elements were to the construction, a new calibration is necessary. This is done with the Variable-Turn Density Coil (VTDC) constructed by R. Bijster [23]. This actuator consists of a coil with a permanent magnet suspended inside along the coil's centerline. Varying the current applied to the coil alters the position of the magnet inside the created magnetic field. In the past Versteeg and Pappadimitriou have related the current to the force, which turned out to be 0.826 mN A^{-1} with 3σ confidence bounds of ± 0.006 mN A^{-1}, where σ is the standard deviation. This was done with the Mettler Coledi AG electronic scale as depicted in Figure 6.12. After assembly of the TB-50m A. Takken found a gradient of 0.823 mN A^{-1}, a possible explanation given for this difference of 0.31% were human error in measuring the pendulum arms and positioning of the magnet inside the coil. Other options presented were the horizontal pendulum arm not being level or interference of the computer with the coil connections creating variation in the magnetic field strength.

Software to perform this experiment has been created by Versteeg in LabView, which raises the current of the coil from 0 A to 20 A in steps of 0.5 A. The experiment is conducted with a sampling rate of 30 Hz for the load cell and each step takes 60 seconds, collecting 1800 data points per step. It

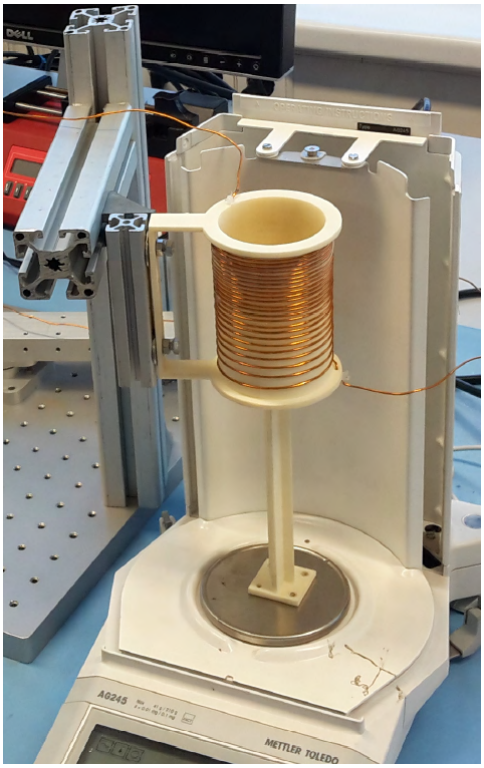

Figure 6.12: Coil calibration as executed by Pappadimitriou [9]

was found by Takken that the coil overheats when kept at 16 A or above for extended periods of time. This means that the test bench was previously calibrated up to 12.3 mN. This is very close to the thrust that the VLM is expected to produce during experiments. This range can be extended by installing a stronger magnet or using more magnets, another option is to elongate the moment arm from the coil to the rotation point. Looking at how the test bench was installed by Takken, elongating the rotation arm can be achieved quite easily. The test bench is constructed on a plate with equally spaced threaded holes, the coil is placed one hole more outwards from the rotational axis.

It was found that each element added to or subtracted from the torsion beam changes its neutral position, this influences the zero weight voltage measurement of the load cell. In other words the offset, or $V_{intercept}$ in Equation 6.3 has to be adapted. One can compute the mean value of 0 A going through the coil and thereby determine the new offset. Each time the elements on the torsion beam are changed, the connection to the load cell should be redone to ensure there is no residual load here that puts the load cell fully in compression or tension. Once the voltage is translated to load with Equation 6.3, the difference in arm length to the centre of the beam needs to be accounted for. This is done with Equation 6.4, where d_1 is the length from the load cell to the centre, and d_2 is from the centre to the arm holding the magnet. These measurements were done by hand and are subjected to human error of several millimetres.

$$F_{coil} = F_{LRF400} \cdot \frac{d_1}{d_2} = F_{LC} \cdot \frac{175}{192} \tag{6.4}$$

Four different calibration goals were identified to isolate the effect of different parameters on the load slope and standard deviation. These goals are listed in Table 6.3. Each test is conducted in a closed vacuum chamber. In the first test, the test bench is bare with only the counterweight attached to level the torsion beam. Next, the thruster and all sensors are added and nitrogen is present up to the propellant valve to mimic accurate wire stiffness during the experiment. Then the vacuum chamber is turned on and finally the effect of turning on the heaters was analysed. Each of these steps brings the test bench closer to the real experiment conditions. With these measurements any random error and systematic bias of the load cell should be detected. Every experiment is run at least twice to check that

there are no distinct outliers, if this is the case a third test or more are conducted.

Name	Situation
Cal-1	Empty test bench
Cal-2	Assembled test bench
Cal-3	Test bench inside vacuum

Table 6.3: Test goals of Calibration

Because of the test bench's high sensitivity, a short calibration will occur minutes before each thrust experiment. Calibration after each test will also take place to catch any zero point drift [28].

Results and discussion

It was found that the equipment is very sensitive to disruptions, weather conditions and hallway traffic. During experiments the author left the clean room to prevent additional noise. Unaltered data for a test is shown in Figure 6.13a, one can see that the data is noisy, but a clear rise is detected. For each current step the mean value is calculated, and a trendline is determined. As long as the noise is smaller than the signal being recorded, it is not an issue and can be filtered out.

Results of the different calibration tests are shown in Figure 6.13b till Figure 6.13d. Trendlines were added to each test result to showcase the linearity of the load cell. The R^2 value consistently exceeds 0.99 across all tests, affirming the load cell's linear performance. The confirmed linearity in behaviour ensures accurate measurement of load values even beyond the calibrated range. It can be seen that the spread of data increases with increasing ampere. The assembled test bench is shown in Figure 5.5, wires touching the torsion beam created jumps in the calibration data. The test bench in vacuum could only be calibrated to 12 A as the coil overheated faster in vacuum due to the lack of air. As the coil was becoming increasingly damaged due to overheating, 8 A was used in this case to be on the safe side.

In order to say something about all collected data, the normalised value and standard deviation have been computed per calibration set. All data was normalised to 8 A. From Table 6.4 it can be seen that the three standard deviation value increases with added elements to the test bench. This is as expected as more factors influence the thrust. This is also the reason behind the increasing amount of tests conducted per parameter. The three standard deviations value found is higher than the accuracy of the load cell sensor, thus the test set-up itself contributes to the uncertainty. What is peculiar is the drift in mean value, this would have been expected to remain constant, but it varies with approximately 0.2mN. This value is sufficiently small that it might be attributed to insufficient test data. For Cal-1 and Cal-3 the mean value has been comprised of 64 values, Cal-2 is computed with 96 values. Due to the time constraint, no further calibrations were conducted to narrow down the source of this low repeatability.

ID	$F_{LRF,8A}$ [mN]	3σ [-]
Cal-1	4.07	0.62 (15.14%)
Cal-2	3.90	0.99 (25.30%)
Cal-3	4.36	1.81 (41.62%)

Table 6.4: Normalised mean value and uncertainty per calibration

Possible flaws in the calibration method are mentioned, improvement of the calibration method, and test set-up are left for future endeavours. The issue could lie with the method of calibration employed in this section, or with the assembly of the test bench itself. If the latter is the case these issues will reoccur during thrust experiments.

The first point of consideration is the mounting of wires to the test bench, each wire acts as a spring and has the potential to affect the movement of the torsion bench. If the mechanical connections are

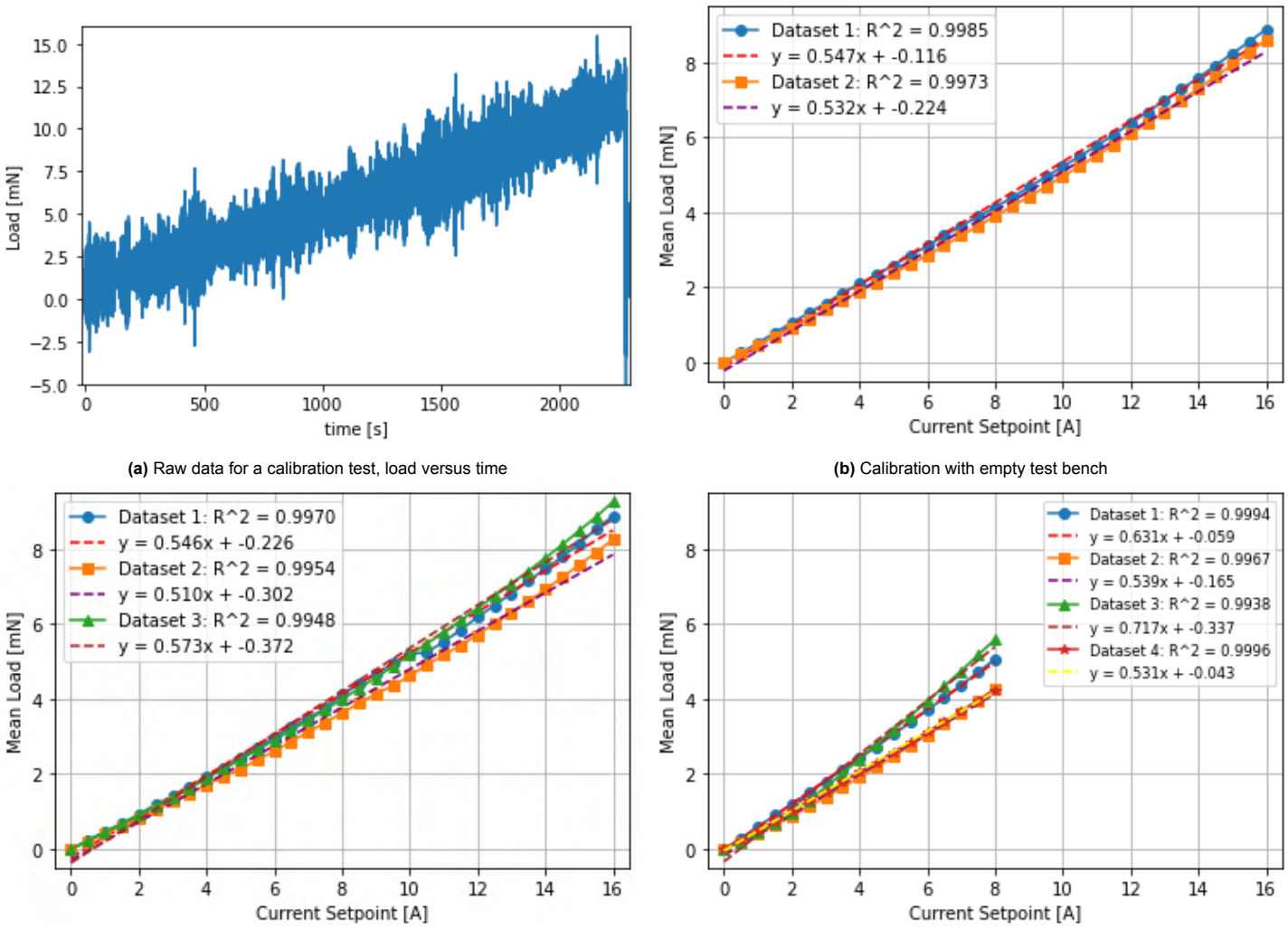

(a) Raw data for a calibration test, load versus time

(b) Calibration with empty test bench

(c) Calibration of assembled test bench

(d) Calibration in vacuum

Figure 6.13: Calibration results

not secured in the middle of the torsion beam, this alters the effective spring constant of the bench and therefore the measured load [28]. It has been attempted to minimise the impact by routing the wires through the middle as shown in Figure 5.5, but they are quite stiff and it would be recommended to get assistance from a technician on how to do this properly.

When the torsion beam is unconstrained it tends to rotate, this indicates that the beam is not level. The levelness of the torsion beam impacts the performance of the test bench. It adds misalignment to the construction and increases friction in the bearing.

Environmental factors such as humidity and temperature could influence the mechanical friction of the test bench. Due to the time required per test and technical difficulties, the calibrations were executed over a span of two weeks. This could have effected the effective spring constant of the test bench.

Electromagnetic interference of the computer and other surrounding equipment might influence the coil's performance. Magnetometers could be used to investigate the magnetic field created by the computer, heater wires and the VTDC and to learn how these fields influence each other.

At the beginning of this subsection a value of 0.823 mN A^{-1} was reported as found by predecessors for the Variable-Turn Density Coil (VTDC). Looking at trendlines found in Figure 6.13 this slope has de-

creased significantly. Due to overheating the VTDC melted the material of the 3D printed structure on which it is mounted. As the coil was wound and glued to this structure it cannot be determined whether the distance between the windings has remained intact and therefore whether the magnetic field has been altered. The arm holding the magnet has to be manually inserted into the coil and aligned with the centre. This is a difficult distance to measure and introduces human error in placement and thus force exerted per ampere. These factors might all have influenced the slope of the calibration curve.

To better understand the system more experiments should be conducted for each test goal. With a large amount of data, one trendline could be established with a standard deviation which gives the accuracy of this test bench. This result could be used during thrust experiments, however at this point there are too many uncertainties as to what caused the deviations from the expected behaviour.

6.3.3. Vacuum effect

While turning on the vacuum pump, it was found that the neutral position of the beam moved. This is shown in Figure 6.14, the measurement is started just before the vacuum pump is turned on and the vacuum chamber is closed when the pressure is sufficiently low and the thrust is seen to not vary anymore. The load cell is represented in voltage as it has a range of -10 to 10 V, and this was a clear indication of how much of this range is lost due to movement induced by pulling the room vacuum. This movement was expected to be caused by the pump removing all the excess air in the room. Once the majority of the air had been pumped out of the room and the pressure was below 10 mbar as shown in Figure 6.15 this hypothesis was tested. The vacuum chamber was closed off from the pump and the pump itself was turned off. This is marked by a lot of noise around the 550 s mark. The beam did not return to its start position.

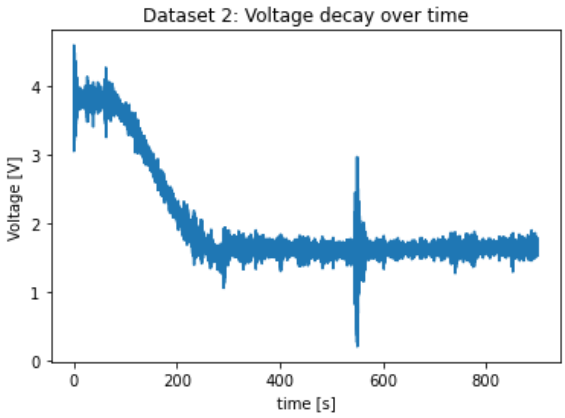

Figure 6.14: Load cell behaviour in vacuum

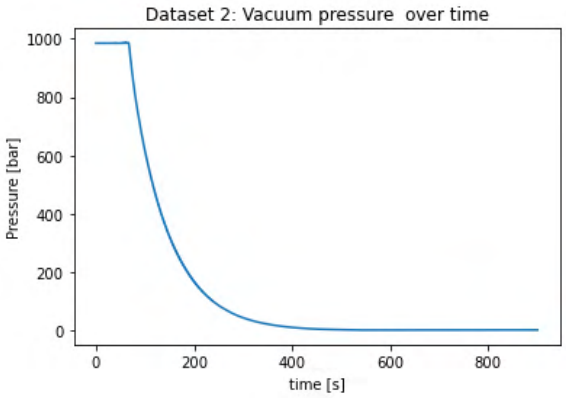

Figure 6.15: Pressure over time

It is unknown what exactly caused this movement since the torsion beam did not move back to its starting position once steady vacuum was obtained and the pump was shut off. Therefore it is unlikely that this is air flow related. Another hypothesis is that friction in the linear bearing must have been too large to overcome for the torsion beam to return to its original position. As the initial movement of the torsion beam is of no concern for the thrust experiments, this phenomenon was left as is. One should be aware of this effect when assembling the test bench as the torsion beam movement is limited before the load cell's maximum compression or expansion is reached.

6.3.4. Calibration with experiments

Calibration was performed before and after each nitrogen experiment to catch any zero-point drift. During these experiments the heaters were turned on. Steps of 1 A were taken and each step had a duration of 60 seconds. Mean values were computed and the zero load measurement was subtracted after initial inspection. The results are shown in Figure 6.16. The expected result for zero-point drift would be that the 'after experiment' line is shifted to above or below the 'before experiment' line but the slope remains intact. This effect is negated by how this graph is generated as the mean value for 0 A is subtracted from the remaining data. Therefore the data should be overlapping, but this is not found.

The linearity of the load cell has proven to be intact, hence something else must be at play here. What can be seen is that the 'before' results generally have a steeper slope than the 'after' results. Higher temperatures also seem to have higher slopes.

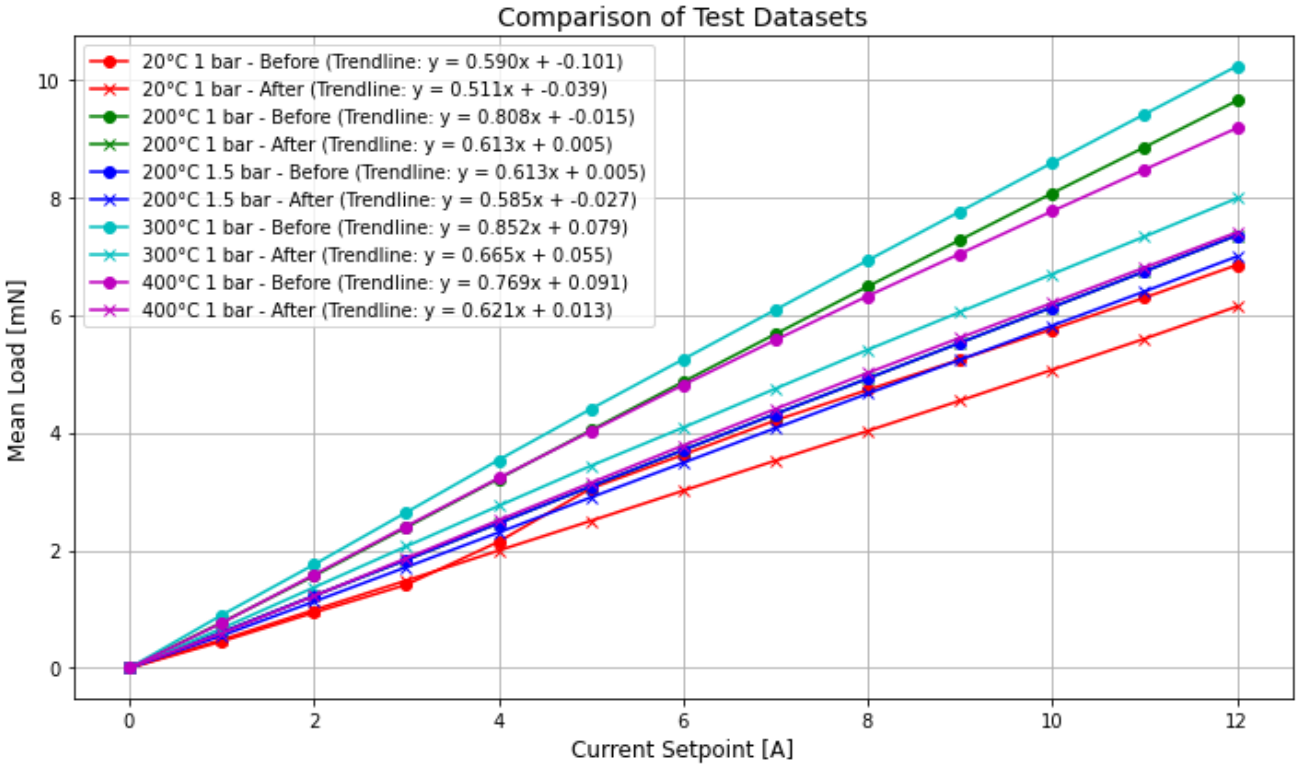

Figure 6.16: Combined calibration data before and after each test

ID	$F_{LRF,8A}$	3σ
20°C 1 bar	4.216	1.130 (26.795%)
200°C 1 bar	5.662	2.262 (39.946%)
200°C 1.5 bar	4.761	0.482 (10.118%)
300°C 1 bar	6.198	2.347 (37.864%)
400°C 1 bar	5.634	2.029 (36.017%)

Table 6.5: Normalised mean value at 8 A and uncertainty of calibrations performed before and after each thrust experiment

Per nitrogen test the before and after data is used to calculate a normalised value and spread again. This is presented in Table 6.5 and it is apparent that the standard deviation is significant. The expected mean value based on the individual calibrations is around 4.1 pm 0.2 mN based on Table 6.4. This value is now around 5.3 mN with an increased variation between experiments. The uncertainty on the measured value is also significant. This effect was already seen when testing the assembled test bench in vacuum. Summarised, turning on the heater and conducting thrust experiments has not adversely affected the uncertainty of the load value found but the measured load has on average increased.

The nitrogen experiments were conducted over a range of temperatures, hence to keep the thruster stable at a set temperature different amounts of power were required. The power chords of each heater were twisted tightly around each other to cancel out the generated electromagnetic field. Any electromagnetic field would influence the coil's performance.

Another hypothesis to explain the difference between calibrations before and after nitrogen experiments is that the magnetic material is heated. The coil acts as an electromagnet when electricity is moving through the copper wire. Due to the resistance of the wire heat is generated. The amount of heat produced is directly proportional to the current squared according to Joule's law. An increased temperature of the wire increases its resistance and decreases the magnetic field strength [29]. It is unknown whether the calibration coil has sufficient time between calibrations inside vacuum to cool down to the initial temperature and how this effects the magnetic field strength.

Due to this large uncertainty in load values, and the unknown factors that influence the load measurements, the calibrations were not used to analyse the thrust data.

6.3.5. Conclusion & Recommendations

It was attempted to calibrate the TB-5.0m for the expected range of thrust from nitrogen experiments, due to the way that the test bench was set up the range of the coil was limited to around 7mN inside vacuum. The uncertainty of the recorded load values is significant with up to 40%. This might be attributed to the construction of the test bench or the calibration method employed.

Proper calibration of the test bench and reason behind this particular behaviour was not achieved during this thesis. For future research, it would be advised to consult with a technical assistant about the proper way to set up such an experiment to be able to identify individual factors contributing to thrust deviations from the expected.

During future calibrations, it would be recommended to move the calibration coil closer to the rotation point to increase the measured load range for the same current. The current-force relation of the load cell is linear, but it would be better to calibrate the entire expected load range of the thruster. This would mean having to redo all experiments.

It would be recommended to 3D print grooves into the Variable-Turn Density Coil (VTDC) mounting structure to ensure reliable distancing of the windings. A structure that aids in the initial placement of the magnet inside the coil would also help keep the force per ampere constant. The wires exiting the coils are now running through the entire vacuum chamber. It would be an improvement if these wires were isolated and wound around each other to reduce electromagnetic interference with other equipment.

For optimal performance, a torsion beam is required to be level. This could be verified by mounting level sensors to the torsion arm and performing measurements inside the vacuum chamber to check the levelness of the surface. Currently, a piece of rubber was used to prevent the test bench from wobbling as the vacuum oven floor was not flat.

7

Nitrogen Testing

Nitrogen testing is used to establish whether the thruster performance has been altered by re-assembly and to quantify this change. In this chapter, first the test goals and approach will be identified, the accompanying test procedures can be found in section C.2, subsequently any noteworthy test occurrences are recorded. Finally, the results are provided and discussed.

7.1. Test approach

At the start of a test campaign, it is important to set up the procedures, test goals, and think about what type of data acquisition is necessary to validate the test goals. Most of this work has already been performed by Hutten [11] and Versteeg [8], Table 7.2 and Table 7.3 are taken from their reports and adjusted where necessary. Experiments using nitrogen as propellant are used to establish whether the thruster performance has been altered by re-assembly and to quantify this change. The obtained data will be verified through comparison with data acquired by Versteeg and Hutten in chapter 8.

Testing with nitrogen is performed in three bursts of five minutes. Five minutes is sufficient to obtain a steady-state mass flow and temperature as the specific heat capacity of nitrogen is relatively low. This is the same sequence that Hutten employed. Versteeg only fired for 15 seconds with the heaters off during firing to avoid the heating wires influencing the thrust measurements.

Before the test commences, all equipment will be turned on and given sufficient time to heat up. This ensures the least measurement inaccuracy as mentioned underneath section 5.2. Once all equipment is prepared, calibration is performed. Ideally, this would be over the entire thrust range, unfortunately the Variable-Turn Density Coil (VTDC) is limited by overheating. The load cell behaviour has proven to be very linear, thus measurements outside the calibration range remain valid. After the nitrogen experiment has taken place, another calibration is performed to catch any effect of temperature on the test bench and zero point drift of the load cell. The results of these calibrations are discussed in subsection 6.3.4.

7.1.1. Parameters

During the test the parameters listed in Table 7.1 are collected, this data is necessary to determine the thruster performance. The temperature on the bracket will be measured to check that it remains below the maximum temperature rating of the pressure sensor.

From the heater current and voltage, the heater power (P_{heat}) and efficiency (η_{heat}) will be computed, to see how much energy from the heater actually goes into the propellant. This is an important thruster characteristic as it shows how much energy is wasted. Furthermore the specific impulse (I_{sp}), discharge coefficient (C_d) and propellant consumption quality ($\xi_{I_{sp}}$) are parameters that describe the thruster behaviour and they will be computed after the test. How exactly this is done can be seen in chapter 3.

Symbol	Description	Location of Measurement
$\dot{m}$	Propellant Mass Flow	In the feed system before entering the vacuum chamber
p_c	Chamber Pressure	At the end of the pressure sensing tube connected to the thruster
p_a	Ambient Pressure	Inside the vacuum chamber
T_c	Chamber Temperature	Clamped between nut and copper
F_t	Force exerted by the thruster	Load cell on the other end of the torsion beam
I_{heat}	Heater Current	Internally measured by the power supply
V_{heat}	Heater Voltage	Internally measured by the power supply
T_{tube}	Temperature of the Propellant Tube	Measured at the bottom of the propellant tube

Table 7.1: Measurement Parameters [11]

7.1.2. Test goals and criteria

Five sets of experiments will be carried out with nitrogen, shown in Table 7.2. To deem whether an experiment will provide meaningful data, certain criteria are set in Table 7.3. If these criteria are not met, this means the test goals have not been reached. The criteria in this case relate to the performance of the sensors being used. They are taken from Hutten [11] with the addition of the thrust being measured with the load cell. Constant means that the maximum deviation is less than $\pm 1\%$ from the average value, excluding start-up and shutdown.

The test goals have been set with the goal of verifying the results obtained by predecessors. The heater implementation of Hutten was such that it was limited to 300°C, a different method has been used in this thesis. It will be demonstrated that higher temperatures of 400°C can be obtained without breaking the heater in the process. The choice of increasing temperature stems from a desire to test the heater capabilities and heater efficiency of this particular resistojet. A variable pressure test has been selected to check that the thruster performs according to theory with an increase in pressure. Each of these experiments is a repetition of the predecessors in order to compare the new thruster iteration with the old one.

Name	Pressure [bar]	Temperature [C]
NI-1	1.0	20
NI-2	1.0	200
NI-3	1.5	200
NI-4	1.0	300
NI-5	1.0	400

Table 7.2: Test goals

7.1.3. Expectations

According to the theory of chapter 3 [15] the thrust should remain constant with increasing temperature. This stems from the relation $\dot{m}c^* = p_c A_t$, with constant chamber pressure (p_c) the right-hand term stays constant. The characteristic velocity (c^*), Equation 3.14, is directly related to the chamber temperature (T_c). Therefore, an increase in chamber temperature decreases the mass flow ($\dot{m}$) to keep the left-hand side of the equation constant. Both the exhaust velocity and the characteristic velocity are correlated to $\sqrt{T_c}$, therefore the decrease in mass flow is balanced by the increase in exhaust velocity in Equation 3.4. As the thrust remains equal between tests but the mass flow decreases, the specific impulse of the thruster is supposed to increase with chamber temperature according to Equation 3.7. In section D.5 several graphs are shown that describe the theoretical behaviour of the thruster. These graphs are later used during validation of the analytical model and contain both theoretical and experimental results, hence they are placed in the appendix. Figure D.10a and Figure D.10b describe the

ID	Description
AC-01	All parameters from Table 7.1 are measured over time through their respective sensors
AC-02	The exhaust is supersonic
AC-03	The performance parameters, i.e. I_{sp}, $\xi_{I_{sp}}$, C_d and η_{heat}, can be calculated with an accuracy of 15% or smaller
AC-04a	The measured chamber temperature remains constant* during operation
AC-04b	The average chamber temperature is within 5% of the target
AC-05a	The measured chamber pressure remains constant* during operation
AC-05b	The average chamber pressure is within 5% of the target
AC-06	The measured mass flow remains constant* during operation
AC-07	The measured thrust remains constant* during operation

Table 7.3: Acceptance Criteria for Nitrogen Thrust Test [11]

thrust and specific impulse behaviour with temperature. The behaviour of characteristic velocity with temperature and its effect on mass flow is displayed in Figure D.10c and Figure D.10d.

As the chamber pressure increases but the temperature remains the same, the mass flow will increase to balance out $\dot{m}c^* = p_c A_t$. This will lead to an increase in thrust, but the specific impulse will be relatively unaffected by the pressure increase as the increase in thrust is divided by the increase in mass flow. Any difference is due to a change in pressure thrust which has a relatively small impact. This is not shown in section D.5 as the inclusion of pressure variation meant that general trends in temperature variation were difficult to distinguish.

7.2. Results

Before processing the results, they are evaluated to ensure that they meet the test criteria. All sensors worked as expected, therefore AC-01 is satisfied. Whether the exit is supersonic as stated by AC-02 is determined with Equation 3.9, where p_c/p_e has to be bigger than a certain factor governed by the specific heat ratio. In the ideal scenario, the flow remains choked at the throat in all experiments. However, the effective throat area is influenced by the presence of the boundary layer, resulting in a modification of the expansion ratio and subsequent changes in exit pressure. The condition remains satisfied in the real case where the expansion coefficient is altered by the discharge coefficient. The performance parameters all have an accuracy below 15%, shown in Table 7.5, this satisfies AC-03. From Figure 7.1 and Table 7.4 it can be derived that AC-04, AC-05 and AC-06 are fulfilled. The chamber pressure and temperature are constant and on target, and there are no unexpected changes in the mass flow. AC-07 requires more careful consideration to determine whether this is the case.

For the five test goals, there are four experiments executed per set of parameters. The averaged result of these experiments is shown in Table 7.4, the subsequently computed performance parameters are shown in Table 7.5. Equations presented in the chapter 3, the analytical model were used to arrive at these values. It was chosen to display them in this order to compare the influence of temperature variation and pressure variation separately.

When observing the performance with varying temperatures, it is observed that the mass flow decreases with increasing temperature. The trend is less linear than expected as the increase between 200°C and 300°C is twice that of the step from 300°C to 400°C. The thrust falls within a range of $\pm$ 0.8 mN, this corresponds with the prediction of the thrust remaining constant with variable temperature. For the variable pressure tests, it can be observed that the mass flow increases. An increasing mass flow means that the thruster expels more propellant and the pressure in the vacuum chamber increases as the pump cannot keep up. A higher amount of particles flow through the thruster, thus more power needs to be supplied to keep the temperature constant. A more in-depth analysis of the

theory compared to test results will follow in section 8.1 where the analytical model is validated. For now, it is verified that the thruster behaves as expected and no significant concerns are detected.

ID	T_c [°C]	p_c [mbar]	$\dot{m}$ [mg/s]	P_{heater} [W]	$F_{thruster}$ [mN]	$T_{ambient}$ [°C]	$P_{ambient}$ [mbar]
NIT-1	21.153 ± 0.323	987.415 ± 5.166	16.501 ± 0.125	-	5.862 ± 0.195	20.903 ± 0.085	8.660 ± 0.749
NIT-4	299.636 ± 0.255	996.355 ± 10.110	11.932 ± 0.034	15.312 ± 0.276	5.112 ± 0.324	22.415 ± 0.505	6.017 ± 0.176
NIT-5	399.441 ± 0.085	994.231 ± 10.638	11.526 ± 0.025	23.908 ± 0.252	5.073 ± 0.131	24.784 ± 0.411	5.991 ± 0.247
NIT-2	199.726 ± 0.059	1000.262 ± 2.403	13.022 ± 0.062	9.087 ± 0.210	5.363 ± 0.083	20.532 ± 0.237	7.136 ± 0.157
NIT-3	199.615 ± 0.004	1515.805 ± 5.458	20.208 ± 0.080	11.085 ± 0.027	8.748 ± 0.032	21.800 ± 0.369	27.119 ± 0.231

Table 7.4: Averaged results of sets of experiments with uncertainty defined as 3σ based on repeatability of experiments

In Table 7.4 the uncertainty is given based on the repeatability of the tests, the three standard deviation value was computed with the average values of the four experiments using Equation 3.36, this gives an absolute value. This value is compared with the sensor error computed in section 5.2. The maximum value out of the three standard deviations of repeatability and sensor error is selected to perform the calculations necessary for Table 7.5. For the chamber temperature and pressure, the sensor error governs the uncertainty, as well as the ambient pressure and temperature. The mass flow uncertainty is that of the sensor with 0.7%. For the supplied power the measurement value is leading. The thrust is sometimes dictated by sensor error of 0.17 mN and sometimes by the repeatability of the experiment. The three standard deviation of up to 40% found during calibration is not considered here as the repeatability of the experiments seems to have improved and more research is required to establish the exact test bench characteristics. These uncertainty values are given as input to the code by Hutten and the error propagation method explained in section 3.2 is used to compute the performance parameters uncertainty.

ID	$R_{t,real}$ [-]	I_{sp} [s]	$\xi_{I_{sp}}$ [-]	η_{heat} [%]	C_d [-]
NIT-1	2993 ± 363 (12.1%)	36.23 ± 1.231 (3.4%)	0.54 ± 0.020 (3.6%)	-	0.69 ± 0.048 (6.9%)
NIT-4	1330 ± 155 (11.7%)	43.69 ± 1.485 (3.4%)	0.46 ± 0.017 (3.6%)	23 ± 2.2 (9.7%)	0.69 ± 0.046 (6.6%)
NIT-5	1130 ± 133 (11.8%)	44.88 ± 1.536 (3.4%)	0.44 ± 0.016 (3.6%)	19 ± 1.8 (9.5%)	0.73 ± 0.049 (6.7%)
NIT-2	1668 ± 195 (11.7%)	42.00 ± 2.554 (6.1%)	0.49 ± 0.031 (6.2%)	27 ± 2.7 (10.0%)	0.68 ± 0.045 (6.6%)
NIT-3	2566 ± 271 (10.6%)	44.14 ± 0.912 (2.1%)	0.53 ± 0.012 (2.3%)	34 ± 2.9 (8.4%)	0.70 ± 0.039 (5.6%)

Table 7.5: Resulting quality factors with uncertainties in the corresponding units and percentage

Results in the form of graphs and tables of all tests can be found in section D.3. In this section, the focus will be solely on the results of the experiment with a chamber temperature of 400°C and any discrepancies discovered in other tests. Figure 7.1 shows the data collected with LabVIEW and Table 7.4 shows the averaged results for the four conducted tests. The four peaks present in each graph represent the time that the propellant valve is opened and thrust is produced. These periods will be referred to as 'thrust period', periods when the valve is closed will be referred to as 'off periods' or 'down periods' as the thruster is shut off during this time. The thrust graph represents the relative thrust produced as the load cell is not set to zero before each test. Post-processing of the thrust data will occur later. One can observe peaks in the mass flow and pressure graphs upon the thruster starting. During the thrust period, the ambient pressure steadily increases due to the addition of nitrogen to the vacuum chamber. The pump is unable to keep the pressure constant but reduces the ambient pressure during the off periods. At the start of the experiment the PID is initiated to keep the temperature constant, this created an initial peak in temperature as the PID tends to overcompensate. There is an initial temperature decrease upon opening the valve and cold nitrogen entering the thruster, towards the end of the thrust period the temperature is stabilising at the set point. When the valve is closed the temperature overshoots but recovers in time for the next thrust period. A similar pattern is followed in the subsequent three tests. This is the same behaviour that Hutten observed [11], which is to be expected as the heater PID was not altered. For the power, it is noteworthy that the temperature is only

recorded at one point on the thruster near the nozzle outlet. The propellant coming in on the other side of the thruster will cool down this portion more significantly. The relevant property for thrust production is the value around the nozzle. While nitrogen is running the thruster is being cooled thus extra power is required to keep the temperature constant.

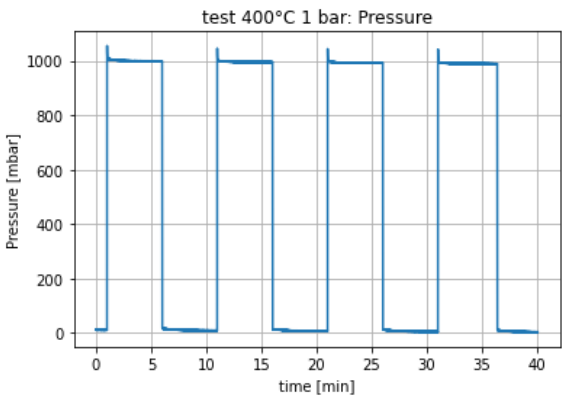

(a) Chamber Pressure

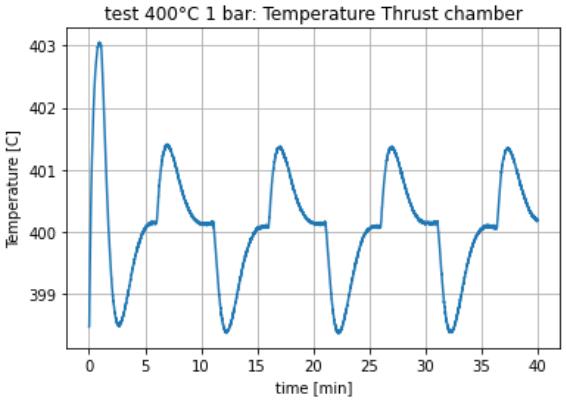

(b) Thrust chamber temperature

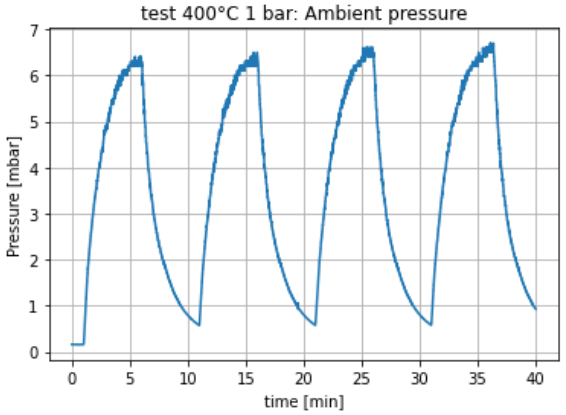

(c) Ambient Pressure

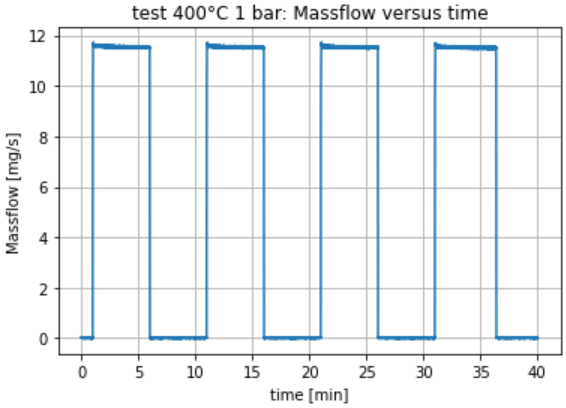

(d) Mass flow

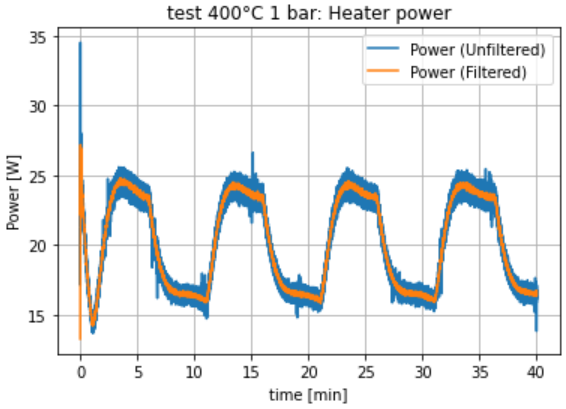

(e) Heater power

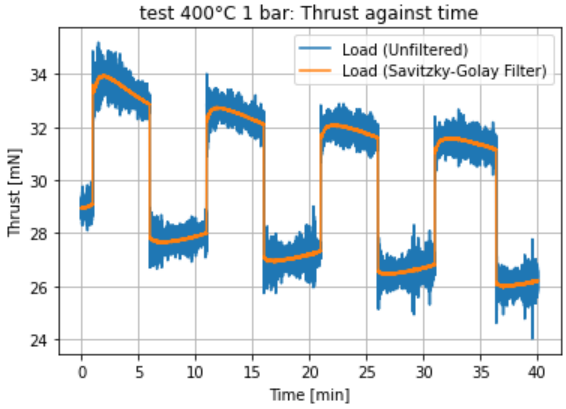

(f) Thrust

Figure 7.1: Results of firing the thruster at 400°C

7.2.1. Thrust analysis

It was found there is drift in the thrust data, for testing at 400°C this drift presents downwards, but for testing at 300°C and temperatures below the thrust curve drifts upwards. This is present both in the thrust and down periods over the entire experiment duration and is therefore called long-term drift. The effect is most prominent at 300°C where the difference between the start of the experiment and

the end is around +6 mN, for 400°C it is approximately -3 mN. The drift was removed by putting a quadratic curve through the down periods as shown in Figure 7.2a and subtracting this from all thrust data. From these down periods, transients around the propellant valve opening (5s) and closing (30s) were removed. This resulted in Figure 7.2b. It was inspected that the step up and down from each experiment was the same, and no other factors were involved. The standard deviation of these steps at 400°C is 0.01 mN or 0.2% of the steady-state thrust value. This is sufficiently small to assume that there is one long-term drift factor and the individual experiments are otherwise undisturbed. A smoothing Savitzky filter is put over the data to visualise the average thrust value.

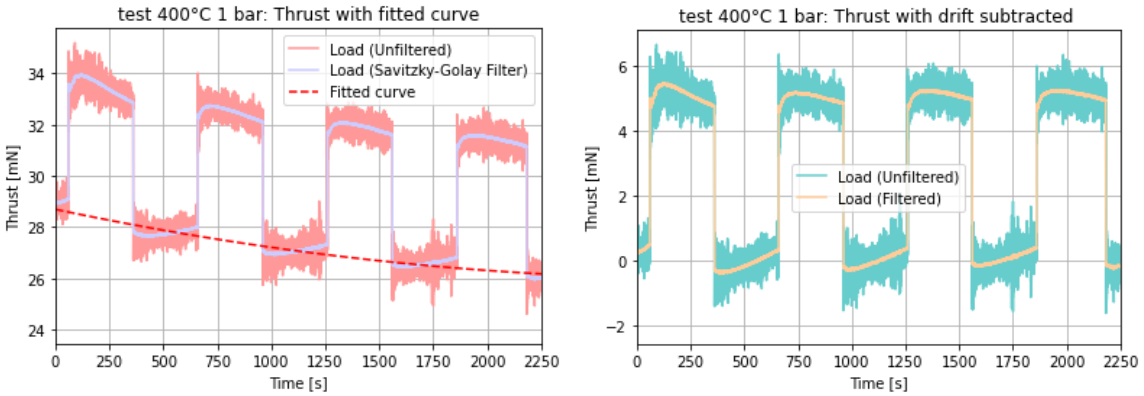

(a) Thrust with a fitted quadratic curve

(b) Thrust curve with drift removed

Figure 7.2: Adjusted thrust curves at 400°C

After removing the long-term drift, it can be seen that something is registering as load while the thruster is off. During the thrust periods the behaviour is curved, something that was not seen by Hutten or Versteeg. One would expect the thrust to peak when the valve opens due to the overshoot of temperature and mass flow and subsequently obtain a steady state. During the first test this curve or peak is more exaggerated, this is why it was chosen to perform four experiments per test goal. This curve is not observed at higher pressures as shown in Figure 7.3. For calculations of the average thrust, the first two minutes of data are excluded to prevent this peak from affecting the results. The maximum difference in thrust value during a single experiment is around 0.32 mN.

The temperature-related drift identified by Hutten upon opening and closing the valve is not present in this data. This absence is expected, as it was associated with a shift in the pendulum's centre of gravity. The use of a different test bench has mitigated this issue. The temperature-related drift would have masked the initial curve observed now, and it is therefore unknown whether this is new behaviour associated with this test bench.

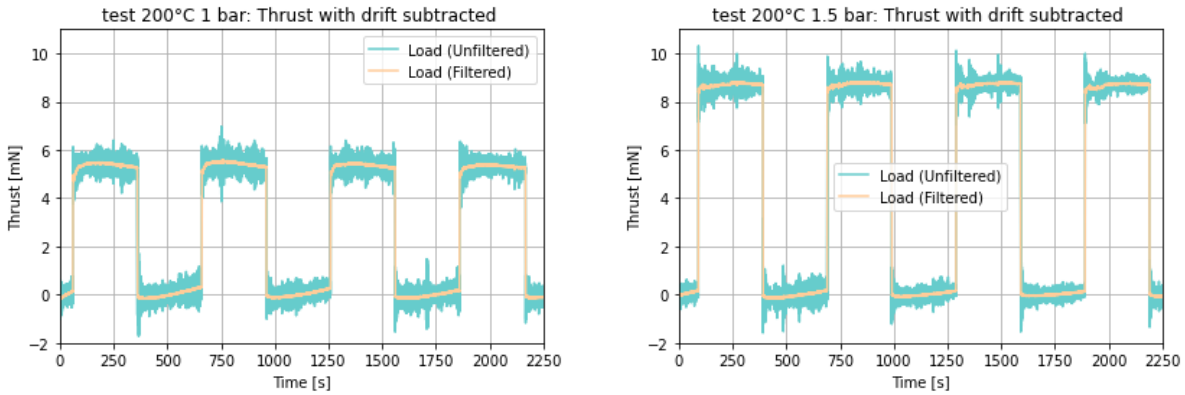

Figure 7.3: Thrust at 200°C and different pressures

It was investigated what might have affected the thrust to create the long-term drift and individual experiment deviations. A multitude of factors that might have affected the thrust are considered and elaborated upon. Several other factors are subsequently proposed that are left for further research to investigate.

During the thrust duration, mass flow and thrust chamber pressure remain constant, the temperature of the thruster varies with a maximum of 1.5°C or 0.38%. Thus the hypothetical thrust should be steady state, and the test bench should be at rest during down periods. With regards to environmental factors influencing the results, all experiments were performed in a span of two days, during the afternoon. The temperature inside the vacuum chamber was recorded during tests and is between 20°C and 25°C. During one set of experiments, the temperature increase is generally below 1°C, the temperature variation increases with thruster temperature and chamber pressure. The ambient pressure varies with around 6 mbar per test, this changes the momentum thrust produced. Using ideal rocket theory equations described in chapter 3 to approximate the thruster behaviour, this increase in chamber pressure could decrease the thrust with 0.2 mN dependent on the exact thrust value. This can partially explain the downwards slope, but does not offer a reason for the curve.

The manner in which the thruster is installed could have caused a variation in thrust throughout the experiment. The thruster is mounted on top of the propellant line which experiences a temperature variation during experiment. The temperature at the bottom of the propellant line was measured during the experiment and is shown in Figure 7.4. The temperature varies by roughly 20°C, Hutten ([11], pp. 64) measured the propellant tube temperature at the top, middle, and bottom and found a similar temperature variation. The linear thermal expansion coefficient of steel has a magnitude of 10^{-5} m/mK [30], with a difference of 20°C this amounts to a change in the propellant tube over the length of 10 cm of 0.02 mm. This means one pillar that holds the thruster is longer than the other, this angle creates a thrust misalignment. The resulting angle would be in the range of 0.1°, and it is therefore unlikely that this is a reason behind the thrust deviation.

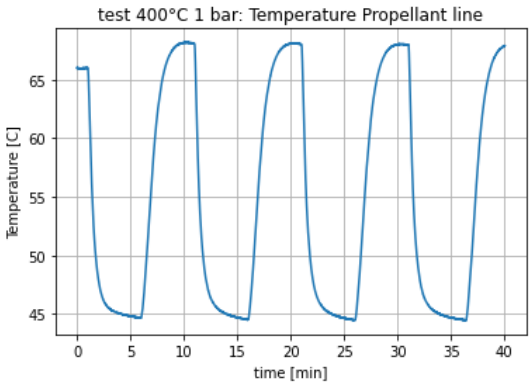

Figure 7.4: Temperature variation of the bottom of the propellant line

The drift during the off periods might be attributed to creep of the load cell, lack of dampening of the torsion arm or an artefact of the drift subtraction. The effect is most prominent at 400°C, indicating that it is temperature-related. During calibration movement of the test bench was detected that is associated with a change in vacuum pressure. This phenomenon remains unexplained, and might also play a role in thrust deviations.

The load cell has been turned on well before the experiments and the expectation was therefore that the load cell temperature remains constant during the experiment. An ambient temperature shift of two degrees Celsius has been taken into account during the computation of uncertainty of the load cell itself, this amounted to an absolute value of 0.17 mN. The temperature of the load cell itself could be monitored during experiments to check that the load cell does not heat up significantly, as convection cannot take place in vacuum.

7.3. Recommendations

Further research is necessary to determine exactly what caused the thrust behaviour. It is difficult on this scale to say something about what effect each of the elements discussed previously has on the test outcome. However one can systematically account for all factors and eradicate them where possible. To troubleshoot this result the following course of action is advised:

- Check the load cell for creep by placing a weight on it for an extended period of time. Previously thirty seconds was used, but as the experiment is five minutes long it would be recommended to use at least that.
- A recommended addition to the calibration would be an 'on-off' load test, comparable to the thrust test done to record whether the test bench returns to the same neutral position after each load measurement. This would determine whether the load discrepancy found is due to the thruster or the test bench, presuming that the Variable-Turn Density Coil (VTDC) behaves as expected.
- Close the vacuum pump during experiments to identify the effect of air flow in and out of the vacuum chamber.
- Apply temperature sensors to monitor the temperature of the bearing as well as the load cell during the experiment. This will tell whether the structure's friction changes over time and whether the load cell drifts due to a temperature shift.

Due to time constraints for the thesis project and another student requiring the test bench, these steps are left as advise for a potential successor and are not executed. One should also be aware that since the conclusion of these experiments the LRF 400 Load Cell has been broken.

Due to the time it takes for the temperature to return to its set point after the test commences combined with the newly found initial curvature, it is advised to extend the test duration to seven or eight minutes in future experiments. During the cold flow test NI-1.4 the propellant valve was accidentally left open for twice the allocated time. Here a significant portion of the thrust is steady state. Longer thrust durations allow for higher confidence in the test results and repeatability as more data is acquired. The Proportional-Integral-Derivative (PID) could also be improved to decrease the settling time of the temperature.

Concerning data acquisition and the LabView code, the author would recommend decreasing the data collection frequency, as LabView memory was on occasion overloaded. To prevent accidents as mentioned in the previous paragraph and aid in ease of testing an automated sequence of valve opening and closing times is also recommended.

8

Comparison with theory & Verification

In this chapter, the results from the experiment are compared to that of the analytical model and recommendations are made on adjustments that can be made for increased accuracy of the analytical model and experimental set-up. Subsequently, the results from the experiment will be compared to the results obtained by Hutten and Versteeg to see how the thruster behaviour has been altered.

8.1. Comparison with analytical model

Experimental results have the purpose of validating the analytical model. If it can be proven that the analytical model predicts the thruster behaviour accurately, within 10%, less testing and design iterations are required to comply with requirements in the future which is cost-efficient. This 10% stems from an inherent inaccuracy in the input parameters of the model due to measurement uncertainties. So far this model has accurately predicted the thrust and specific impulse for both Hutten [11] and Versteeg [8]. The discharge coefficient and specific impulse quality factor have proven more difficult to predict accurately. The corrected behaviour has proven to be closer to reality than the Ideal Rocket Theory (IRT).

The expected analytical results given the test goals have been computed using the model explained in chapter 3 and are displayed in Table 8.1. This table is elaborate such that future researchers can use it for comparison. Several graphs have been made to compare the analytical model output to the experimental output. In Figure 8.1 the results are shown for tests from 20°C to 400°C for 1 bar chamber pressure. The results for 1.5 bar are taken out as they skew the graphs and are not relevant for the comparison performed here. The values for 1.5 bar are present in this report, they are lower than the predicted values but the trend is as expected. What can be seen in Figure 8.1a is that the experimental thrust amounts to one-third of the ideal thrust and half of the corrected thrust. From Figure 8.1b it can be seen that the flow regime in the throat stays relatively in the same order of magnitude, but the discharge coefficients are around 27% lower than predicted.

The difference between theoretical and experimental values can have two causes. One would be flaws in the measurement set-up, the other that the predictions are based on incorrect assumptions. Both options are examined.

Flaws of the measurement set-up could be the misalignment in the connection from the torsion beam to the load cell, or misalignment from the thruster to the test bench connection. This would underestimate the thrust being produced. During calibration it was found that the Variable-Turn Density Coil (VTDC) produced less force than expected based on behaviour recorded by predecessors and there was a large uncertainty present in the thrust value found.

Misalignment of the thrust that exits the nozzle may also have been a factor. The deflection of material into the nozzle is more on one side than on the other and asymmetrical along the width. This would lead to the flow exhibiting not only an outward velocity component in the diverging direction but also a downward or upward component. This deviates from the assumption of purely axial flow. Figure 6.4

		NIT-1	±	NIT-2	±	NIT-3	±	NIT-4	±	NIT-5	±
Input											
T_c	[K]	294.15	6.01	473.15	6.62	473.15	6.62	573.15	7.05	673.15	7.53
p_c	[mbar]	1000	50	1000	50	1500	50	1000	50	1000	50
p_a	[mbar]	10	1.5	10	1.5	10	1.5	10	1.5	10	1.5
Output											
Ideal											
γ	[-]	1.40	0.0	1.39	0.05	1.39	0.05	1.38	0.07	1.37	0.08
F_t	[mN]	15.75	1.03	15.77	1.05	23.83	1.30	15.78	1.04	15.80	1.05
$\dot{m}$	[mg/s]	24.17	1.59	19.02	1.29	28.54	1.60	17.25	1.15	15.87	1.04
I_{sp}	[s]	66.46	0.84	84.50	0.84	85.14	1.05	93.30	0.95	101.49	1.00
c^*	[m/s]	431.37	4.43	547.99	3.81	547.89	4.08	604.46	3.79	656.80	3.83
C_F	[-]	1.51	0.01	1.51	0.01	1.52	0.02	1.51	0.01	1.51	0.01
P_{heat}	[W]	-	-	3.57	0.25	5.36	0.34	5.07	0.35	6.37	0.43
Re_t	[-]	3804	249	2106	130	3160	159	1670	104	1377	83
p_t	[mbar]	52.81	2.71	52.94	2.59	79.40	2.67	53.09	2.63	53.27	2.70
T_t	[K]	244.99	4.84	395.12	5.47	394.98	5.52	480.40	6.21	566.68	6.70
U_t	[m/s]	319.98	3.14	404.58	2.74	404.71	2.74	444.55	2.75	480.85	2.69
p_e	[mbar]	3.58	0.66	3.63	0.70	5.44	1.04	3.69	0.70	3.76	0.69
T_e	[K]	113.34	6.10	185.33	9.27	185.17	10.18	228.97	11.95	275.41	14.02
U_e	[m/s]	612.17	12.14	777.39	13.06	777.25	14.01	857.14	15.33	930.87	16.62
Expected											
C_d	[-]	0.95	0.1%	0.94	0.2%	0.95	0.1%	0.93	0.2%	0.93	0.2%
$\xi_{I_{sp}}$	[-]	0.77	0.9%	0.69	1.4%	0.75	0.7%	0.66	1.6%	0.62	1.8%
ξ_{F_T}	[-]	0.73	1.1%	0.65	1.5%	0.71	0.8%	0.61	1.8%	0.58	2.0%
F_T	[mN]	11.54	0.88	10.254	0.84	16.93	1.03	9.66	0.80	9.12	0.75
$\dot{m}$	[mg/s]	23.05	1.60	17.89	1.26	27.12	1.52	16.11	1.12	14.73	0.975
I_{sp}	[s]	51.04	0.71	58.45	0.95	63.66	0.76	61.16	1.10	63.163	1.10
Re_t	[-]	3698	245	2029	129	3064	147	1062	100	1317	79

Table 8.1: Results of the analytical model given the test goals

shows this asymmetrical nozzle geometry caused by extensive compression.

Due to the construction of the thruster and the limitations of the microscope, the nozzle throat area was not directly measured, but assumptions were made based on a deflection formula and the width exit-to-throat ratio. The significant drop in discharge coefficient compared to the analytical case might be partially attributed to an overestimation of the throat area. If the throat area in reality is smaller than the author estimated this would restrict the mass flow passing through. This has the same effect on the discharge coefficient as viscous effects in the flow. A distinction as to what caused the decrease in experimental mass flow cannot be made. An overestimation of the throat area would also overestimate the ideal thrust and specific impulse.

Efforts were made to minimise surface roughness to decrease friction and consequential boundary layer growth. However, the exact surface roughness of the copper inside the throat area is unknown and the current method of estimating C_d does not allow for the inclusion of surface roughness. Since the optical characterisation of the surface, the copper may have corroded thereby increasing the roughness. Measures were taken to prevent this such as storing the thruster inside ziplock bags but the effectiveness of this method is unknown. This would have led to an overestimation of the C_d value by the theoretical model.

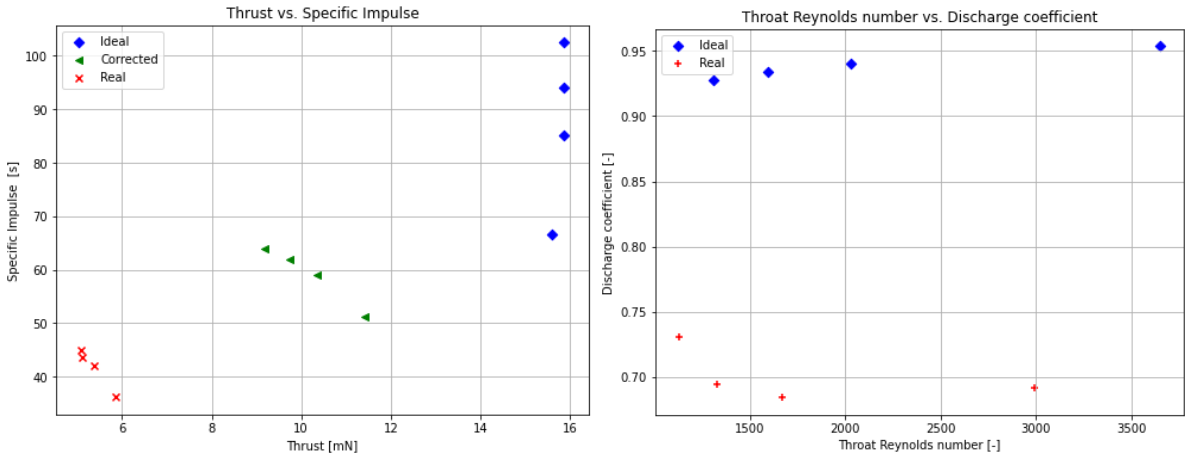

(a) Thrust versus Specific Impulse

(b) Throat Reynolds number versus discharge coefficient

Figure 8.1: Comparison between analytical model and experimental results

The analytical model assumes an axisymmetrical nozzle, this is not the case in this design. Not even the original 2D nozzle shape is intact. Due to the inwards deflection, the exact geometry is unknown but an assumption has been made based on fixed beam situation with a distributed load. This leads to the deflection being maximum at the exit and approaching zero at the throat. The usage of hydraulic throat diameter was supposed to represent any geometry as an axisymmetrical nozzle however this hypothesis seems not to hold up in this case. It is uncertain how a boundary layer develops or what the flow pattern is like as the nozzle converges in one axis and diverges in the other. From literature it is gathered that the additional gas-surface interaction as compared to an axisymmetrical nozzle can lead up to a 20% decrease of thrust for low (Re $\leq$ 500) Reynolds numbers [31]. Viscous effects are less dominant in the regime considered in this project but the effect will still be present. Therefore prediction of performance based on an axisymmetrical nozzle can lead to significant errors. The flow has a three dimensional aspect and modelling it as anything less will underestimate the boundary layer thickness and overestimate the thrust efficiency [32]. The unconventional geometry is only suspected to enhance the 3D behaviour of the flow.

This analytical model uses empirical and analytical relations based on axisymmetrical nozzles to predict thrust behaviour. One might consider more complex models such as Laminar flow Navier-Stokes solver (NS) or Direct Simulation Monte Carlo (DSMC). Here it is important to opt for the 3D model to account for corner effects and subsonic layer growth [33].

The inability of the empirical relations to predict the discharge coefficient was already observed by Hutten as is shown in Figure 8.2. This figure has been made by Hutten, not the author, and 'This work' refers to values from Hutten. The C_d values found by the author are around 0.7. One can observe that especially at lower Reynolds numbers the experimental values deviate from the prediction. The difference is in the order of 10% in the worst case for Hutten. This consistent overestimation of theoretical discharge coefficient can now be attributed to the empirical relations inability to consider the additional gas-surface interaction present in 2D nozzle geometries.

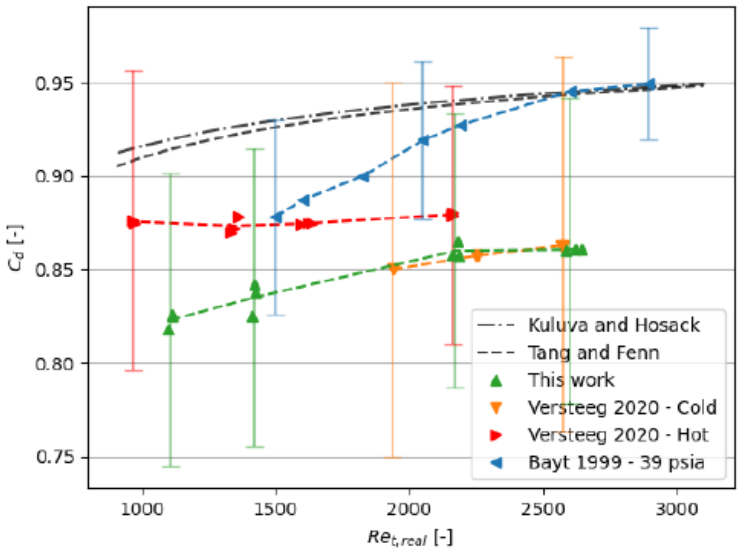

Figure 8.2: Comparison of the discharge factor as a function of the Reynolds number at the throat by Hutten [11]

8.2. Verification

The aim of this section is to compare the thruster to experimentally obtained results from the same thruster at an earlier development stage. This is to verify that the alterations made have not affected the thruster's performance. During this project the thruster was taken apart and re-assembled with mesh inside the chamber and foam in the propellant line. Furthermore, the effect of using a different test bench on the uncertainties and recorded experimental data is of interest.

First, the disparities or similarities of the values and uncertainties themselves are explored. Subsequently, any discrepancies found are investigated. Table 8.2 and Table 8.3 compare the data from this author, Hutten [11] and Versteeg [8]. Data was collected from tables present in their reports. These two data sets were chosen to compare as no other compatible data was available. Versteeg performed most tests at a higher chamber pressure and Hutten did not go above 300°C. It is known that the nozzle geometry was altered due to excessive compression in an effort to make the thruster leak tight. Due to inward deflection of material the nozzle exit is no longer rectangular as discussed in subsection 6.1.2.

What one can observe when looking at the comparison tables is that the chamber pressure and temperature remain constant. Versteeg performed his experiments at a higher vacuum pressure. In comparison to the previous geometry the exit area is smaller and the throat area larger, leading to a lower expansion ratio. The mass flow is equal or higher than previously seen, but the thrust is remarkably lower. The mass flow deviates with 10% from Hutten's value, the thrust is 64% in comparison. This reduction in performance returns in the value for specific impulse and the specific impulse quality factor. The drop in discharge coefficient is significant with a 0.15 or a 17.6% difference. The Reynolds number provides an indication of the flow regime in the throat and remains in the same order of magnitude. This means that the ratio of viscous and inert forces does not vary significantly between the three projects. The heater efficiency is slightly lower than previously found.

The sensor accuracies for the author are reported as absolute or relative per the specific measurement context, the same standard appears not to be upheld by previous students. The instruments used in the experiments are the same by all three researchers, therefore the measurement uncertainty of the temperature and pressure is expected to be the same. This assumption holds for the chamber pressure, for the ambient pressure the other two projects report values above the sensor accuracy, it is unknown why that is the case. With regards to the chamber temperature Versteeg used the pressure sensor's internal temperature sensor during the cold flow, and Hutten decided to use the maximum temperature deviation whereas the author adjusted this per temperature setting. How Hutten ([11], pp. 37) arrived at the uncertainty margins presented is unknown. No explanation or units were offered for the high

Parameters	Cramer	Hutten	Versteeg (Cold)
Input			
T_c [K]	294.3 ± 6.0	$293 \pm 2.4\%$	294.1 ± 1.5
p_c [mbar]	987.4 ± 50	$985 \pm 5.1\%$	1107 ± 5.0
p_a [mbar]	$8.66 \pm 15\%$	$6.7 \pm 19.1\%$	179 ± 28
A_t [$10^3 \mu m^2$]	104.5 ± 15.3	75.3 ± 59	76.5 ± 0.84
A_e [$10^3 \mu m^2$]	359 ± 14.0	580 ± 10	537.6 ± 8.6
H_t [μm]	522 ± 34.3	538 ± 8	496 ± 4
W_t [μm]	200.1 ± 16.2	140 ± 11	154 ± 17
ϵ [-]	3.44 ± 0.64	7.70 ± 61	7.03 ± 0.68
θ [°]	20 ± 0	20 ± 0	20 ± 0
Output			
F_t [mN]	5.86 ± 0.195	$9.21 \pm 1.2\%$	10.43 ± 0.067
$\dot{m}$ [mg/s]	$16.5 \pm 0.7\%$	$14.9 \pm 0.9\%$	16.69 ± 0.12
P_{heat} [W]	N.A.	N.A.	N.A.
I_{sp} [-]	36.23 ± 3.22	$63.5 \pm 1.4\%$	63.77 ± 0.61
Re_t [-]	2993 ± 348	$2586 \pm 17.8\%$	3369 ± 93
C_d [-]	0.69 ± 0.05	$0.860 \pm 9.4\%$	0.85 ± 0.10
η_{heat} [%]	N.A.	N.A.	N.A.
ξ_{Isp} [-]	0.54 ± 0.05	$0.912 \pm 2.0\%$	N.A.

Table 8.2: Comparison of results for 20°C with uncertainty

Parameters	Cramer	Hutten	Versteeg (Hot)
Input			
T_c [K]	472.77 ± 6.6	473.15 ± 1.5	482.0 ± 5.8
p_c [mbar]	1515.805 ± 50	1498 ± 3.3	1510 ± 10
p_a [mbar]	$27.12 \pm 15\%$	8.1 ± 19.8	216 ± 33
A_t [$10^3 \mu m^2$]	104.4 ± 15.3	75.3 ± 59	70.6 ± 4.8
A_e [$10^3 \mu m^2$]	359 ± 14.0	580 ± 10	531.7 ± 5.1
H_t [μm]	522 ± 34.3	538 ± 8	496 ± 4
W_t [μm]	200.1 ± 16.2	140 ± 11	142.3 ± 9.6
ϵ [-]	3.44 ± 0.64	7.70 ± 61	7.53 ± 0.49
θ [°]	20 ± 0	20 ± 0	20 ± 0.4
Output			
F_t [mN]	8.75 ± 0.17	13.73 ± 2.7	12.78 ± 0.083
$\dot{m}$ [mg/s]	$20.208 \pm 0.7\%$	17.7 ± 0.8	16.76 ± 0.12
P_{heat} [W]	$11.09 \pm 0.2\%$	8.96 ± 2.1	N.A.
I_{sp} [-]	44.14 ± 2.63	79.3 ± 2.7	77.75 ± 0.75
Re_t [-]	2566 ± 264	$2183 \pm 16.8\%$	2412 ± 48
C_d [-]	0.70 ± 0.04	$0.857 \pm 8.5\%$	0.871 ± 0.083
η_{heat} [%]	$34\% \pm 3$	37%	43%
ξ_{Isp} [-]	0.53 ± 0.03	894 ± 2.9	N.A

Table 8.3: Comparison of results for 200°C at 1.5 bar with uncertainty

uncertainties in the areas and area expansion ratio and this discrepancy will not be discussed further. As the nozzle geometry is required to compute the thruster performance, the values will be reported here as shown in their original reports. The measurement uncertainties found by Versteeg [8] appear reasonable and based on the microscope capability. A different microscope was used which resulted in a slightly different pixel size, and it is up to the researcher to decide the level of accuracy with which they can distinguish surface features. The uncertainty on the thrust value in this work is based on the sensor accuracy and repeatability found during the nitrogen experiments. However, more work must be done to gain confidence in the test bench characteristics as a high standard deviation was found during calibration of up to 40%. The effect of the test bench is also seen in the specific impulse and consequently the specific impulse quality factor. Hence the found accuracy of the thrust, and related computed values is debatable. The sensor accuracy could be improved by using a load cell with a smaller range. The Reynolds number is linked to the nozzle area, hence the increase in comparison to Versteeg's values is sensible.

To explain the relatively stable mass flow values and drop in thrust, the theory is consulted for the expected behaviour with varying expansion ratio. The expansion ratio is related to the throat-to-exit pressure ratio by Equation 3.6. If the expansion ratio decreases, the exit pressure increases as the flow slows down according to fluid dynamics. According to Equation 3.4, the exit pressure is both part of the momentum thrust ($\dot{m}U_e$) and pressure thrust ($(p_e - p_a)A_e$). How the expansion ratio exactly affects the thrust has been investigated with Figure 8.3 made with python. The configuration of the program is such that the expansion ratio is altered due to a variable throat area and variable exit area respectively. A change in exit area leaves the thrust relatively unchanged whereas a different throat area has a noticeable impact. With the lower expansion ratio due to both a larger throat and smaller exit compared to previous research, the thrust and mass flow values would have been expected to increase.

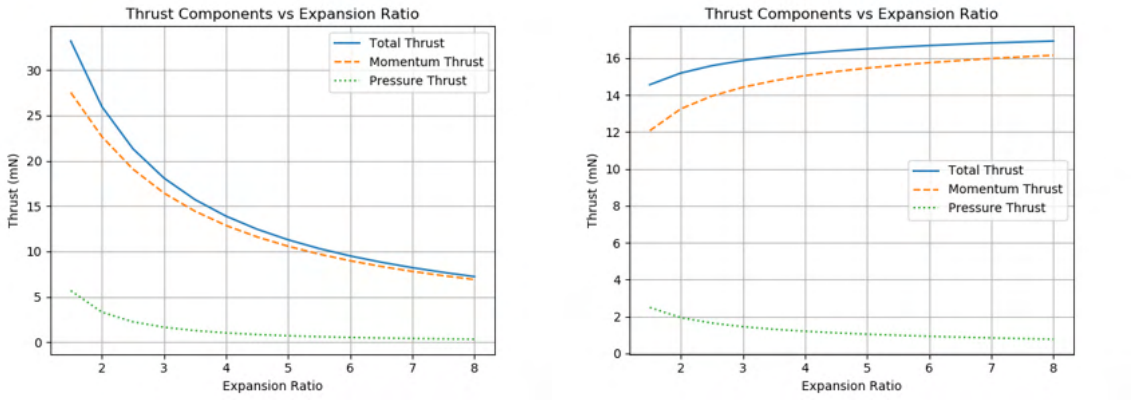

(a) Expansion ratio with variable throat area

(b) Expansion ratio with variable exit area

Figure 8.3: Analysis of the effect of different thrust components

It can be concluded that theoretical predicted behaviour does not correspond to the experimental results found. The mass flow staying close to the previously obtained values might be attributed to the increased drop in discharge ratio. Despite the fact that the mass flow should theoretically be larger there is a 31% decrease with respect to the ideal value due to the discharge ratio, in comparison to the 15% difference between ideal and real mass flow that predecessors experience.

The decreased heating efficiency can be attributed to the modifications made to the thruster. The attachments made for the heater securement protrude to outside the heat shield and the heat shield exit has been adjusted to accommodate the threaded blocks. This means more surface is present outside the heat shield to radiate heat away compared to the thruster before.

The thrust is 36% lower in both tests than Hutten's results. This difference cannot be explained by the discharge coefficient alone. The purpose of this section was to compare the thruster's behaviour to previous research to qualify whether the performance has been altered due to thruster modifications. Hence it is sufficient to say that the difference in nozzle geometry has changed the performance significantly. The reason behind the different performance is outside the scope of this investigation.

8.3. Conclusion & Recommendations

In this chapter, it was found that the thruster did not behave as expected. The thruster performance was roughly half of the predicted behaviour and also deviated significantly from the predecessors. As during previous projects the results from the analytical model did correspond with experimental data, the issue lies with the experiments. During this project, both the test bench and the thruster were changed. This made it unattainable to find the reason for this difference without further research.

To find the cause of the unexpected thruster behaviour one should first characterise the test bench in detail. More calibrations should be executed to better understand its behaviour. A reliable calibration method should be found that obtains repeatable data. Improvements to the set-up and additional testing suggested in previous chapters should reduce the uncertainty significantly.

Secondly, it is important to know the nozzle geometry. The thruster design should be adapted such that movement of the nozzle is restricted, or a method should be devised to measure the throat area. At the very least the nozzle geometry should be restored to its original design, to verify the results. This would allow for distinguishing between thruster alterations and test bench changes during processing of results. It is an important lesson that only one parameter should be varied per set of experiments.

Finally, the analytical design can be improved by finding relations specific to 2D nozzles. Otherwise 3D simulations should be performed to accurately predict correction factors such as the specific impulse quality and the discharge coefficient.

9 Conclusion

In this thesis the author set out to answer the following research questions.

How can the thruster design be improved?

In an endeavour to improve the heat introduction into the current thruster design a thermal paste based on gallium, indium, and tin was used in the heater cavities to promote heat transfer from the heaters to the surrounding structures. This paste fills up all the gaps and therefore promotes conduction. The heaters were secured to the thruster structure to keep this paste contained and prevent the heaters from moving. The heaters performed at elevated temperatures for longer periods and this method of promoting heat transfer is deemed a success.

Mesh was added to prevent blockage of the nozzle and foam was added to the propellant line to promote heating. The foam acts as an additional heat conductor in the supply line to increase the temperature at which the propellant enters the thrust chamber.

How does the experimental set-up need to be modified to decrease the measurement inaccuracy below 10%?

- *How does the experimental set-up need to be modified to fit on the TB-50m?*
- *How should a proper calibration be executed?*

During previous research temperature variations and heavy propellants altered the centre of gravity of the thruster on which the thrust measurement was dependent. This resulted in a measurement inaccuracy above 10% for thrust and specific impulse. In this thesis, the experiments were conducted on the TB-50m which is independent of the centre of gravity of the thruster as opposed to the previously employed TB-5m. A different test bench attachment was designed and manufactured to secure the thruster to this different test bench. Additional care was taken during the assembly of the test bench and calibration procedures to discern and evaluate the specific sources contributing to the observed noise levels and measurement uncertainty. Despite these efforts, quantifying the precise contributions of individual elements proved challenging due to resource constraints. The reason for the difference in slope observed in the current-force relation, as well as the variations in standard deviations, remains unspecified. It was found that the equipment is sensitive to surrounding disturbances, this became apparent from the variable noise level. The uncertainty on load values found during calibration in vacuum is up to 40%. This was attributed to the calibration method with the Variable-Turn Density Coil (VTDC) as the uncertainty derived from the repeatability of thrust experiments yielded a maximum of 6.3%. More research is required to determine the source of this discrepancy and to properly calibrate the test bench. Therefore it cannot be said that the thrust measurement has an inaccuracy below 10%.

Can the thruster performance be estimated by the analytical model suggested by Makhan [7] and elaborated by Versteeg and Pappadimitriou [8, 9]?

There is a significant difference found between the theoretical and experimental values. This distinction can be attributed to both flaws in the thruster manufacturing and experimental set-up as well as limitations of the analytical model to predict real-world phenomena. Specifically, assumptions regarding the discharge coefficient and the axisymmetrical nature of the flow may not accurately represent real-world conditions. Assumptions made in regards to the nozzle's geometry and condition are suspected to have contributed to the significant difference in discharge coefficient of 36%. Therefore, while the analytical model provides valuable insights on expected thruster performance, its reliance on idealised conditions emphasises the necessity for a more comprehensive modelling approaches to accurately predict 2D thruster performance in real-world scenarios.
How well does the thruster performance compare to data obtained by Versteeg and Hutten?

- *What influence does the modified test bench have?*

Two test cases conducted in a vacuum environment were compared to experimental data obtained by previous master's students under consistent input chamber pressure and temperature conditions. During this verification, it was found that the performance of the thruster has deteriorated. A significant deformation of the nozzle geometry has taken place and the expansion ratio (A_e/A_t) has been reduced by 50%. In an effort to make the thruster leaktight with a degraded sealing surface, excessive torque was applied that forced material into the nozzle. As the throat area could not directly be measured assumptions were made with regards to the nozzle deformation. It was hypothesised that there was an increase in the throat area and a decrease in the exit area. The discharge coefficient has reduced by 17.6% compared to previously conducted experiments. The thruster performance is lowered by approximately 40%, but due to the way that the expansion ratio is altered this outcome cannot be easily explained. It can be concluded that the thruster is no longer comparable to the original design and the nozzle geometry should be restored to answer this question.

The difference in test bench removed one type of temperature-related drift found by the predecessors, but added two new types of drift. More investigation is required to identify the reason behind this drift and eliminate it from the data.

10 Recommendations

The original intention behind this thesis was to improve the accuracy of the measurement data for a particular thruster such that the data could be verified and published. Regrettably, due to time constraints and technical difficulties encountered during the course of the study, this objective has not been fully realised. Despite these challenges, the findings and insights gained from this research lay a foundation for future investigations in this area.

Moving forward, it is important to acknowledge that the sealing surface made of copper is found to be non-reusable during this project, as it undergoes deformation during the assembly of the thruster due to compression. Additionally, it is advisable to examine the thruster profile under a microscope for any deformations. To prevent leakage, the sealing surface can be restored by re-machining the copper blocks. The sealing surface is only 0.2 mm thus this operation can be repeated several times before other features of the thruster are impaired. The facilities for this are present at DEMO. An alternative design, where the seal can be easily replaced and is not integrated into the thruster, would be interesting for future research.

To improve the test bench performance, extensive testing is required to identify the source behind the long- and short-term drift observed during the thrust experiment as well as explain the behaviour of the Variable-Turn Density Coil. Calibrations should be repeated a multitude of times to gain confidence in the test bench behaviour and decrease uncertainty.

The analytical model should include a relation based on a 2D nozzle as opposed to the current axisymmetrical relations used to predict the discharge coefficient and nozzle quality. If such relationships cannot be found it is recommended to use 3D simulation methods to correctly predict corner effects and boundary layer growth.

Addressing these concerns should allow for replication of the tests conducted by Hutten with a lower inaccuracy.

References

1. Guo, J., Bouwmeester, J. & Gill, E. In-orbit results of Delfi-n3Xt: Lessons learned and move forward. *Acta Astronautica* **121,** 39–50. ISSN: 00945765 (Apr. 2016).
2. Krusharev, I., Poyck, R., Bellini, Q., Zandbergen, B. T. C. & Cervone, A. *Cubesat Micro-Propulsion Systems for Extending the Capabilities of Academic Projects* in *Proceedings of the 65th International Astronautical Congress* (IAF, Oct. 2014), 1–12.
3. Cervone, A. *et al.* Green micro-resistojet research at Delft University of Technology: new options for Cubesat propulsion. *CEAS Space Journal* **9,** 111–125. ISSN: 18682510 (1 Mar. 2017).
4. Mueller, J. *Thruster Options for Microspacecraft: A Review and Evaluation of Existing Hardware and Emerging Technologies* in (July 1997). https://doi.org/10.2514/6.1997-3058.
5. Guerrieri, D. C., de Athayde Costa e Silva, M., Cervone, A. & Gill, E. Selection and Characterization of Green Propellants for Micro-Resistojets. *ASME Journal of heat and mass transfer* **10** (139 May 2017).
6. Hamann, R., Verhoeven, C., Vaartjes, A. & Bonnema, A. in *Small Satellites for Earth Observation* (eds Sandau, R., Röser, H.-P. & Valenzuela, A.) 319–330 (Springer Netherlands, Dordrecht, 2008). ISBN: 978-1-4020-6943-7. https://doi.org/10.1007/978-1-4020-6943-7_30.
7. Makhan, R. A. *Performance of the MEMS Vaporizing Liquid Microthruster using cold nitrogen gas as propellant An experimental study* MA thesis (Delft University of Technology, Dec. 2018). http://repository.tudelft.nl.
8. Versteeg, H. S. E. *Novel fabrication method for a hot gas supersonic micro-thruster* MA thesis (Delft University of Technology, May 2020). http://repository.tudelft.nl.
9. Pappadimitriou, A. *Performance Evaluation of a Vaporizing Liquid Microthruster using nitrogen and water as propellants* MA thesis (Delft University of Technology, Mar. 2021). http://repository.tudelft.nl.
10. Cramer, L. J. M. *Literature Study: A study into vaporising liquid micro-resistojets* unpublished. 2023.
11. Hutten, R. *Vaporizing Liquid Micro-resistojet experimentation* MA thesis (Delft University of Technology, Feb. 2021). http://repository.tudelft.nl.
12. Cervone, A. *et al. Space Micropropulsion for Nanosatellites* (ed How Cheah, K.) (Elsevier, 2022).
13. Janssens, S. M. J. *Design of a Micro Propulsion Test Bench* MA thesis (Delft University of Technology, Delft, Aug. 2009).
14. Takken, A. *Development of a high-temperature Solar Thermal Propulsion engine* MA thesis (Delft University of Technology, Jan. 2021). http://repository.tudelft.nl.
15. Zandbergen, B. T. C. *Thermal Rocket Propulsion* version 2.09 (Delft University of Technology, Sept. 2022).
16. Tang, S. P. & Fenn, J. B. Experimental determination of the discharge coefficients for critical flow through an axisymmetric nozzle. *AIAA Journal* **16** (1 Jan. 1978).
17. Johnson, A. N., Espina, P. I., Mattingly, G. E., Wright, J. D. & Merklet, C. L. *Numerical characterization of the discharge coefficient in critical nozzles* in *Proceedings of the National Conference of Standards Laboratories Workshop & Symposium* (1998).
18. Kuluva, N. M. & Hosack, G. A. Supersonic nozzle discharge coefficients at low Reynolds numbers. *AIAA Journal* **9,** 1876–1879 (9 1971).
19. Spiszj, E. W., Brinichj, F. & Ju, J. R. *Thrust coefficients of low-thrust nozzles* (National Aeronautics and Space Administration, Oct. 1965).

20. Berton, J. J. *Divergence Thrust Loss Calculations for Convergent-Divergent Nozzles: Extensions to the Classical Case* tech. rep. (Lewis Research Center, Cleveland, Ohio, 1991).
21. Lynn, T. W. *An Introduction to Experimental Uncertainties and Error Analysis for Physics 28* (Harvey Mudd College, 2002).
22. Donald R. Burgess, J. *"Thermochemical Data" in NIST Chemistry WebBook, NIST Standard Reference Database Number 69* (eds Linstrom, P. & Mallard, W.) ().
23. Bijster, R. J. F. *Design, Verification and Validation of a Micropropulsion Thrust Stand* PhD thesis (Delft University of Technology, Jan. 2014). http://repository.tudelft.nl/..
24. Silvestrini, S. *Closed-loop Thrust Magnitude Control System for Nano- and Pico-Satellite Applications* MA thesis (Delft University of Technology, July 2017). http://repository.tudelft.nl.
25. The Lee Company. *Electro-Fluidic Systems Handbook* 9th (The Lee Company technical center, Westbrook, Connecticut, 2017).
26. Torre, F. L. *Gas Flow in Miniaturized Nozzles for Micro-Thrusters* PhD thesis (Delft University of Technology, June 2011). http://resolver.tudelft.nl/uuid:176902dc-7234-414c-af5b-87ef11ec6dc1.
27. Lindberg, V. *Uncertainties and Error Propagation: Part I of a Manual on Uncertainties, Graphing, and the Vernier Caliper* (Louisiana State University, Department of Geology & Geophysics, 2000).
28. Polk, J. E. *et al.* Recommended Practices in Thrust Measurements. *Journal of Propulsion and Power* **3,** 1–17 (33 2013).
29. Harrington, R. E. *Introduction to Electromagnetic Engineering* (Dover Publications, 1987).
30. Awasthi, A., Gautam, A. & Dheer, P. Linear Expansion Coefficient on Different Material Due To Temperature Effect. *International Research Journal of Engineering and Technology (IRJET)* **05,** 4309. ISSN: 2395-0056. https://www.irjet.net/archives/V5/i5/IRJET-V5I5918.pdf (2018).
31. Alexeenko, A. A., Levin, D. A., Gimelshein, S. F., Collins, R. J. & Reed, B. D. Numerical Modeling of Axisymmetric and Three-Dimensional Flows in Microelectromechanical Systems Nozzles. *AIAA Journal* **40,** 985–992 (2002).
32. Markelov, G. N. & Ivanov, M. S. *A Comparative Analysis of 2D/3D Micronozzle Flows by the DSMC Method* in *39th AIAA Aerospace Sciences Meeting & Exhibit* (Reno, NV, 2001), 1009.
33. Louisos, W. F. & Hitt, D. L. Viscous Effects on Performance of Three-Dimensional Supersonic Micronozzles. *Journal of Spacecraft and Rockets* **49,** 51–58 (Jan. 2012).

A

Parts list

Part name	Amount	Material	Specifications
Top sealing block	1	Cu-ETP (unalloyed copper)	Incl. Stainless Steel Tubing
Bottom sealing block	1	Cu-ETP (unalloyed copper)	
Thruster profile	1	Stainless Steel	0.5 mm
Foam heat exchanger	1	Ni-4753	
Mesh	1	RVS 304	
Foam inserts	24	Ni-4753	
M4 Bolts	6	Stainless steel	Torx-head
M4 Nuts	6	Steel	
M4 Washer	6	Steel	
Disk Springs	6 x 6	Steel	Bellevile type, Size: S4214 DIN2093
Shoulder bolts	2	Steel	ISO 7379 M3-04x20
Test Bench Bracket	1	Aluminium	
Left Side Radiation Shield	1	0.5mm Aluminium	
Right side Radiation Shield	1	0.5mm Aluminium	
Truss Brackets		Steel	For shield attachment
M3x5 Bolt	4	Steel	For shield attachment
M3 Nuts	2	Steel	For shield attachment
Liquid metal paste	1	Gallium-Indium-Tin	Amount necessary to fill the gap
Cartridge heater	2	Alloy 600	
Threaded sleeve	2	Messing	For heater securement
Threaded block	2	Copper	For heater securement
MS5837-30BA pressure sensor	1	-	-
MINSTAC VHS solenoid valve	1	-	-
MINSTAC tubing	1	-	-

Table A.1: Parts list with all components attached to the thruster

B

Experiment hardware

B.1. Datasheets

20001149-00 ✓ ACTIVE

MEAS | MEAS MS5837

TE Internal #: 20001149-00

TE Internal Description: MS5837-30BA26 30BA HE LS T&R PRESS SEN

View on TE.com >

Sensors > Pressure Sensors > Board Level Pressure Sensors

Proof Pressure Range: **50 bar**

Pressure: **30000 mbar**

Board Level Pressure Sensor Type: **Digital Pressure and Altimeter Sensor Modules**

Board Level Pressure Sensor Style: **Absolute**

Features

Product Type Features

Board Level Pressure Sensor Type	Digital Pressure and Altimeter Sensor Modules
Board Level Pressure Sensor Style	Absolute

Electrical Characteristics

Board Level Pressure Sensor Supply Voltage	1.5 – 3.6 V

Dimensions

Dimensions	3.3 x 3.3 x 2.75 mm[.11 x .11 x 0.03 in]

Usage Conditions

Pressure	30 bar
Operating Temperature Range	-20 – 85 °C[-4 – 186 °F]

Operation/Application

Resolution	.2
Output Interface	I2C
Proof Pressure Range	50 bar
Pressure	30000 mbar
Output/Span	24 bit ADC
Board Level Pressure Sensor Accuracy	±1.5mbar

Packaging Features

Board Level Pressure Sensor Package	Surface Mountable

Other

Options	High Endurance, Shielded

Load Cell: Futek LRF400

FUTEK
ADVANCED SENSOR TECHNOLOGY, INC.

MODEL LRF400
Load Cell Tension and Compression

FEATURES

- High accuracy
- Overload protection
- For use in both tension and compression
- Integrated connector, detachable cable available
- Notable non-repeatability

IMPORTANT NOTE: DO NOT ROTATE THE LOADING ROD AS IT WILL CAUSE DAMAGE TO THE SENSOR

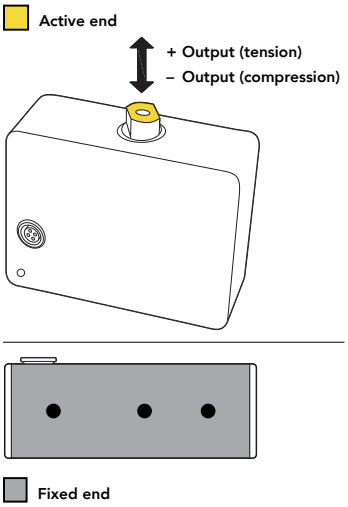

SPECIFICATIONS	
PERFORMANCE	
Nonlinearity	±0.05% of RO
Hysteresis	±0.05% of RO
Nonrepeatability	±0.05% of RO
Creep	±0.05% of Load
ELECTRICAL	
Rated Output (RO)	2 mV/V nom
Excitation (VDC or VAC)	18 max
Bridge Resistance	1000 Ohm nom
Insulation Resistance	≥500 Mohm @ 50 VDC
Connection	4 Pin LEMO Receptacle
Connector Code	CC4
MECHANICAL	
Weight (approximate)	5 oz [140 g]
Safe Overload	See chart on next page
Material	Aluminum, Red Anodized (Housing)
IP Rating	IP40
TEMPERATURE	
Operating Temperature	-60 to 200°F [-50 to 93°C]
Compensated Temperature	60 to 160°F [15 to 71°C]
Temperature Shift Zero	±0.005% of RO/°F [0.01% of RO/°C]
Temperature Shift Span	±0.005% of Load/°F [0.01% of Load/°C]
CALIBRATION	
Calibration Test Excitation	10 VDC
Calibration (standard)	5-pt compression
Calibration (available)	Tension and Compression
Shunt Calibration Value	150 kOhm
CONFORMITY	
RoHS	EU 2015/863
CE	EN55011; EN61326-1

Sensor Solution Source
Load · Torque · Pressure · Multi-Axis · Calibration · Instruments · Software

www.futek.com

CE RoHS ANSI Z540-1 ISO 17025 ISO 9001 ISO 13485 U.S. Manufacturer

Model LRF400

DIMENSIONS inches [mm]

TOLERANCE:
.X ± 0.1" [2.5 mm]
.XX ± 0.01" [0.25 mm]
.XXX ± 0.005" [0.127 mm]

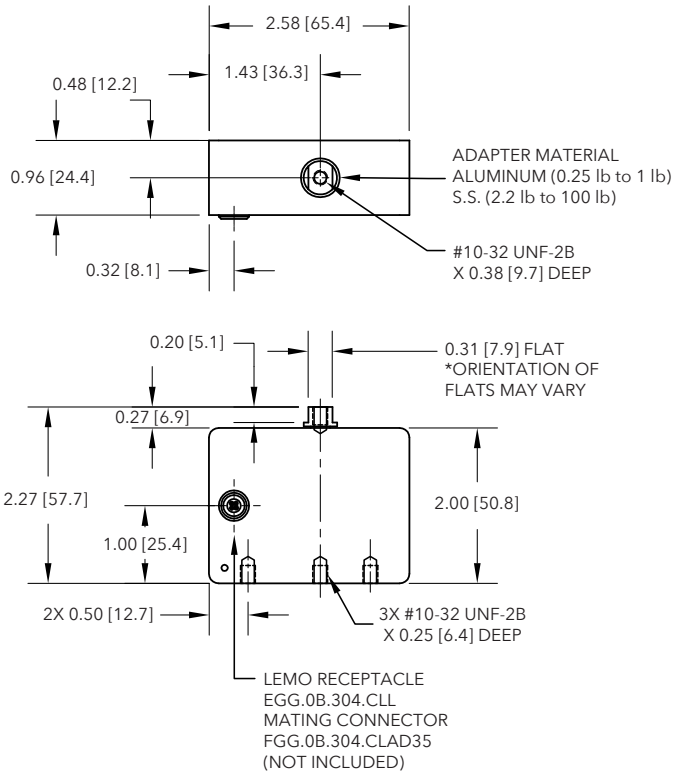

CAPACITIES

ITEM #	lb	N	Safe Overload (lb)	Deflection (in)	Natural Frequency (Hz)
FSH04036	0.25	1.1	50	0.0078	120
FSH04037	0.50	2.2	50	0.0075	170
FSH04038	1	4.5	50	0.0067	260
FSH04039	2.2	9.8	250	0.0084	210
FSH04040	5	22.2	250	0.0065	350
FSH04041	10	44.5	250	0.0059	520
FSH04042	25	111	250	0.0052	860
FSH04043	50	222	250	0.0050	1250
FSH04044	100	445	250	0.0050	1760

LEMO 4-PIN (CC4)

PIN	COLOR	DESCRIPTION
1	Red	+ Excitation
2	Green	+ Signal
3	White	– Signal
4	Black	– Excitation

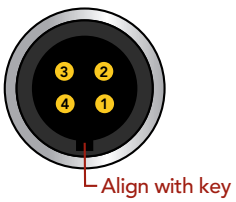

Drawing Number: FI1435-C

10 Thomas, Irvine, CA 92618 USA
Tel: (949) 465-0900

www.futek.com

CE RoHS ANSI Z540-1 ISO 17025 ISO 9001 ISO 13485 U.S. Manufacturer

Nitrogen mass flow meter: Brooks 5850S

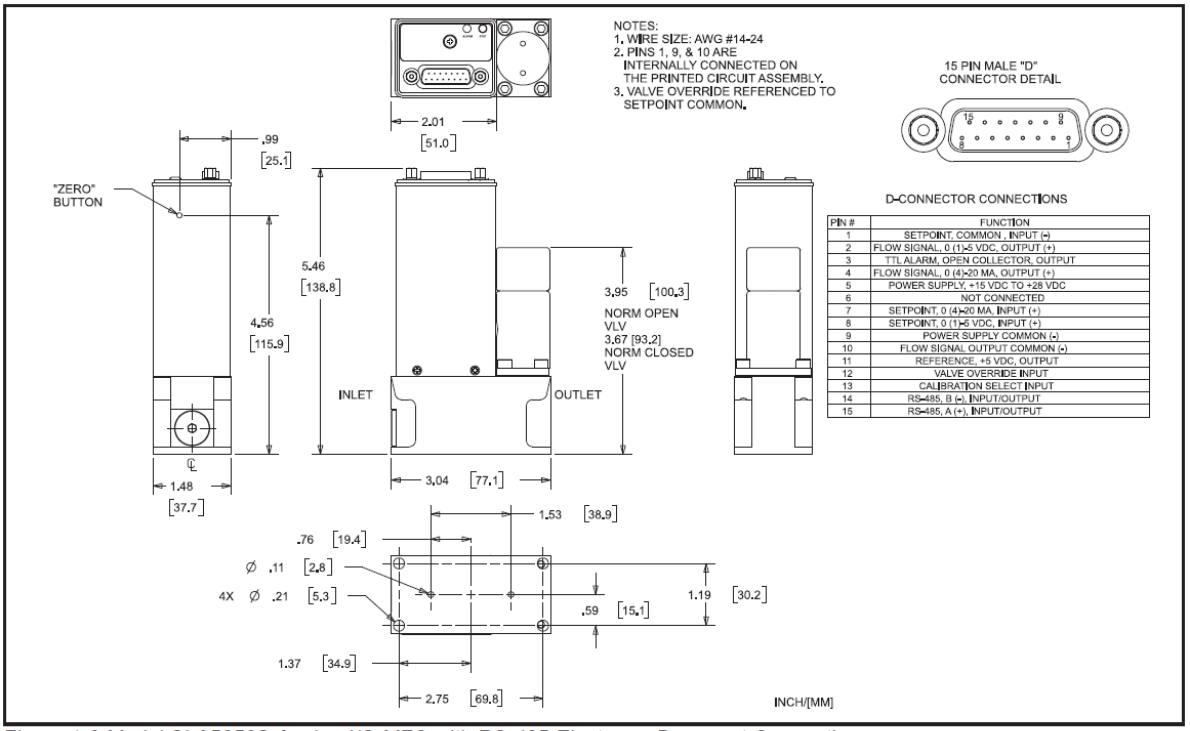

Figure 1-6 Model SLA5850S Analog I/O MFC with RS-485 Elastomer Downport Connections

Cartridge heater: Watlow 1/8-Inch FIREROD®

SPECIFICATION SHEET

1/8-Inch FIREROD® Cartridge Heaters

Miniature FIREROD® Provides Maximum Performance Where Space is Limited

When an application requires heat delivered into a small space with minimum weight, the 1/8-inch diameter FIREROD® cartridge heater from Watlow® is the ideal solution.

This swaged constructed miniature cartridge heater features high watt density, high operating temperature capability and provides long life in applications where it is essential to have a very small size.

Like all Watlow FIRERODs, the 1/8-inch maximizes heat transfer utilizing resistance wiring close to the heater sheath, isolated by a thin layer of compacted MgO insulation.

For this and other Watlow heaters, customers can also specify lead length and choose from a variety of lead options. Leads can be insulated with fiberglass or PTFE or protected by stainless steel braid or hose.

Watlow's 1/8-inch FIRERODs also have an option many others lack: the ability to have an internal J or K-type thermocouple located near the tip of the heater.

Typical Applications

- Burn-in chip test system
- Mass spectrometry
- High-definition ink jet printers
- 3D printing, fused deposition modeling
- Gas chromatography
- Respiratory equipment
- Gas analyzers
- Freeze protection
- Packaging equipment

Features and Benefits

Miniature size
- Delivers high performance in a small package
- Supports a wide variety of application requirements

Low mass
- Provides quicker response time
- Increases heater life
- Lowers internal temperature

Swaged construction
- Provides higher watt density and higher temperature capabilities
- Allows maximum heat transfer
- Increases safety due to low leakage current

Optional internal thermocouple
- Reduces system footprint
- Measures temperature at point of application

Manufactured to the highest quality standards
- Outlasts competitors in life testing
- Backed by over 50 years of industry expertise

Numerous lead options available
- Designed for flexibility and performance

WATLOW®
Powered by Possibility

Specifications

Sheath
- Alloy 600 is standard
- 304 stainless steel is available

Maximum application temperature
- 1400°F (760°C)

Maximum voltage
- 240V

Maximum wattage at 240V
- 744 W

Maximum amperage
- 3.1 amp

Wattage tolerances
- +10 percent, -15 percent

Dimensions
- Actual diameter is 0.122 in. (3.10 mm) ± 0.002 in. (0.05 mm)
- Minimum overall length is 0.875 in. (22.22 mm) (Minimum length may change based on lead construction, volts and watts, please consult factory.)
- Maximum overall length is 12 in. (304.8 mm)
- Length tolerance 3.5 in. (89 mm) and less ± 3/32 in. (2.4 mm)
- Length tolerance greater than 3.5 in. (89 mm) ± 3 percent

Construction
- Solid lead wire is standard, but stranded is available
- Lead options (see illustrations):
  - Crimped-on
  - Swaged-in
- Lead types are:
  - Fiberglass 482°F (250°C)
  - High temperature fiberglass 842°F (450°C)
  - PTFE 392°F (200°C)
- Moisture resistant option: Welded end-disk is standard with PTFE seal and leads available
- Internal thermocouple available
  - Thermocouple embedded in the end-disc "C" location
  - Thermocouple junction is grounded
  - Type J or K available (solid lead wire)
  - Swaged-in, fiberglass 482°F (250°C)
  - Swaged-in PTFE 392°F (200°C)
  - For available lengths, consult factory
- Lead protection options
  - Stainless steel braid crimped over lead end
  - Stainless steel flexible hose crimped over lead end
- Other options
  - Bent heaters, in no-heat section, up to 90° angle
  - One inch diameter mounting flange (FS flange)

Average Hours of Operation During Stress Test Failure

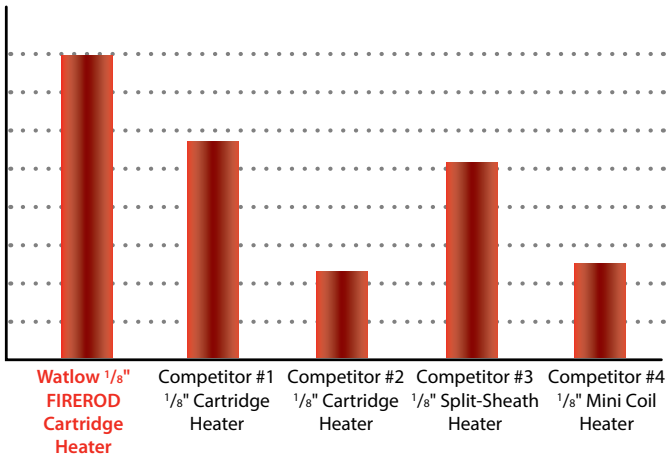

Lead Options

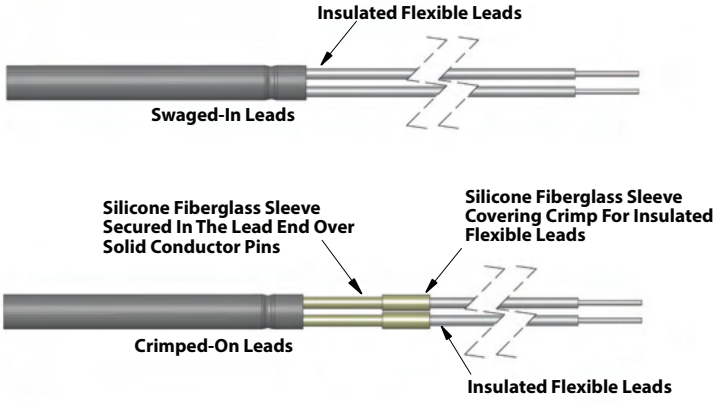

Internal Construction

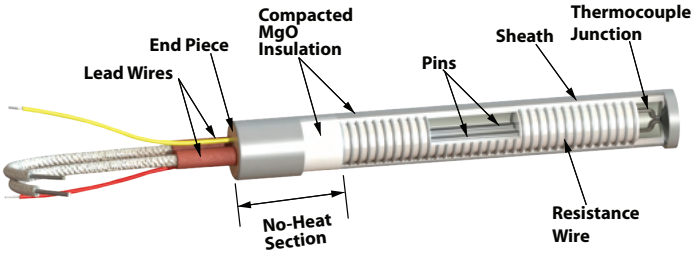

Powered by Possibility

To be automatically connected to the nearest North American Technical Sales Office:
1-800-WATLOW2 • www.watlow.com
inquiry@watlow.com

International Technical Sales Offices:

China	+86 21 3532 8532	Italy	+39 02 4588841	Singapore	+65 6773 9488
France	+33 1 41 32 79 70	Japan	+81 3 3518 6630	Spain	+34 91 675 1292
Germany	+49 7253 9400 0	Korea	+82 2 2169 2600	Taiwan	+886 7 288 5168
India	+91 40 6661 2700	Mexico	+52 442 256 2200	UK	+44 115 964 0777

B.2. Electrical diagram

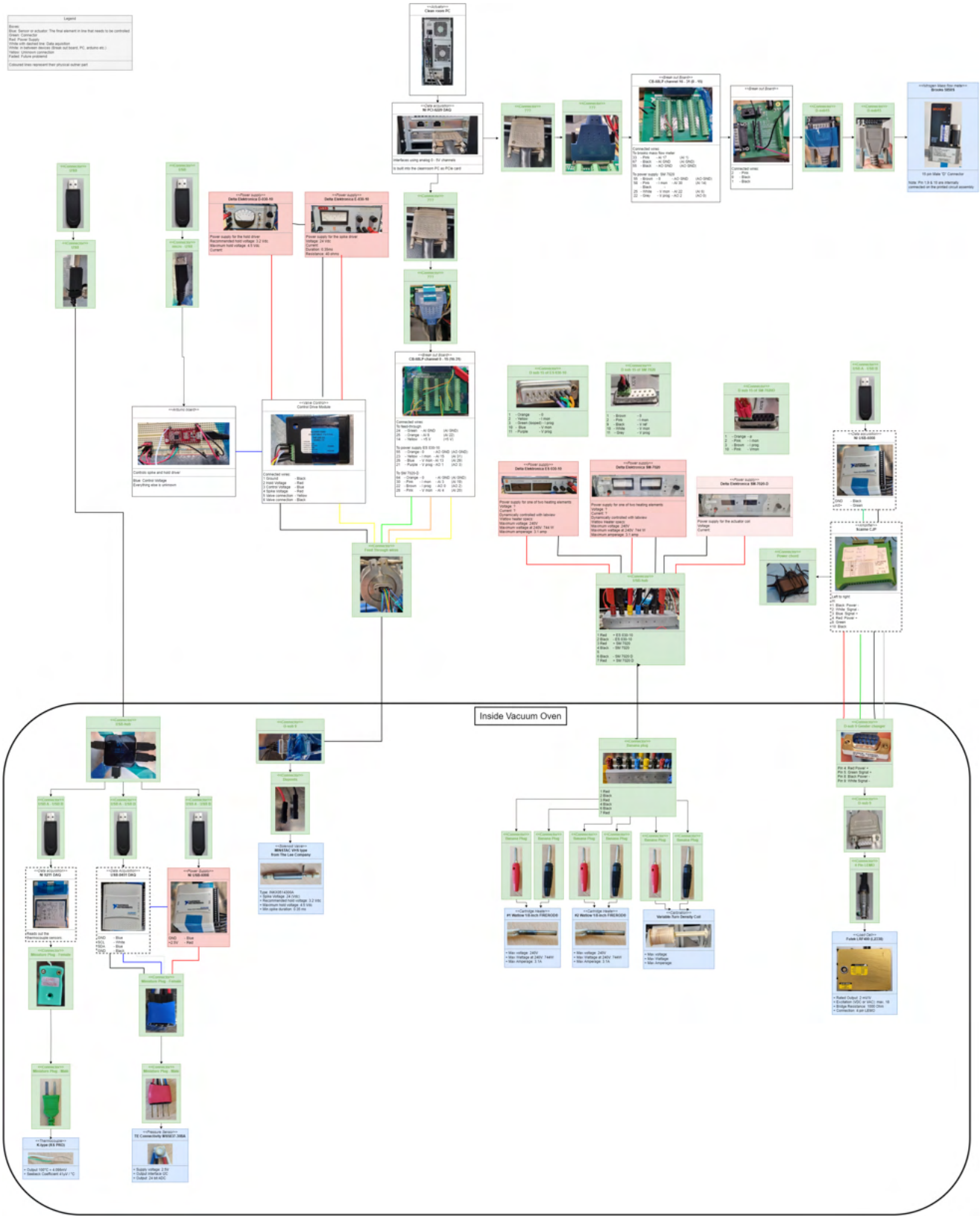

Figure B.1: Electrical diagram of the test set-up

C

Test procedures

Procedures are an important part of conducting tests. Make sure that procedures are printed with each tests being conducted and mark each step that is executed. This makes testing a safe and repeatable process.

C.1. Leak testing procedures

These procedures are taken from Versteeg [8] and were modified when necessary. Steps were added to increase the safety of the system, thorough leak testing of the system is only necessary after long periods between tests as overtime connections can become lose. Always be mindful of the section of the feedsystem that is pressurised, and where the pressure will go once a valve is opened.

*

Leak test preparation

1. Connect the Brooks 2000 sccm mass flow sensor (right) to the breakout board behind the vacuum chamber and plug in its power brick (45 min warm-up time) (only for mass-flow based testing).
2. Turn on the E-030-1 and D-030-1 power supplies behind the vacuum chamber.
3. Turn on the clean room computer next to the vacuum chamber, and start LabVIEW after having logged in (the computer is relatively slow to start, other tasks can be completed in parallel).
4. Ensure the tubing leading to the vacuum chamber is connected to the feed system at the specified mass flow sensor.
5. Ensure the valve override switch on the breakout board is set to ON.
6. Connect the thruster to the tubing for inside the vacuum chamber. Use the MINSTAC torque wrench together with a 5⁄32 inch wrench for tightening the connections. The minimum torque is achieved by pressing the shorter torque arm clockwise until it just contacts the longer arm. Instruction can be found in the Lee company manual L12.
7. Place the thruster inside the vacuum chamber and plug in the propellant tubing quick connect fitting to the connection in the top rear left of the chamber.
8. Place the NI UBS-8451 and USB-6008 DAQs inside the chamber with the I²C cable interface and plug both into the USB hub on the back wall inside the chamber.
9. Connect the cable from the pressure sensor on the thruster to the I²C interface (colour coded for alignment).
10. Connect the valve electrical pins to the spike and hold driver with a feed-through cable via the 9 pin connector taped to back of the left wall. Pin 6 and 7 are the correct wires to hook up. When looking at the valve with the pins facing towards you, and the direction of flow pointing upwards, the red wire should be on the right.
11. Open LabVIEW and verify that the valve works (you should be able to hear it click)
12. Verify that all connections are hand tight.

13. Verify that the high-pressure shut-off valve at the bottom of the feed system board is closed.
14. Verify that all manual valves are closed, they should be orientated perpendicular to the flow direction, indicating that it is blocked.
15. Verify that the pressure regulator is fully closed by turning it counter-clockwise until a physical stop is reached.
16. Wear protective glasses.
17. Have gas leak detection spray and paper towels at the ready, and any required wrenches to tighten the system.
18. Clear away any cluttering items and make sure there is a clear path to the exit.
19. Inform any other people working in the clean room that you will be working with a pressurised system.
20. Open the main valve on top of the N2 cylinder, located behind the feed system board. Turning one time counterclockwise suffices.
21. Check for leaks (both by ear and with the spray).
22. Open the high-pressure shut-off valve at the bottom of the feed system board.
23. The high-pressure gauge now indicates the pressure inside the N2 cylinder. If this is close to zero, the cylinder should be replaced according to the instructions on the board.
24. Slowly adjust the pressure regulator upward to the desired value for the feed-system pressure by carefully rotating it clockwise. The pressure in the feed system (relative to atmospheric) can be read-off on the low-pressure gauge.
25. Open the low-pressure shut-off valve (long red handle) by aligning it with the direction of the tubing.
26. Open the selection valve (small yellow knob) to the rightmost mass flow sensor, again by aligning it with the tubing.
27. Check for leaks (both by ear and with the spray).

Flow rate leak test

1. Open leak_test.vi with LabVIEW.
2. Specify the desired test name and folder to save data in, then run the program.
3. Open the valve to the thruster from LabVIEW and allow the mass flow rate to be recorded for at least 30 seconds to obtain a steady state value (initial response will show a mass flow peak to fill the thruster).
4. Close the valve to the thruster from LabVIEW and stop leak_test.vi.

Pressure dynamics leak test

1. Plug the nozzle exit with rubber pieces and a clamp. Use tape to keep the rubber steady during clamp tightening.
2. If tests are to be performed in vacuum, close the chamber door and turn on the vacuum pump, wait roughly 15 min to reach minimum vacuum pressure between 20 and 30 Pa.
3. Open leak_test_no_mf.vi with LabVIEW.
4. Specify the desired test name and folder to save data in, then run the program.
5. Open the valve to the thruster from LabVIEW until the thrust chamber pressure remains constant over time.
6. Close the valve to the thruster and record pressure over time for the desired period. For very low leakage flows this can take multiple hours or days, while for relatively severe leaks it may only take minutes or seconds.
7. When sufficient time has passed, stop leak_test_no_mf.vi.

Leak test shut-down

1. If tests were performed in vacuum, first close the valve between the chamber and the pump (handle left of the door), then turn off the pump and open the pressure-equalization port on the front of the chamber to allow air to enter it once more.
2. Open the vacuum chamber door once ambient pressure inside of it has been restored.
3. Close the main valve on top of the N_2 cylinder.
4. Close the high-pressure shut-off valve.
5. Turn the pressure regulator fully counter clockwise, so that it will start at zero outlet pressure for subsequent tests, and gas in the high-pressure line between the cylinder and the regulator is not wasted. **note:** this method should only be used if testing is conducted on consecutive days, otherwise the high pressure line should also be purged.
6. Remove the rubber and clamp plug from the nozzle. Some gas might be released
7. Bleed the low pressure section of the feed system to ambient conditions by opening the thruster valve from LabVIEW with the same program as used for performing the test.
8. Close LabVIEW, copy the acquired data to a USB-drive and turn off the computer.
9. Close the low-pressure shut-off and selection valves.
10. Turn off the E-030-1 and D-030-1 power supplies.
11. Optional steps to completely disassemble the set-up and take the thruster out of the vacuum oven.
    (a) Unplug the mass flow sensor power brick.
    (b) Uncouple the propellant quick connect at the back inside the chamber
    (c) Uncouple the MINSTAC tubing from the valve (can be done by hand or with the wrenches specified).
    (d) Disconnect the pressure sensor and valve electrical wiring.
    (e) Unplug the NI UBS-8451 and USB-6008 DAQs.

C.2. Nitrogen testing procedures

What here follows is an extensive list of instructions for testing the thruster using nitrogen as propellant. Steps for heating can be skipped when the aim is cold gas testing, this includes turning on power supplies SM-7020 and ES-030-10. Part of the checklist under section C.2 Preparation might already be completed, however the test conductor should check that all these tasks have been completed in order to avoid mistakes.

Preparation

1. Turn on and/or plug in the components requiring warm-up or start-up time:
    (a) Turn on the SM-7020-D, SM-7020, ES-030-10, E-030-1 and D-030-1 power supplies (60 min warm-up time).
    (b) Make sure that the Brooks 5850S mass flow meter is plugged in (45 min).
    (c) Turn on the clean room computer next to the vacuum chamber, and start LabVIEW (5 min).
2. While the previous devices are warming up, install the thruster on the thrust bench, outside of the vacuum chamber:
    (a) Connect the heat shield, taking care of all cables coming from the thruster.
    (b) Connect the valve to the MINSTAC connector end propellant tubing inside the vacuum chamber. Use the MINSTAC torque wrench together with a 5⁄32 inch wrench for tightening the connections. The minimum torque is achieved by pressing the shorter torque arm clockwise until it just contacts the longer arm. Instruction can be found in the Lee company manual L12.
    (c) Use 4 M4 screws with washers to attach the thruster securely to the end of the torsional beam
    (d) Take length measurements to determine the force conversion factor between the magnetic actuator force, thrust force and load cell.
    (e) Attach thermocouples with small pieces of tape

(f) Route cables for the $p-T$ sensor, valve, thermocouples, heaters and the propellant tubing over the side of the torsional beam, from the thruster to the pivot in the middle to minimise added stiffness.
(g) Secure cables and tubing using small pieces of tape.
(h) Centre the magnet arm to the coil and align its end to (7.1 ± 0.1) cm from the high coil density side of the actuator, while the pendulum is pressed against the distance sensor.

3. Move the thrust bench inside the vacuum chamber, with the magnetic actuator facing to the side:

(a) Ensure the power patch-through panel is at the opposite side of the vacuum chamber relative to the magnetic actuator.
(b) (If not already present:) Plug in the two NI DAQs to the USB dock in the vacuum chamber.
(c) Attach the I²C cable from $p-T$ sensor to the NI USB-6008 and NI USB-8451 DAQs through the color-coded interface cable.
(d) Plug in the propellant feed tube quick-connect at the rear top-right corner of the vacuum chamber.
(e) Plug in thermocouples to NI-9211, write down which sensor location corresponds to what port.
(f) Run the magnetic actuator cables to be primarily perpendicular to the coil length axis at first and in a wide loop later, and plug these into ports 6 and 7 on the power patch-through panel (color coded for + and -).
(g) Ensure that the magnetic actuator cables do not touch the walls of the vacuum chamber.
(h) Twist the heater cables around each other, this blocks the magnetic field it generates and prevents interference.
(i) Plug in the heaters to port 1-4 on the power patch-through panel, one heater occupies port 1-2 (color coded for + and -), the other 3 (Red) and 4 (Black).

4. Test if all sensors and actuators are working:

(a) Open thrust_test_heated_N2.vi with LabVIEW.
(b) Specify the desired test name and folder to save data in, then run the program.
(c) Temporarily open the MINSTAC valve and verify that the mass flow sensor is measuring a flow of propellant.
(d) Turn on one of the heaters at 10 Watt and verify that the temperature of the thruster is going up. Turn the heater off. Repeat this step for the other heater.
(e) Verify that the remaining sensor and actuator data being recorded makes sense, fix possible issues that come up. ($p-T$ sensor, thermocouples and load cell)
(f) Stop thrust_test_heated_N2.vi.

5. Open up the feed system:

(a) Verify that all connections are hand tight.
(b) Verify that the high-pressure shut-off valve at the bottom of the feed system board is closed.
(c) Verify that all manual valves are closed, they should be orientated perpendicular to the flow direction, indicating that it is blocked.
(d) Verify that the pressure regulator is fully closed by turning until a physical stop is reached and the thread is visible.
(e) Wear protective glasses.
(f) Clear away any cluttering items and make sure there is a clear path to the exit.
(g) Inform any other people working in the clean room that you will be working with a pressurised system.
(h) Turn the handle on top of the N2 cylinder $\sim 180°$ counter-clockwise to open its main valve.
(i) Listen whether there is a leak.
(j) Open the high-pressure shut-off valve.
(k) Check that the cylinder pressure, as indicated on the high-pressure gauge, is still above the desired test pressure; otherwise, abort the test and have the N2 cylinder replaced according to the instructions on the feed system board.
(l) Open the red low-pressure shut-off valve and yellow selection valve toward the mass flow sensor in use, by aligning the handles with the tubing.
(m) Slowly open the pressure regulator valve (clockwise) until the indicator for the downstream pressure has moved ever so slightly, the small gas burst going through can also be heard.

Environment setup

This section describes the steps to turn on the vacuum chamber and heat up the thruster.

1. Turn on the vacuum chamber:
   (a) Specify a folder and test name and click run to start thrust_test_heated_N2.vi in LabView.
   (b) Make sure the heating power is set to 0 Watt and the temperature control setpoint to 0 °C.
   (c) Make sure the vacuum chamber door is properly closed.
   (d) Turn the handle on the vacuum chamber such that the connection to the vacuum pump is open.
   (e) Rotate the black knob on the vacuum chamber such that the vacuum chamber is closed off from the outside air.
   (f) Turn on the vacuum pump (O/I switch)
   (g) Make sure the pressure sensors in the LabView program show that the pressure is decreasing.
2. Preheat thruster to desired temperature:
   (a) Wait for the vacuum chamber to have reached a pressure of 100 mbar or lower.
   (b) Turn on the heaters by setting the power level of the individual heaters to max 20 Watt and selecting Power Control by clicking the heating control selector button.
   (c) Continue heating until the thrust chamber temperature has reached a temperature of 10 °C below the desired temperature. Set the heating power to 0 Watt.
   (d) Set the input of the temperature controller to the desired temperature and click the heating control selector button to select Temperature Control. The temperature will now automatically rise to the desired temperature.
3. Repeat the following until the desired value of p_c is reached to within 50 mbar:
   (a) Open the thruster valve to check the resulting chamber pressure during thrust.
   (b) Close the thruster valve.
   (c) If the pressure was too low, open the pressure regulator slightly more (counterclockwise).
   (d) If the pressure was too high, close the pressure regulator slightly more (clockwise) and bleed off the excess gas.
4. Wait up to 5 minutes for the temperature oscillation to stabilise to an acceptable range (± 1 °C) and for the pressure inside the vacuum chamber to reach 5 mbar or lower.
5. Stop thrust_test_heated_N2.vi in LabView.
6. **Immediately** continue with calibration of the test bench:
   (a) Open 'Calibration for testing (attempt 1).vi' in LabVIEW
   (b) Specify a folder and test name and click run to start the LabView program.
   (c) Specify temperature setting
   (d) Note any offsets
7. Specify a folder and test name and click run to start thrust_test_heated_N2.vi in LabView.
8. Wait up to 5 minutes for the temperature oscillation to stabilise to an acceptable range (± 1 °C) and for the pressure inside the vacuum chamber to reach 5 mbar or lower.

Note: Do not stop the LabView program yet! Stopping the LabView program will stop the control of the chamber temperature. The time between stopping this test and starting the thrust measurements should not be much longer than 10 seconds to keep the chamber temperature stable.

Thrust testing at a set pressure

1. Restart thrust_test_heated_N2.vi in LabView.:
   a) Specify a folder and test name to save the upcoming thrust measurement.
   b) Click the STOP TEST button to stop the LabView program started for the environment setup.
   c) Click on the Abort Execution button to stop the LabView program.
   d) Click on Run to start the LabView program to start recording for the thrust measurement.

2. Perform the test

    a) Perform the actions from Table C.1 at the given time.
    b) During the experiment, make sure the variables shown in the LabView interface are within the expected values.
        a) If items are distinctly off, abort the test and assess the situation before continuing.

3. Stop the test

    a) At the end of the experiment, stop recording using the STOP TEST button.
    b) Press the Abort Execution button to stop the LabView program.
    c) In case more tests take place
        a) Specify a folder and test name and click run to start thrust_test_heated_N2.vi in LabView
        b) Return to item C.2 step 2

Time	Actions
0:00	Start recording
1:00	Open the propellant valve
6:00	Close the propellant valve
11:00	Open the propellant valve
16:00	Close the propellant valve
21:00	Open the propellant valve
26:00	Close the propellant valve
31:00	Open the propellant valve
36:00	Close the propellant valve
40:00	Stop recording

Table C.1: Actions to undertake during the nitrogen thrust measurement

Shutdown

1. Turning off equipment and allowing the thruster to cool:

    (a) Close the valve between the chamber and the pump (handle left of the door).
    (b) Turn off the vacuum pump.
    (c) Do not open the pressure equalization valve yet, to avoid oxidation.
    (d) Close the main valve on top of the N2 cylinder.
    (e) Close the high-pressure shut-off valve.
    (f) Turn the pressure regulator fully counterclockwise, so that it will start at zero outlet pressure for subsequent tests, and gas in the high-pressure line between the cylinder and the regulator is not wasted.
    (g) Bleed off excess gas in the low-pressure part of the feed system to ambient.
    (h) Close the low-pressure shut-off and selection valves.
    (i) Turn off the SM-7020, SM-7020-D, ES-030-10, E-030-1 and D-030-1 power supplies.
    (j) Unplug the D-sub15 cable from the Brooks 5850S mass flow sensor.
    (k) Wait for the thruster to cool down to $\leq$ 100 °C to avoid oxidation. Depending on the temperature tested at, doing this overnight may be preferable as especially for lower temperatures this can be very slow. Monitor the initial temperature behavior from LabVIEW to estimate the time needed.
    (l) Close LabVIEW, copy the acquired data to a USB-drive and turn off the computer.

2. Thruster hardware removal, after the thruster has cooled down sufficiently for safe handling ($\leq$ 40 °C):

(a) Open the pressure-equalization port on the front of the chamber to allow air to enter.
(b) Wait for pressure inside chamber to return to ambient, then open the door.

3. Optional in case the vacuum oven has to be left empty and no subsequent tests are executed:

(a) Uncouple the propellant quick connect at the back inside the chamber.
(b) Unplug the distance sensor cable.
(c) Unplug the USB DAQs from the USB hub.
(d) Unplug the heater and actuator electrical power cables.
(e) Unplug the sensor and valve electrical cables.
(f) Remove the DAQs from the vacuum chamber.
(g) Remove the thrust bench from the vacuum chamber.
(h) Disconnect the thruster from the thrust bench.
(i) Uncouple the MINSTAC tubing from the valve (can be done by hand).
(j) Remove heat shield from the thruster.

D

Test Results

D.1. Analytical model

Hutten [11] made an analytical model and the code is available on the GitHub repository RickHutten/ResistojetPerformanceTool. Inputs were put in manually to replicate the tables on page 12 of his report, this was successful as can be seen in Table D.1.

Input					
Propellant		Nitrogen		Nitrogen	
T_c	[K]	305.5 $\pm$ 5.8		670.7 $\pm$ 5.8	
p_c	[Kpa]	135.6 $\pm$ 5.0		166 $\pm$ 10	
p_a	[Pa]	184 $\pm$ 29		209 $\pm$ 32	
A_t	[10^3 μm^2]	70.6 $\pm$ 4.8		70.6 $\pm$ 4.8	
A_e	[10^3 μm^2]	531.7 $\pm$ 5.1		531.7 $\pm$ 5.1	
H_t	[μm]	496 $\pm$ 4		496 $\pm$ 4	
θ	[°]	20 $\pm$ 0		20 $\pm$ 0	
Output		This Work	Hutten	This Work	Hutten
Ideal:					
F_t	[mN]	15.45 $\pm$ 1.16	15.45 $\pm$ 1.16	19.02 $\pm$ 1.69	19.02 $\pm$ 1.69
$\dot{m}$	[mg/s]	21.77 $\pm$ 1.7	21.78 $\pm$ 1.7	17.87 $\pm$ 1.62	17.87 $\pm$ 1.63
I_{sp}	[s]	72.34 $\pm$ 0.73	72.34 $\pm$ 0.73	108.58 $\pm$ 0.62	108.6 $\pm$ 0.62
Expected:					
C_d	[%]	95.25 $\pm$ 0.17	95.25 $\pm$ 0.17	93.34 $\pm$ 0.28	93.34 $\pm$ 0.28
$\xi_{I_{sp}}$	[%]	77.75 $\pm$ 0.70	77.74 $\pm$ 0.70	68.13 $\pm$ 1.22	68.13 $\pm$ 1.23
F_t	[mN]	11.44 $\pm$ 0.97	11.44 $\pm$ 0.97	12.10 $\pm$ 1.32	12.10 $\pm$ 1.32
$\dot{m}$	[mg/s]	20.74 $\pm$ 1.66	20.74 $\pm$ 1.66	16.68 $\pm$ 1.56	16.68 $\pm$ 1.57
I_{sp}	[s]	56.25 $\pm$ 0.51	56.25 $\pm$ 0.51	73.98 $\pm$ 1.22	73.97 $\pm$ 1.22
$R_{e,t}$	[-]	3641 $\pm$ 256	3641 $\pm$ 256	1677 $\pm$ 139	1677 $\pm$ 140

Table D.1: Comparison analytical model as created by Hutten and replicated by the author

D.2. Microscope measurements

The Keyence VK-X1000 Confocal laser microscope and accompanying software was used to measure the nozzle exit width and height. To establish the exit width a root mean square value was taken from the four measurements taken in Figure D.2. The nozzle exit height could not directly be determined from the measurements taken in Figure D.1, but they were used to confirm the results found after exit area surface was directly mapped out.

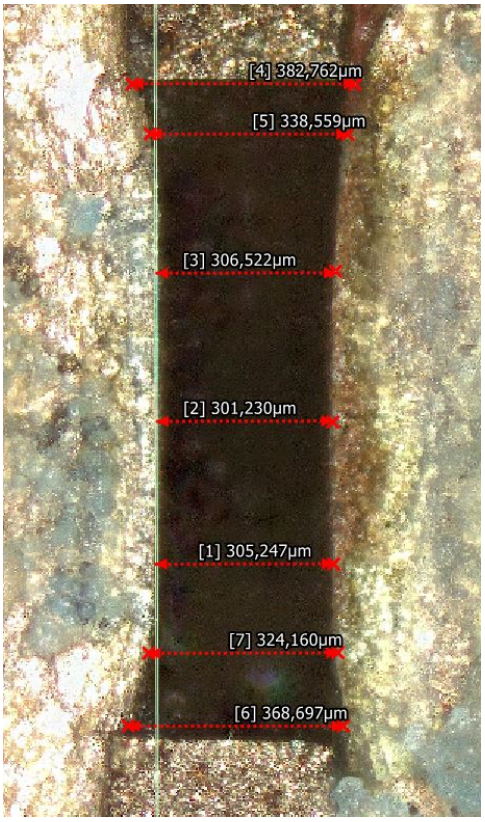

Figure D.1: Measurements performed with the microscope to get an indication of the nozzle exit height

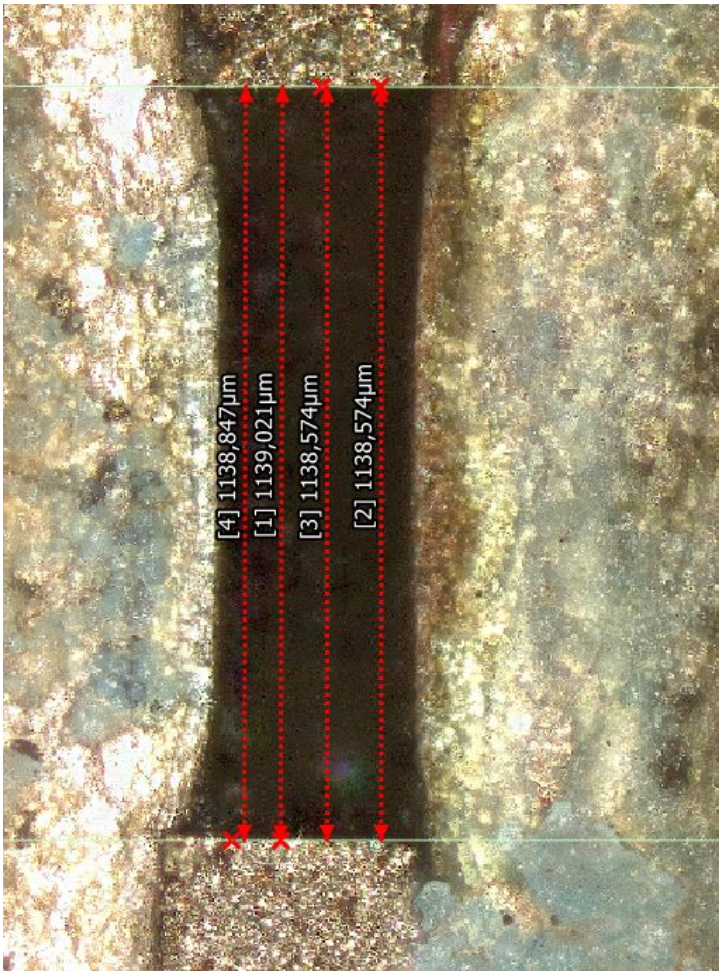

Figure D.2: Measurements performed with the microscope to get an indication of the nozzle exit width

D.3. Nitrogen testing

In this section, graphs and tables with results of each conducted nitrogen experiment are shown.

D.3.1. Test 20°C

Table D.2: Test at 20°C 1 bar

Name	Value	Uncertainty
Average thrust [mN]	5.86	0.20
Average massflow [mg/s]	16.50	0.13
Average pressure [mbar]	987.42	50.0
Average temperature of the thruster [°C]	21.15	6.01
Average specific impulse [s]	36.23	1.23

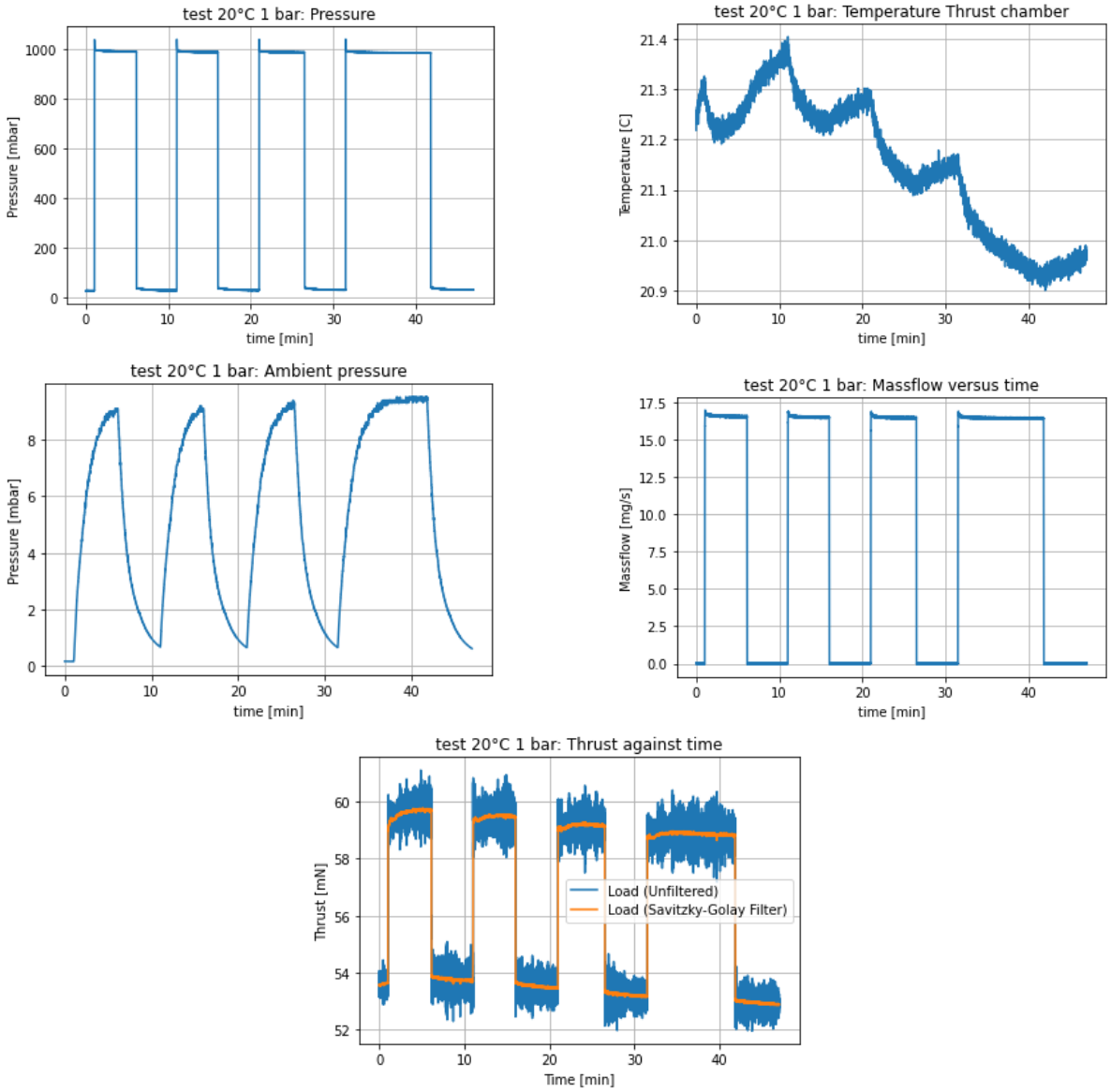

Figure D.3: Results of firing the thruster at 20°C

D.3.2. Test 200°C

At 200° experiments were conducted at both 1 bar and 1.5 bar chamber pressure.

Table D.3: Test at 200°C 1 bar

Name	Value	Uncertainty
Average thrust [mN]	5.36	0.17
Average massflow [mg/s]	13.02	0.09
Average pressure [mbar]	1000.26	50.0
Average temperature of the thruster [°C]	199.73	6.62
Average power [W]	9.09	0.21
Average specific impulse [s]	42.00	2.55

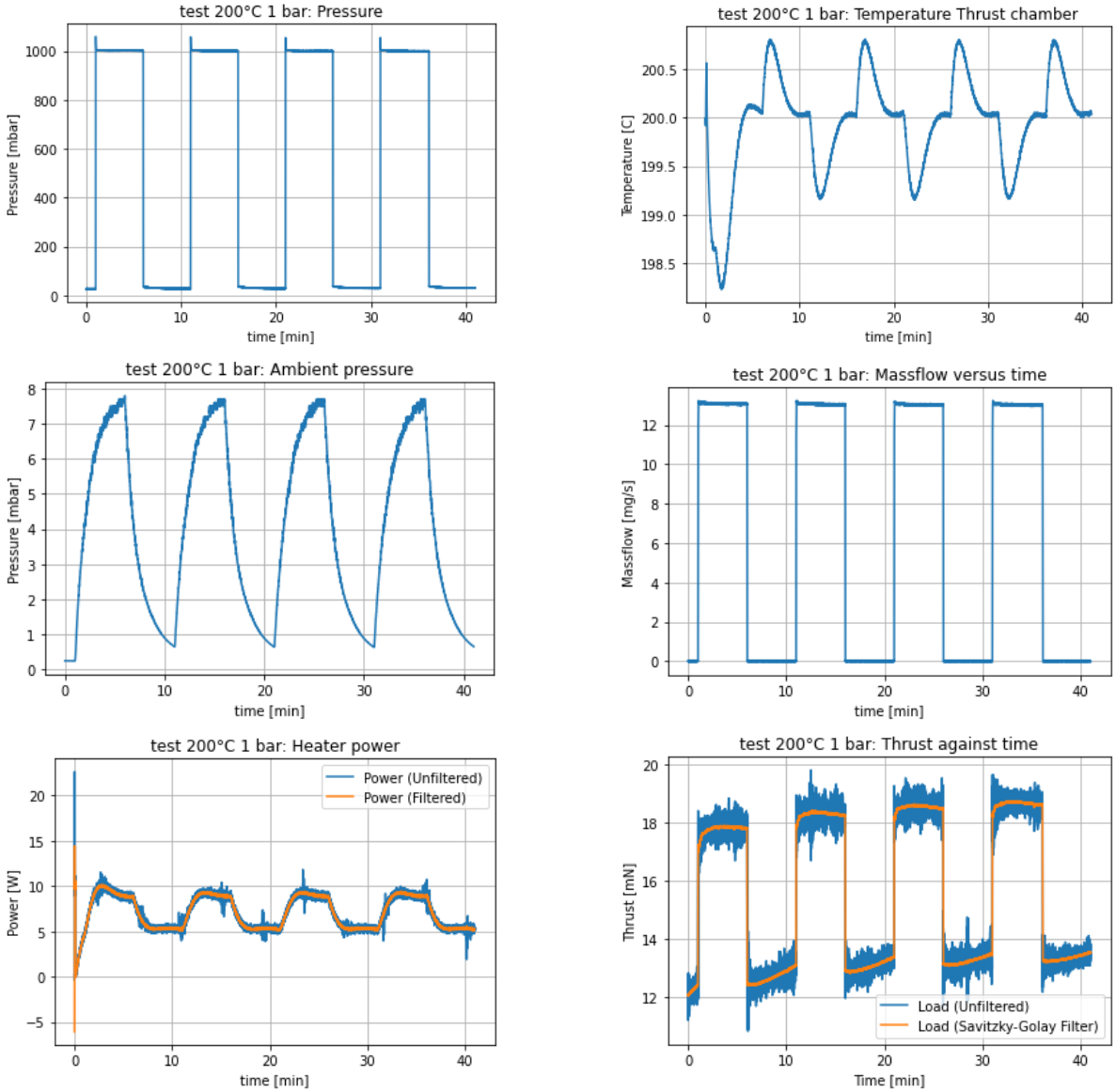

Figure D.4: Results of firing the thruster at 200°C

Table D.4: Test at 200°C 1.5 bar

Name	Value	Uncertainty
Average thrust [mN]	8.75	0.17
Average massflow [mg/s]	20.21	0.14
Average pressure [mbar]	1515.81	50.0
Average temperature of the thruster [°C]	199.62	6.62
Average power [W]	11.09	0.027
Average specific impulse [s]	44.14	0.91

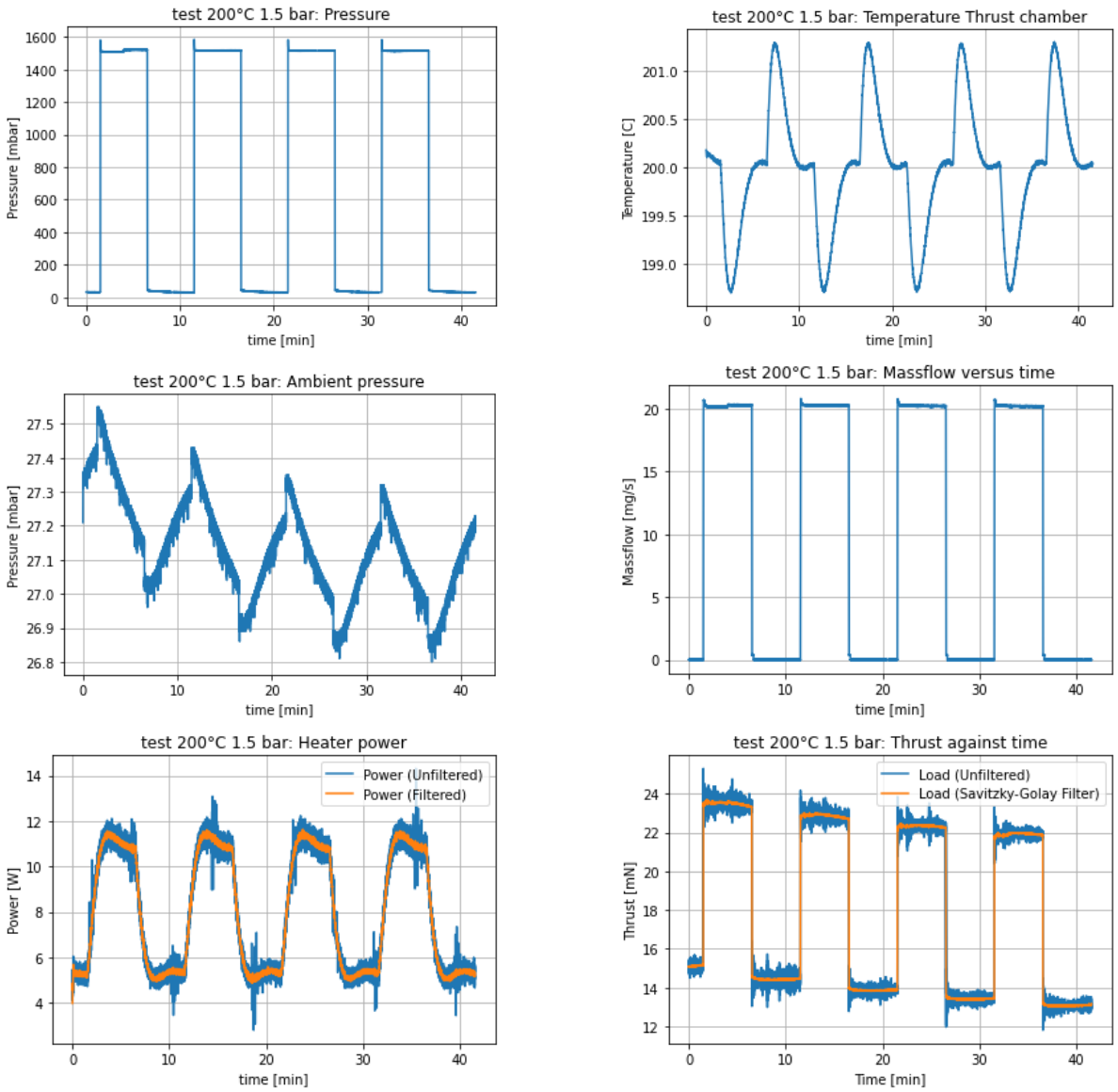

Figure D.5: Results of firing the thruster at 200°C at 1.5 bar

D.3.3. Test 300°C

Table D.5: Test at 300°C 1 bar

Name	Value	Uncertainty
Average thrust [mN]	5.11	0.32
Average massflow [mg/s]	11.93	0.08
Average pressure [mbar]	996.36	50.0
Average temperature of the thruster [°C]	299.64	7.05
Average power [W]	15.31	0.28
Average specific impulse [s]	43.69	1.49

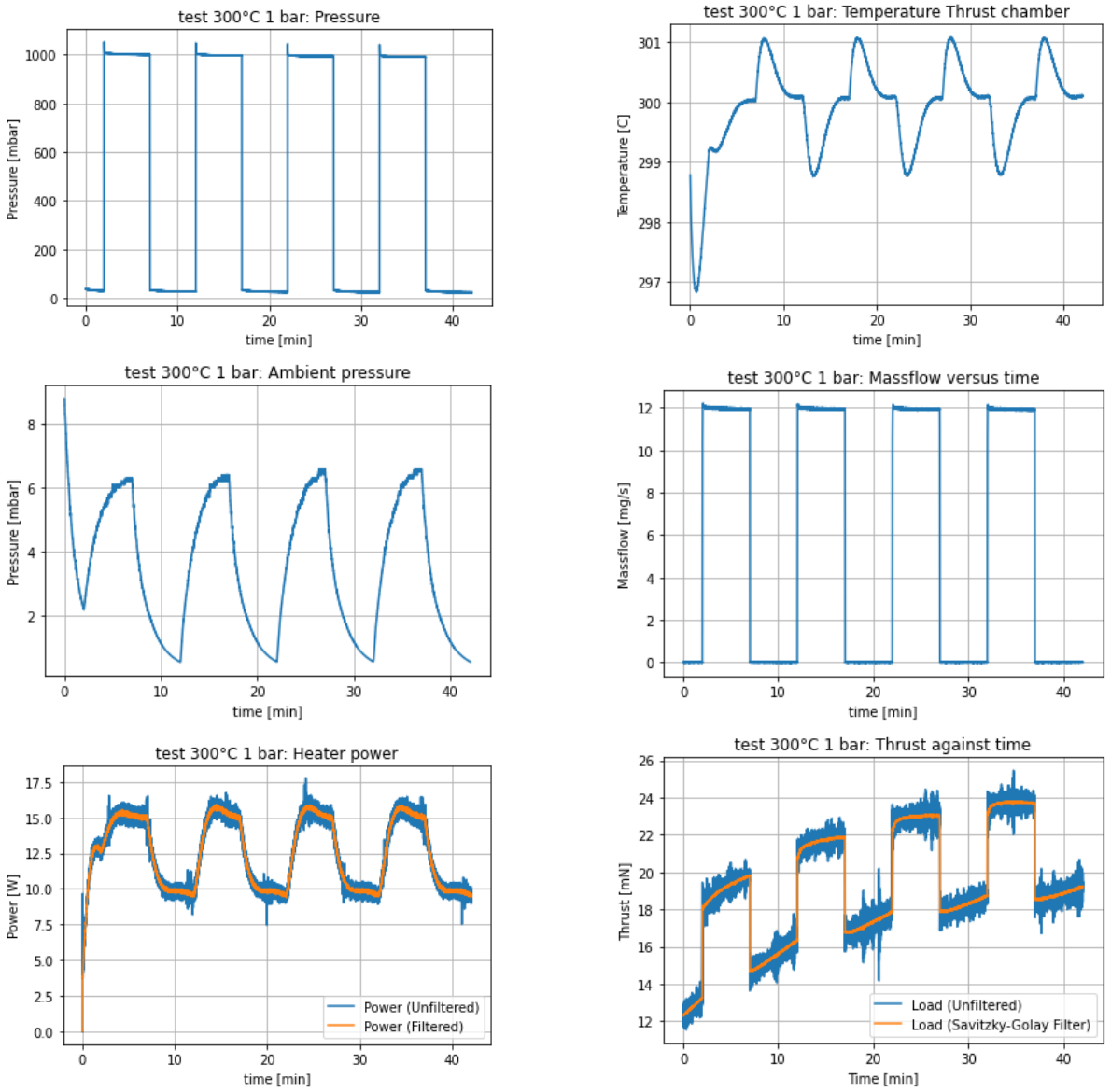

Figure D.6: Results of firing the thruster at 300°C

D.3.4. Test 400°C

Table D.6: Test at 400°C 1 bar

Name	Value	Uncertainty
Average thrust [mN]	5.07	0.17
Average massflow [mg/s]	11.53	0.08
Average pressure [mbar]	994.23	50.0
Average temperature of the thruster [°C]	399.44	7.53
Average power [W]	23.91	0.25
Average specific impulse [s]	44.88	1.53

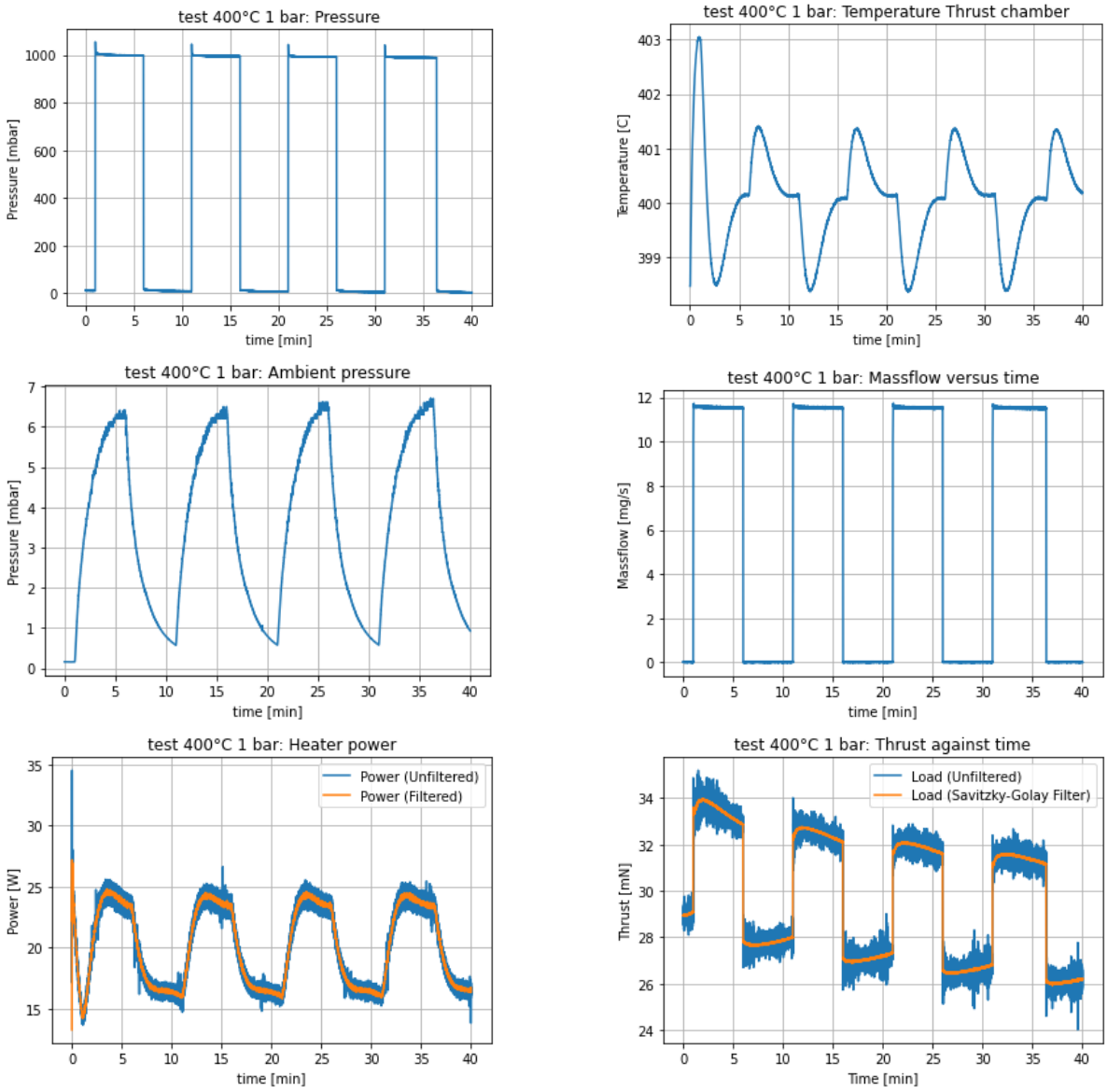

Figure D.7: Results of firing the thruster at 400°C

D.3.5. Tabulated data of each test

ID	T_c [°C]	P_c [mbar]	$\dot{m}$ [mg/s]	P_{heater} [W]	F_{thruster} [mN]	T_{ambient} [°C]	P_{ambient} [mbar]
NI-1.1	21.2 ± 0.1	990 ± 2.0	16.6 ± 0.07	-	5.94 ± 0.12	20.9 ± 0.2	8.4 ± 1.7
NI-1.2	21.3 ± 0.1	987 ± 1.2	16.5 ± 0.06	-	5.91 ± 0.07	20.9 ± 0.1	8.5 ± 1.7
NI-1.3	21.1 ± 0.1	987 ± 1.2	16.5 ± 0.06	-	5.81 ± 0.07	20.9 ± 0.1	8.6 ± 1.6
NI-1.4	21.0 ± 0.1	986 ± 1.7	16.5 ± 0.07	-	5.79 ± 0.11	20.9 ± 0.0	9.1 ± 1.6
NI-2.1	199.7 ± 1.6	1001.6 ± 1.0	13.05 ± 0.06	9.2 ± 1.3	5.38 ± 0.18	20.5 ± 0.4	7.2 ± 1.2
NI-2.2	199.7 ± 1.0	1000.2 ± 1.3	13.03 ± 0.06	9.1 ± 0.8	5.40 ± 0.20	20.4 ± 0.1	7.2 ± 1.3
NI-2.3	199.7 ± 1.0	999.7 ± 1.0	13.01 ± 0.06	9.0 ± 0.8	5.35 ± 0.17	20.5 ± 0.1	7.2 ± 1.3
NI-2.4	199.7 ± 0.9	999.6 ± 1.1	13.00 ± 0.06	9.0 ± 0.8	5.33 ± 0.13	20.7 ± 0.2	7.0 ± 1.4
NI-3.1	199.6 ± 1.4	1518.2 ± 14.7	20.24 ± 0.20	11.1 ± 1.0	8.74 ± 0.09	21.6 ± 0.2	27.2 ± 0.2
NI-3.2	199.6 ± 1.4	1516.9 ± 1.6	20.22 ± 0.07	11.1 ± 1.0	8.76 ± 0.07	21.7 ± 0.3	27.1 ± 0.2
NI-3.3	199.6 ± 1.4	1514.7 ± 1.4	20.19 ± 0.07	11.1 ± 1.0	8.76 ± 0.05	21.8 ± 0.2	27.1 ± 0.2
NI-3.4	199.6 ± 1.4	1513.5 ± 1.3	20.18 ± 0.07	11.1 ± 1.0	8.74 ± 0.04	22.0 ± 0.2	27.0 ± 0.2
NI-4.1	299.8 ± 0.8	1001.0 ± 2.0	11.95 ± 0.06	15.2 ± 1.0	5.19 ± 0.06	22.2 ± 0.1	6.0 ± 0.8
NI-4.2	299.6 ± 1.4	997.7 ± 1.4	11.94 ± 0.05	15.4 ± 1.2	5.25 ± 0.28	22.3 ± 0.2	6.0 ± 1.1
NI-4.3	299.6 ± 1.4	994.6 ± 1.2	11.93 ± 0.05	15.4 ± 1.2	5.00 ± 0.24	22.5 ± 0.2	6.0 ± 1.2
NI-4.4	299.6 ± 1.4	992.1 ± 1.2	11.92 ± 0.05	15.4 ± 1.2	5.02 ± 0.13	22.6 ± 0.2	6.1 ± 1.2
NI-5.1	399.4 ± 1.9	999.2 ± 1.4	11.54 ± 0.06	24.1 ± 1.8	5.05 ± 0.50	24.7 ± 0.5	5.9 ± 1.2
NI-5.2	399.4 ± 1.9	995.6 ± 1.3	11.53 ± 0.05	23.9 ± 1.6	5.02 ± 0.26	24.7 ± 0.3	5.9 ± 1.2
NI-5.3	399.4 ± 1.9	992.6 ± 1.2	11.53 ± 0.05	23.9 ± 1.6	5.12 ± 0.23	24.8 ± 0.3	6.0 ± 1.3
NI-5.4	399.5 ± 1.9	989.6 ± 1.4	11.52 ± 0.05	23.8 ± 1.7	5.11 ± 0.24	25.0 ± 0.3	6.1 ± 1.3

Table D.7: Experimental results, uncertainty is the 3σ of the measured values

D.4. Comparison of drift between experiments

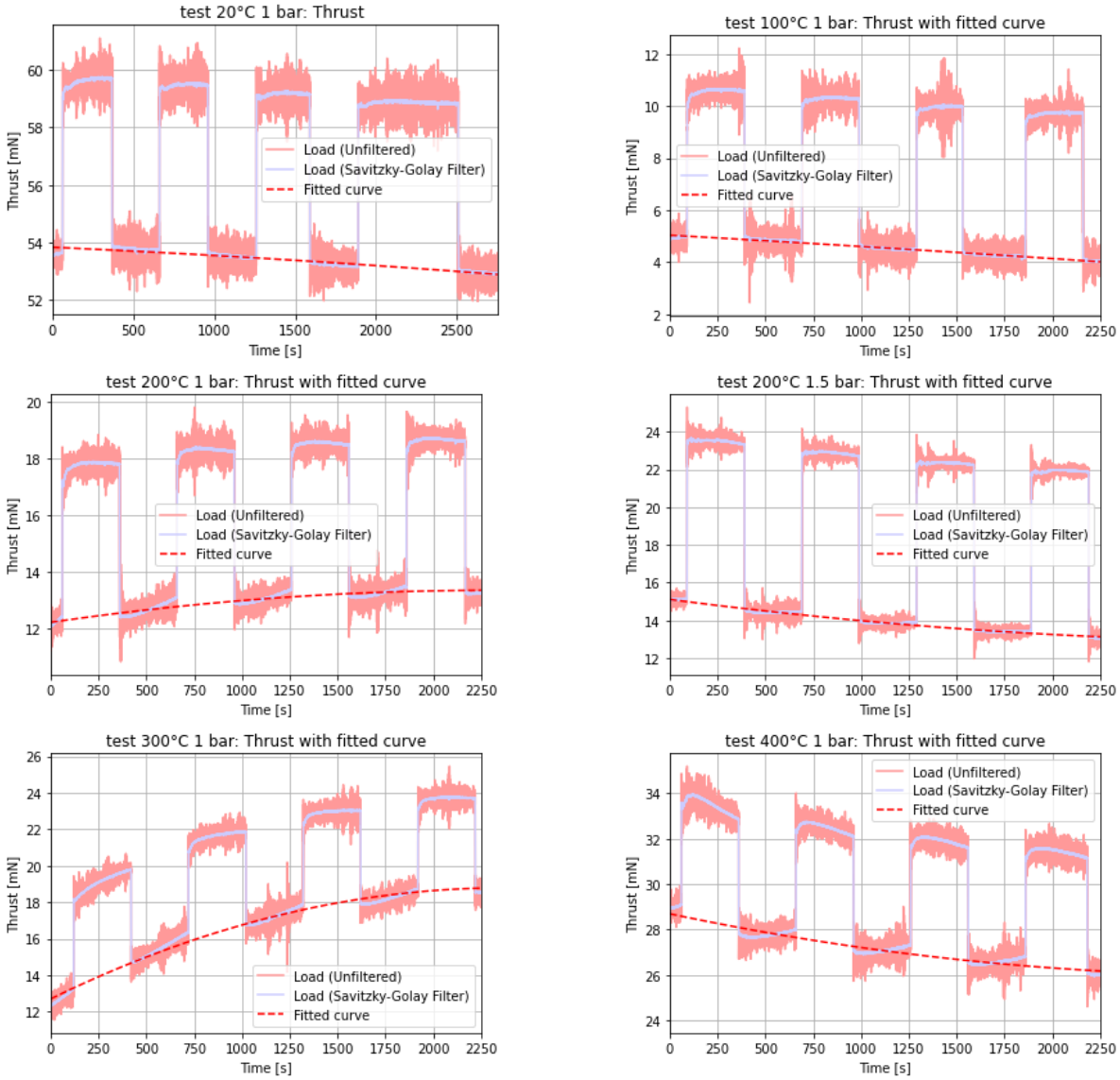

Figure D.8: Experimental thrust curves with fitted curve

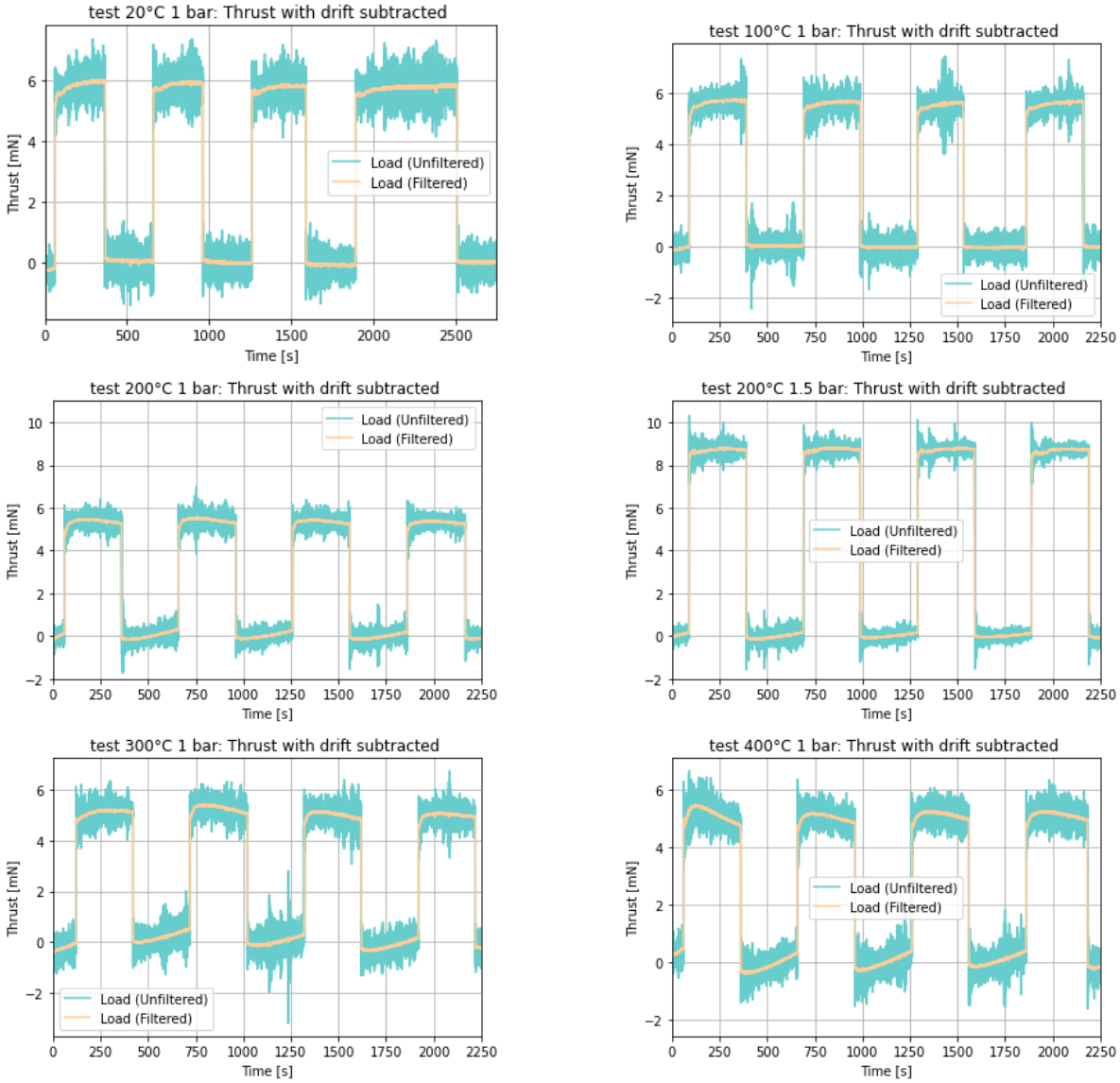

Figure D.9: Experimental thrust curves with the drift subtracted

D.5. Comparison of the analytical model to experimental data

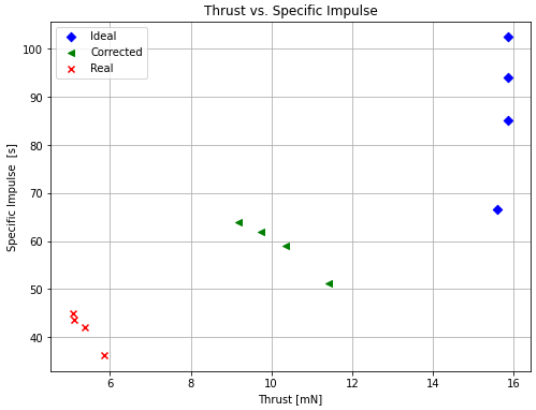

(a) Thrust versus Specific Impulse

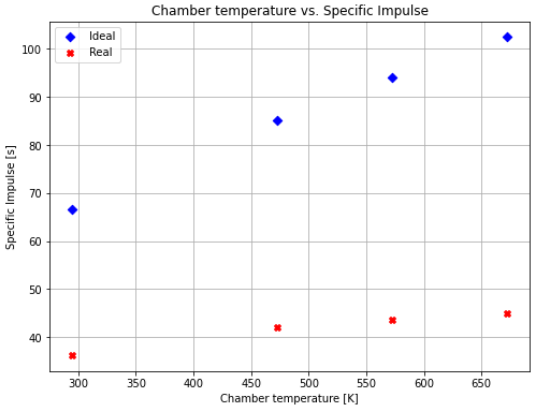

(b) Chamber temperature versus Specific Impulse

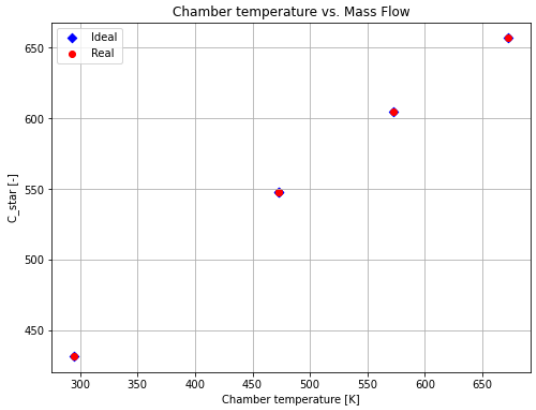

(c) Temperature versus characteristic velocity

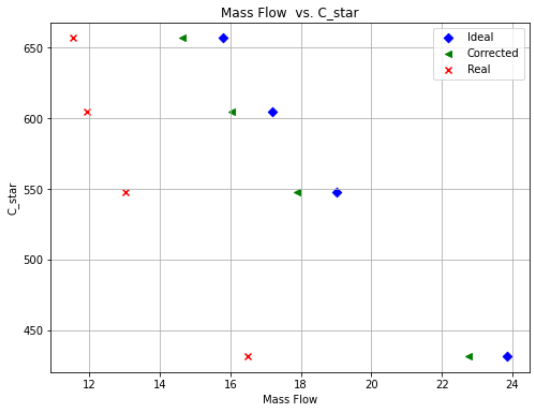

(d) Mass flow versus characteristic velocity

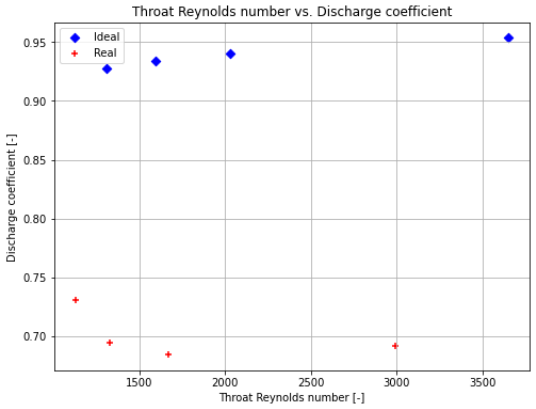

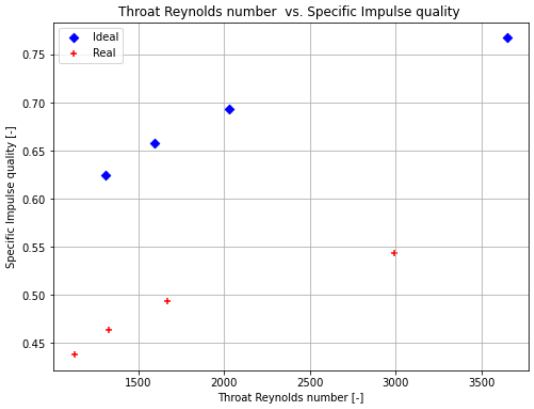

Figure D.10: Comparison of analytical and experimental results

E

Technical drawings

In this chapter the essential technical drawings made during this thesis are presented. Please disregard the scale as these images were adapted to fit into the appendix.

E.1. Copper Sealing Block

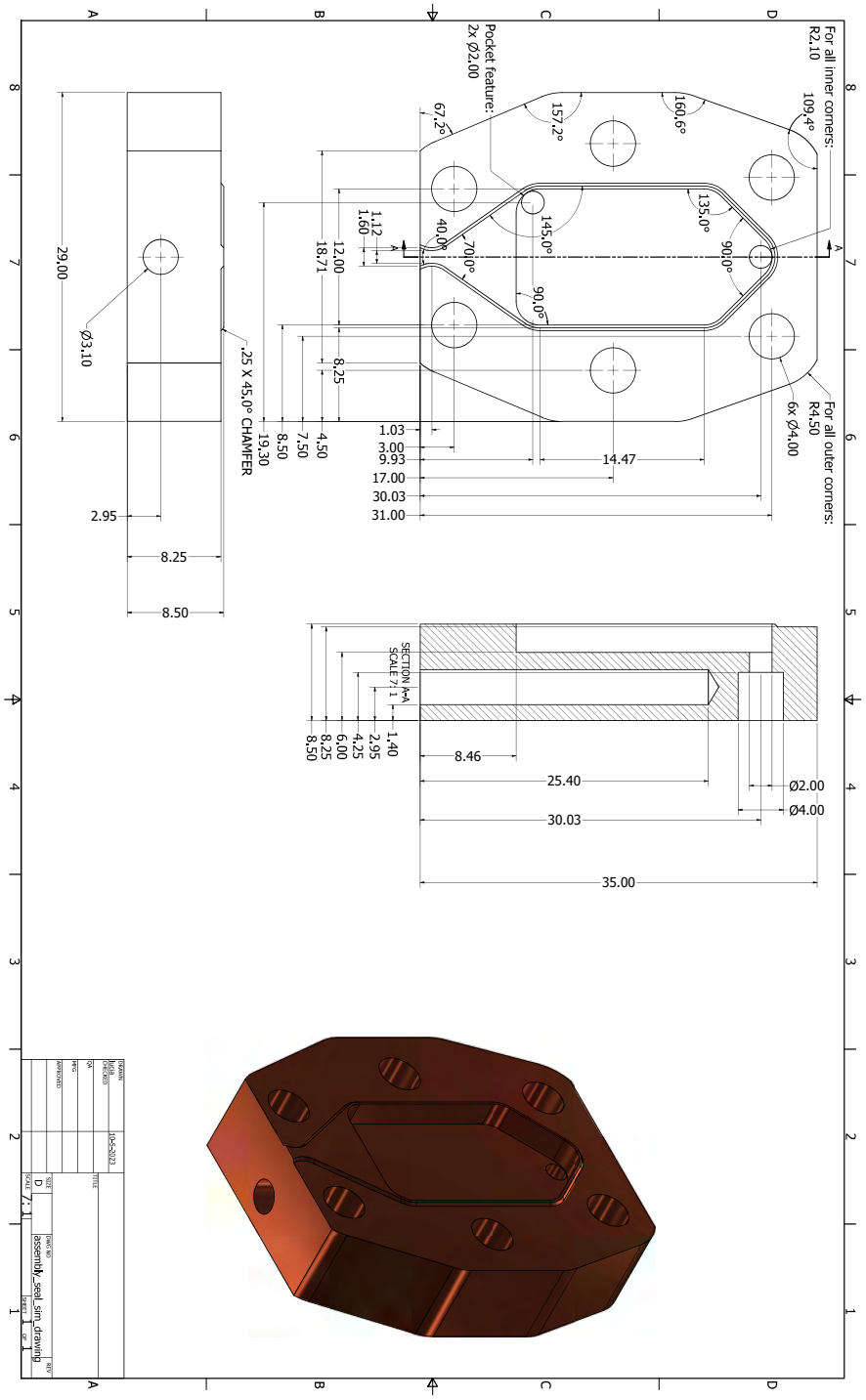

E.2. Test Bench Bracket